NTNU – Trondheim
Norwegian University of
Science and Technology

Tumor Dosimetry in a Phase I Study of Lu(177)-DOTA-HH1 (Betalutin)

How hard does the magic bullet strike?

Johan Blakkisrud

Master of Science in Physics and Mathematics
Submission date: June 2015
Supervisor: Pål Erik Goa, IFY
Co-supervisor: Caroline Stokke, OUS
Anne Catrine Martinsen, OUS

Norwegian University of Science and Technology
Department of Physics

Abstract

Introduction: Antibody-radionuclide-conjugate therapy using the monoclonal antibody agent ^{177}Lu-DOTA-HH1 (Betalutin^{TM}) developed by Nordic Nanovector, is a novel treatment of non-Hodgkin Lymphoma. A Phase I/II study is currently being conducted at Oslo University Hospital, the Lymrit-37-01-study. The main aim of this thesis was to develop and present a method to do dosimetric calculations on tumors in patients included in the study. Inhomogeneity of dose was investigated through dose rate maps and cumulative dose rate histograms.

Method: Using imaging data from two SPECT/CT-sessions 4 and 7 days post-injection, activity in lesions was quantified. Volumes of interest (VOIs) were drawn by a nuclear medicine specialist. VOIs were drawn with a margin around the imaged activity of the lesion, the novel $\text{VOI}_{\text{SPECT}}$-method. Cumulative activity was found through mono-exponential clearance of the activity. Patient specific masses from VOIs closely around the tumors were used. Absorbed dose was found by the proposed S-factor, $\bar{S}$, resulting in mean dose to the tumors. The activity quantification method was verified through phantom measurements with hot spheres in attenuating material. The energy absorption factor was found using the dose calculation computer program OLINDA. Dose rate maps were generated through the use of convolution of activity distribution and a voxel s-value kernel retrieved from a database.

Result: A total of 17 tumors in 6 patients grouped in three dose levels were ascribed a mean dose. Mean doses ranged from 86 to 794cGy. Inter- and intra-patient differences were observed. The phantom experiment showed good accuracy, with relative errors in the order of 5% compared to true activity. A constant factor $\bar{S}$ to calculate the absorbed energy was found sufficient as long as tumor volumes are in the range of 1mL to 300mL. 16 dose rate maps and cumulative dose rate volume histograms were made, and $\dot{D}$-values were found.

Conclusion: The method presented was found to be successful in the calculation of mean tumor dose. A method to generate dose rate maps and cumulative dose rate histograms has also been found and presented.

Sammendrag

Introduksjon: Antistoff-radionuklide-konjugatterapi ved bruk av stoffet ^{177}Lu-DOTA-HH1 (Betalutin^{TM}) utviklet av Nordic Nanovector er en ny og lovende behandlingsform mot non-Hodgkin lymfom. En fase I/II studie med Betalutin^{TM} pågår ved Oslo Universitetsykehus, Lymrit-37-01-studien. Målet med denne masteroppgaven var å utvikle og presentere en metode som gjør det mulig å beregne gjennomsnittlig absorbert dose til tumorer i pasienter som deltar i studien. Grad av inhomogenitet i tumorene ble undersøkt ved hjelp av doseratekart, og kumulative doseratevolumhistogrammer.

Metode: Aktivitet i lesjonene ble kvantitert gjennom bildedata fra to SPECT/CT-skan, gjort fire og syv dager etter injeksjon. Kumulativ aktivitet ble funnet ved monoeksponentiell modellert utvask av aktivitet. Tumormasser ble funnet fra inntegninger av tumorvolum på CT-data. Absorbert dose ble funnet ved å anta en konstant S-faktor, $\bar{S}$. Kvantitering ble verifisert mha. fantomopptak der sfæriske innsatser fylt med aktivitet og omgitt av attenuerende materiale simulerte lesjoner. Energiavsetningsfaktoren ble funnet gjennom doseberegningsprogrammet OLINDA, som nyttiggjør seg av en sfærisk tumormodell. Doseratekart ble generert mha. konvolusjon av aktivitetdistribusjon og voksel s-verdier i vev, med lik vokselstørrelse som SPECT-systemet.

Resultat: Gjennomsnittdose på organ-nivå i totalt 17 tumorer i 6 pasienter ble beregnet. Doser varierte fra 86 til 794 cGy. Forskjeller i dose både mellom ulike pasienter og innad i samme pasient ble observert. Utmerket kvantitering i fantomet ble funnet, feil omkring 5%. Bruk av en konstant $\bar{S}$ er tilstrekkelig så lenge tumorene ikke er større enn 300mL eller mindre enn 1mL 16 doseratekart og kumulative doseratevolumhistogrammer ble laget.

Konklusjon: En metode for å beregne gjennomsnittsdoser til tumorer har blitt utviklet, presentert og verifisert. En metode for å lage doseratekart har også blitt laget.

Acknowledgments

I have so many people to thank for making this thesis possible. First and foremost I would like to thank my outstanding supervisor, Unit Leader Nuclear Medicine Caroline Stokke at the Intervention Centre at Oslo University Hospital. I am deeply grateful to Caroline for the generous way she has shared with me, not only her specialist knowledge, but also scientific thinking in general. This has been very valuable to me, and is something I will take with me. Her guidance, knowledge and not least patience has helped me through this scientific adventure, thank you Caroline, you are the greatest! Gratitude also goes to Head of the Medical Physics department Anne Catrine Martinsen, my second supervisor, who has given constructive, and always valuable feedback with a keen eye for details, I am most grateful! In addition, I would like to thank my supervisor at NTNU, Associate Professor Pål Erik Goa, who helped out with the administrative part of the work.

I would also like to express my gratitude to physicists, medical doctors and other clinical personnel at the different departments and sections at Oslo University Hospital.

I would like to thank the Department of Radiology and Nuclear Medicine at Ullevål University Hospital for letting me use the SPECT/CT-scanner. Thank you Medical Physicist Jon Erik Holtedahl, who showed me how to use the scanner and helped with the phantom experiments. I want to thank the people at The Norwegian Radium hospital for lending me room and equipment; I want to thank Kari Bjering who lend me a key and let me return it under her office door many late evenings. In particular I would like to thank Nuclear Medicine Specialist Ayca Løndalen who delineated the tumors, thank you for showing patience and teaching an engineering student some rather detailed human anatomy.

At Rikshospitalet, I want to thank all the people at The Intervention Centre, for welcoming me into their community.

My gratitude also goes to High School teacher Siv Hennum Mohseni, for proofreading my questionable English.

I would also like to thank my family for showing me their support, and Mina Hennum Mohseni, for putting up with me all the nights I was working late.

Contents

Chapter 1

Introduction

Lymphoma is the tenth most prevalent cancer disease in the world. The systemic nature of the disease makes it difficult to treat with external radiation treatment. Moreover, the response to chemotherapy strongly varies from patient to patient. A new and rising treatment modality is proving ground in the clinic, antibody-radionuclide-conjugate therapy (also known as radioimmunotherapy). By attaching radioactive isotopes to biologically active molecules, the result is a «Magic bullet» that delivers the radiation directly to the cancerous site. New advances in chemistry and biological engineering make it possible to tailor medical remedies to specific diseases (Olafsen and Wu, 2010). Through the production of synthetic radioactive isotopes, these biological molecules can be linked to isotopes having the precisely wanted treatment effect.This makes for a treatment modality that can deliver a deadly amount of dose to cancerous cells, sparing normal tissue, resulting in more effective, systematic treatment with fewer negative side effects. New technology makes it possible to trace the radioactivity through the body, further tailoring the treatment to individual patients.

Radioactive elements have a long and intertwined history with the medical field. Irene Curie, the daughter of the famous Marie Curie and her husband Frederick Joliet were experimenting with polonium in 1936 and did a magnificent discovery: By irradiating a thin metal foil with a lump of Polonium, they were investigating how to form positron/electron pairs. When the metal foil kept radiating *after* the removal of the Polonium source, they realized they had discovered a new radioactive isotope. This discovery was published in an article in *Nature* (Joliot, 1934), and read by the Italian physicist Enrico Fermi. With a lump of radon sealed in beryllium and submerged in paraffin, he bombarded 60 pure elements with slow neutrons, and got 14 new «radioelements» back.

This he published in *Nature* later that year, in «Letters to the Editors» published in May, with a note on the 11th radioelement stating

> «Iodine - Intense Effect. Period about 30 Minutes.» (Fermi, 1934)

Radioactive iodine was picked up by the medical community, and used to treat thyroid diseases, and the field of nuclear medicine was born. Fermi's discovery led to a prosperous time in nuclear physics, where new radioactive isotopes were discovered at a rapid speed. Starting out with Fermi's 16 isotopes in 1934, to 141 by 1937, to over 3500 radioactive isotopes known today (NIDC).

Medical interest was sparked by the fact that radioactivity could be traced in the patient body. One of the first measuring devices, the Geiger-Muller tube, had been around since 1928. It was positioned over the organ of interest and used to quantify the flux of radiation (Jaszczak, 2006). A giant leap forward came in 1958 when Hal Anger made the Anger Camera, a scintillation crystal coupled to photomultiplier tubes, making two dimensional detection of radiation and «true imaging» possible. Using another kind of detector, two scientists, Kuhl and Edwards developed early in 1960 a technique to image the body with transaxial tomography. Tomography, from the Greek words τομος(tomos - slice) and γραπηό (grapho - to write) meaning literally to «write with slices» is an imaging technique where an image of the interior of an object is reconstructed through a series of projections. Their device had a detector doing both a translational and rotational motion, present in modern day scanners. Remarkably, Kuhl suggested to combine this emission tomography with transmission computed tomography, still an emerging technology, and described then the very first SPECT/CT-system.

Fast forward 40 years, computed emission tomography with single emission sources is a valuable tool for researchers and medical professionals. If we rearrange the words in the previous sentence we get SPECT (**S**ingle **P**hoton **E**mission **C**omputed **T**omography). Together with the plethora of available radioactive isotopes to image, they are fundamental parts of the vast field of Nuclear Medicine. An important and thriving therapeutic method is (targeted) nuclear therapy. The grand idea is to deliver a sufficient dose of radiation to the cancerous site, using biologic activity molecules linked to radioactive elements (Chatal and Hoefnagel, 1999). Especially useful are the nuclei that have both therapeutic and imaging qualities. These special radiopharmaceuticals (medical remedies with a radioactive agent) are called theranostic agents. The field of theranostics is quite young; in a special issue of *Seminars in Nuclear Medicine* dedicated to it, both the spelling theranostics and theranosis were used, to emphasise the novelty of the field (Freeman and Blaufox, 2012).

Dosimetry, the science of finding the absorbed energy in tissue, is used to establish radiotoxicity to normal organs, and amount of dose delivered to tumors. Dosimetry of tumors, though challenging, is of great interest, and is a field of ongoing research. Quantitative imaging have made it possible to investigate absorbed doses without putting further invasive strain on the patient (Flux et al., 2006). This is especially true when the therapeutic agent is possible to image directly, without the help of a tracer. Extensive research has been dedicated to tumor dosimetry, but alas, a plethora of methods exists and there is to some extent a lack of a general consensus (Baum, 2014). There are many potential reasons for this. First of all, antibody-nuclide-conjugate agents spans a large number of different radioactive isotopes used in an even wider range of radiopharmaceuticals. Further more, access to imaging equipment varies, both in research and clinical situations. Many of the elements of dosimetry are challenging, with scarce data points involved in measurements and highly varying systems in the form of patient and disease variability.

Betalutin^{TM}is a promising theranostic agent in the treatment of non-Hodgkin Lymphoma. It is produced by Nordic Nanovector, and is a radiopharmaceutical, a targeted nuclide therapy agent, specifically an antibody-radionuclide-conjugate therapy agent. Betalutin consists of a radioactive isotope of Lutetium (^{177}Lu) and the monoclonal antibody HH1. ^{177}Lu is a β-emitter which also emits γ-particles with energies that lie in a range suitable

for imaging.

An ongoing clinical phase I/II study of the treatment of non-Hodgkin Lymphoma using Betalutin^{TM}is currently conducted at Oslo University Hospital, the LYMRIT 37-01 study. The study provides imaging data that make it possible to investigate the amount of radiation energy delivered to the tumors. This is vital information to obtain better understanding of the delivery of the radiopharmaceutical to maximize treatment outcome.

The main goal of this thesis is to develop and present a method to do tumor dosimetry on the patients in the LYMRIT-37-01 study, undergoing treatment for non-Hodgkin Lymphoma with Betalutin ^{TM}based on quantitative imaging with a SPECT/CT-system. Primarily a method asserting the *mean* dose to the tumor is to be investigated. Elements in the method will be evaluated using both real patient and phantom data using hot spheres in attenuating material to simulate lesions. Further possibilities for voxelized dosimetry, where the inhomogeneous distribution of the absorbed dose is taken into account will also be discussed.

Chapter 2

Theory

2.0.1 Radioactivity

Radioactivity is the spontaneous process where the nucleus changes energy state and emits radiation particles. Three main categories of radiation particles exist, the heavy charged α-particle, light charged β^-/β^+-particles and the massless γ-photons. The particles have different characteristics, and have different interaction with matter. α and β-particles have short range, and give away their energy to the surroundings in dense energy tracks. Short range and high energy density make them good therapeutic agents, as they can locally deliver a sufficiently high amount of radiation energy to a target. Photons interact less, and can travel great distances before they interact. This makes photons valuable for diagnostic purposes, as they can escape the body without interacting.

Radioactive decay is statistical in nature, as they are governed by the laws of quantum physics. A useful parameter is the *rate* of disintegration, called activity. The rate of disintegration of N number of identical nuclei can be expressed by the differential equation

$$-\frac{\mathrm{d}N}{\mathrm{d}t} = \lambda N, \tag{2.1}$$

where λ is a suitable constant. This equation can be solved to

$$A(t) = A_0 e^{-\lambda t}, \tag{2.2}$$

where A_0 is the activity at $t = 0$.

The constant λ is called the decay constant, and can be used to express the nuclei half life

$$t_{1/2} = \frac{\ln(2)}{\lambda}. \tag{2.3}$$

This half life i.e. mean time until half of the nuclei have disintegrated, is an inherent characteristic of the nuclei.

In medical physics, the inherent half life (and corresponding decay rate constant) is often referred to as the physical half life (or physical decay rate). Another closely linked concept

is the biological half life, describing the uptake or clearance of the activity in parts of or in whole organisms. As secretion of substances from the body can often be modelled as exponential functions, the physical (λ_p) and biological (λ_b) constant can be combined to the effective λ_e,

$$\lambda_e = \lambda_p + \lambda_b$$

and effective half life can be stated as

$$t^e_{1/2} = \frac{t^p_{1/2} t^b_{1/2}}{t^p_{1/2} + t^b_{1/2}} \tag{2.4}$$

2.0.2 The nuclide - Lutetium

^{177}Lu, Lu(177) or $^{177}_{71}$Lu is a non-stable isotope of lutetium. Production of ^{177}Lu can be done in two different ways; either a direct route by irradiation of lutetium by neutrons or an indirect route of neutron irradiation of ytterbium, which causes a mix of different isotopes, and ^{177}Lu can be extracted radiochemically (Barchausen and Zhernosekov).

As it is a neutron-rich isotope, it will spontaneously undergo β-decay, turning a neutron into a proton and emitting an electron and a neutrino. The resulting energy is shared between the electron and neutrino, resulting in a continuous energy spectrum. The main decay-modes of lutetium are found in figure 2.1. Half life of ^{177}Lu is 6.7 days, short enough to assure energy deposition before being secreted, and long enough to ensure organ uptake. Mean energy of the emitted β-particles is 134.3keV (Kondex, 2003). Electrons interact in general both by energy exchanged in collisions, and radiation energy in the form of bremsstrahlung. The fraction of energy radiated compared to the total energy loss is dependent on the kinetic energy of the electrons. For electrons emitted from ^{177}Lu, the main loss is due to collisions.

The range of the β-particles emitted from ^{177}Lu is very short compared to other therapeutic nuclei. For example, the β-emitter ^{90}Y, an established nuclei in nuclide therapy , gives away 50% of its energy inside a sphere with a radius of 6.5mm, compared to a 0.6mm sphere for ^{177}Lu (de Jong et al., 2005). The maximum range of the electrons from ^{177}Lu is 2.2mm in water, compared to 12mm in ^{90}Y (Song et al., 2007). Mean ranges lie about 0.67mm for ^{177}Lu, making the deposition of energy from the β-particles local.

Main γ-energies are indicated by the thicker lines in the diagram in figure 2.1, having energies of 113 and 208keV with 6 and 11% abundance respectively. From an imaging perspective the abundance is low, but the photon energy lies well inside the realm of imaging. This makes it possible to image the distribution of ^{177}Lu in patients with commercially available SPECT/CT-scanner systems.

The dual nature of ^{177}Lu makes it an excellent theranostic agent, as it has both therapeutic and diagnostic qualities.

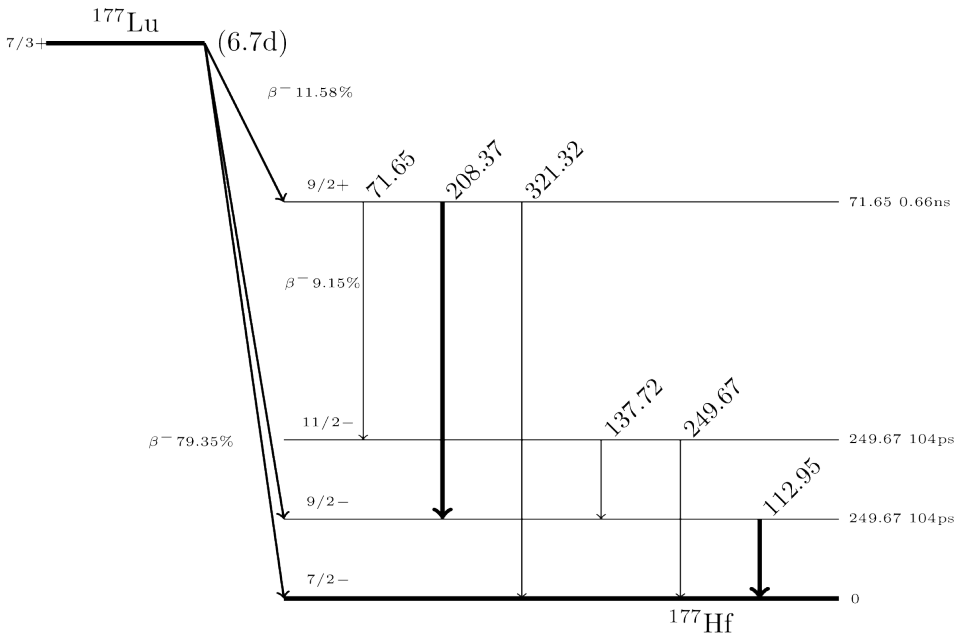

Figure 2.1: Decay scheme of ^{177}Lu, decay data from (Schötzig et al., 2001).

2.0.3 Betalutin^{TM} and non-Hodgkin-Lymphoma, Medical background

Betalutin^{TM} is a radiopharmaceutical developed by Nordic Nanovector to treat non-Hodgkin lymphoma. Lymphoma is cancer that develops in the lymph system, in B and T-cell leukocytes of the immune system. Non-Hodgkin lymphoma is a group of lymphomas, that itself is sub categorized into 25 subgroups (Holte and Fossa). Betalutin^{TM} is indented to treat relapsed Follicular Lymphoma and Diffuse Large B-cell lymphoma. Both are lymphomas where the disease stems from cancerous B-cells. B-cells express a large number of antigens, small peptides on the cell surface. As B-cells mature, properties of the cell membrane change with regards to antigen composition. One such antigen is CD37, a transmembrane molecule expressed on B-cells in the stage pre-B-cell to peripheral mature B-cell, though absent on both stem cells and plasma cells. In short, the antigen is expressed on malignant B-cells, and to a lesser extent on healthy cells, making it a good target for antibody-radionuclide.conjugate (Repetto-Llamazares et al., 2014b).

Betalutin^{TM} consists of a radioactive isotope of Lutetium (^{177}Lu) and a monoclonal antibody, HH1, linked with the chelator p-SCN-Bn-DOTA (DOTA). HH1 was originally developed at the Norwegian Radium Hospital (Smeland et al., 1985). The antibody HH1 has a high affinity for the antigen CD37. The drug is delivered through injection to the bloodstream.

Treatment with CD37 is a novel treatment. The closest therapies to compare it with are the two FDA-approved drugs Zevalin^{TM} and Bexxar^{TM}. Zevalin ^{TM}uses ^{90}Y as the radioactive component, Bexxar ^{TM}uses ^{131}I (Wiseman et al., 1999), (Horning et al., 2005). Both drugs use targeting molecules aiming to the antigen CD20. Comparing CD20 versus CD37 has been done as early as 1989 (Press et al., 1989) where both showed therapeutic applications, but CD20 was first utilized as a target in commercial drugs. Newer research

has led to renewed interest in CD37 as target, and ^{177}Lu as the radioactive agent (Repetto-Llamazares et al., 2014a).

2.1 SPECT/CT

2.1.1 Detector

The main purpose of the gamma-camera (i.e. SPECT-detector) is to detect incoming photons, and make a two dimensional representation of the activity directly facing the detector. The path to registration of an incoming photon consists of a sequence of events: A mean to exclude photons with an undesired incoming angle, a mean to convert photons to visible light and ultimately convert this visible light into an electronic signal. The first task is done by a collimator;often made of lead or another heavy, non-penetrable element and in a geometry that only permits transmission of photons having a specific angle. In modern scanners, a parallel hole geometry is often used. It is important that the collimator is tailored to the photon energies that are being detected. Photons having a greater angle than the acceptance angle are absorbed in the walls of the collimator.

Conversion of an incoming photon into an electrical signal is often done with an inorganic crystal. The inorganic crystal must be made in such a way that it has a large probability to interact with a photon. In most commercially available SPECT-systems this task is done by a sodium iodide(NaI)crystal. The incoming photon interacts with the crystal with a scintillation (flash or burst) and the result is a secondary photon in the visible spectrum. This secondary photon is then enhanced by a photomultiplier tube, that in turn will induce an electrical output. As a large crystal is desirable, multiple photomultipliers are placed on each crystal, and a centroid from multiple signals are made to deduce the spatial position of the event. This scheme of electronics is called «Anger logic», and often the full detector is referred to as an «Anger Camera». A schematic image of an Anger-Camera is found in figure 2.2. A further rejection of photons based on energy is done at this stage;photons outside an acceptance window of photon energies are rejected. The spectrum of accepted energies is called an energy window. An alternative to the scintillation crystal and the photomultiplier is a detector based on semiconductors. Such a detector is utilized to convert the photons to an electrical signal directly (Garcia et al., 2011).

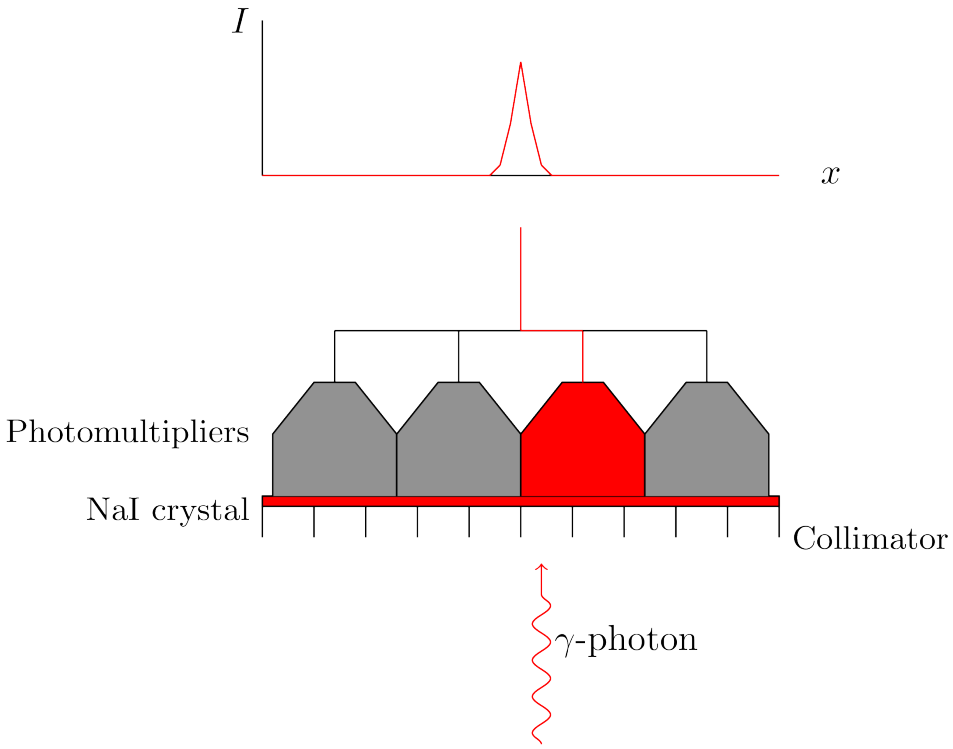

Figure 2.2: A schematic of a gamma-camera detector showing an incoming photon with the correct incident angle being detected and given a spatial value. The figure shows the one dimensional case, in reality the line of detector elements is a grid.

The chain of events leading to the detection of a photon, all the way down to the disintegration itself, is governed by stochastic laws. A consequence of this is that two measurements of identical activity distributions will in general give two different results. This makes the measurements, and in consequence the images, inherently noisy. Image noise can be quantified by the probability of measuring n counts and follows a Poisson distribution

$$p(z = k) = \frac{\lambda^n e^{-\lambda}}{n!}$$

with mean λ. As the number of counts detected increases, the mean of this distribution $\bar{k}$ will go to λ, and the standard deviation will be equal to $\sqrt{\lambda}$.

2.1.2 Image reconstruction

The principle in SPECT, as in all tomographic techniques, is to sample a number of projections around the desired object, and reconstruct a three dimensional image of the object.

The reconstruction of the tomographic image in modern equipment is done by an iterative reconstruction algorithm; where corrections for various image degradation factors are incorporated. Two main contributors to errors and degradation of quantitative SPECT-images are scatter and attenuation (Ritt et al., 2011). Both phenomena arise from photons interacting with matter before they hit the detector. Attenuation is loss of primary

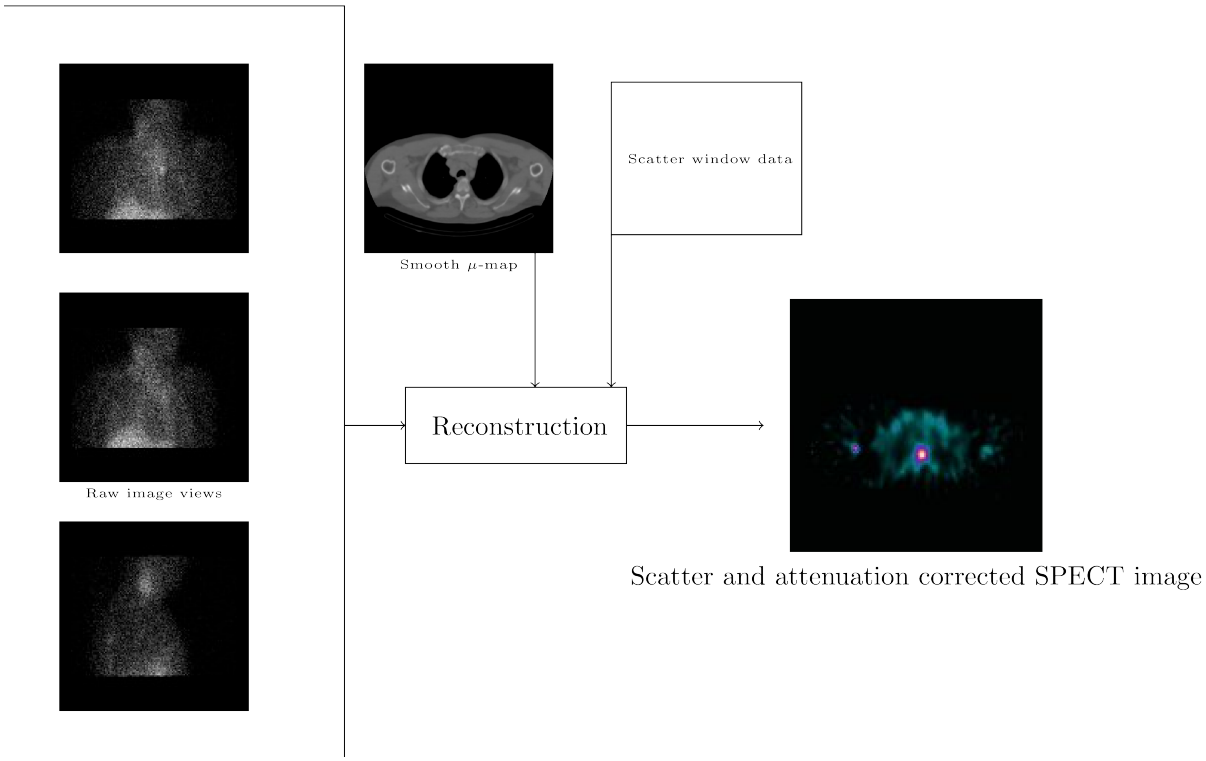

Figure 2.3: Overview of the data needed for a reconstructed SPECT-image. Raw data are illustrated with only three views, one axial slice illustrating the μ-map and a single slice representing the final SPECT-image. The scatter window data will look like the raw image view with reduced intensity. Images are from patient data in the Lymrit 37-01-study.

photons due to absorption in surrounding matter. Scattering arises when photons changes direction and momentum. In the range of energies for diagnostic photons mostly due to Compton-interaction with surrounding atoms. To account for attenuation, a map of the linear attenuation coefficients (μ) are made for the whole space imaged. This is in practice done by a CT-scan, resulting in a μ-map for the CT-photon energy. This map is then extrapolated for the relevant energies of the nuclei in question, and the map is directly used in the reconstruction. Scatter can be accounted for by choosing a «scatter window» where energies of the scattered photons are guessed a priori, and measured photon flux from this window is then used to reduce the contribution from scattered photons. An overview of the components in the reconstruction of an attenuation and scatter corrected SPECT/CT-image data set are shown in figure 2.3.

The reconstruction is often axial, meaning the primary reconstructed images are made of slices along the axial direction. The size of the axial image in number of pixels is called the matrix size. Matrix size together with the size of each pixel determines the field of view, as matrix size in each direction multiplied by pixel size. Typical matrix sizes in SPECT are 64 by 64 or 128 by 128, typical pixel size is 4-5mm. SPECT pixels are often isotropic, having equal size in all directions. Slices can be stacked on top of each other and give a three dimensional representation of the specimen. A pixel with a height, having a third dimension, is called a voxel.

2.1.3 Imaging resolution

The resolution of the imaging system is a crucial parameter, deciding how small structures that can be investigated with adequate precision. In a broad sense, the resolution is how small details that can be *resolved* (separated) in the image representation of the object. For a SPECT-system, the loss of resolution comes from a wide range of image degrading artefacts, some of which have already been outlined in previous chapters. The resolution can be quantified by the system PSF.

Mathematically formulated, imaging consists of forming an image, I of an object, P with some mathematical operator O,

$$P = O(P). \tag{2.5}$$

The operator O is generally not known, but a useful approximation often done is to model it as a spatial convolution between the object and the systems point spread function h

$$P = h \otimes I \tag{2.6}$$

h represents the image of a point, an object infinitely small and infinitely powerful.

SPECT systems are complicated, and results in complicated PSF-functions. However, The contributions can be separated into various parts, and assumptions that yield fruitful results can be made. An intrinsic aspect of the system is the geometrical limitations imposed by the collimator. This contribution can be modelled as a Gaussian function, and it can be shown that it is dependent on distance to the detector. Scattering inside the detector further degrades the resolution; this can also be modelled as a Gaussian (Rahmin and Zaidi, 2008). Collimator effects can be suppressed by moving the detector as close to the surface of the object as possible (Sohlberg et al., 2007). This is called contour imaging, and can be automated by a surface detection system on the scanner.

Further resolution loss can arise by septal penetration. As the name suggests, photons are penetrating the collimator septa, causing mis registration of photon events. Artefacts arising from these phenomena are complicated to correct for. As of now, Monte Carlo simulation techniques are required; this is ongoing research (A et al., 2002) (Du et al., 2002).

The intrinsic detector response and the collimator response can be separated into two Gaussian point spread functions, and a combined PSF can be found by convolving them. As the result of a convolution of two Gaussian functions is a Gaussian, the final PSF (not accounting for septal penetration and scatter) has a Gaussian form, in one dimension

$$f(x) = \frac{1}{\sigma\sqrt{2\pi}} e^{-\frac{x^2}{2\sigma^2}}. \tag{2.7}$$

As previously shown, this represents the image of a point in the SPECT system, and the full width at half maximum can be expressed by the parameter σ as

$$\text{FWHM} = 2\sqrt{2\ln 2}\sigma$$

It is worth mentioning that this is a very simplified representation. The surface-detector distance that the collimator response is dependent on, is neglected, and all of the imaging degrading factors have been summarized into a single Gaussian function. The PSF is also thought to be symmetrical in all spatial dimensions, which is also generally not the case. However, This have been shown to be a reasonable approximation in many settings.

The effective FWHM of the system can be found by measuring a point or line source. This must be done with the same scanner settings as the patient imaging.

The point spread function if known can be incorporated in the reconstruction, or be used on the resulting image to correct for degradation in the image data. When used post reconstruction, the goal is to invert equation (2.6), or even more general equation (2.5). This is not trivial; it can be shown through Fourier analysis that information is lost through the operator O, may be impossible to recover. This is stated without proof and it will be taken as granted (See for example (Flower, 2012) for a more rigorous treatment of the imaging problem.) A central element is noise; with stochastic noise it will become impossible to find *the* solution, but the goal then becomes to find the *best* solution.

Using the PSF-approximation described earlier, the solution to the problem becomes a deconvolution of the image, with the known PSF as kernel. Numerous algorithms for this have been developed and implemented in commercially available systems, popular algorithms in the nuclear imaging field are the Van-Cittert algorithm and Richardson-Lucy (Erlandson et al., 2012). The algorithms operate iteratively, and put constraints on the solution to suppress noise.

2.1.4 Partial volume effect

The partial volume effect (PVE) is a consequence of the limited resolution of the imaging system. The point spread function spans a limited *volume* in space, and puts a lower bond for the volume possible to quantify the activity within (Hoffmann et al., 1979). An important aspect of the PVE in quantitative imaging, is that objects with diameters smaller than 2-3 FWHM will appear to have a significantly lower activity concentration than they really have. The effect is dependent on object characteristics like size, shape and activity concentration within the object. Two common terms used to describe this artefact are «spill in» and «spill out», describing situations where activity concentration «leaks» into neighbouring regions.

Another consequence of the partial volume effect is a blurring of object rims. This manifests as a «penumbrae» around source objects. Difficulties in determining the borders around the object then arise. In addition to the finite resolution of the imaging system, the voxelation also imposes a limit on image resolution. This is because activity inside a voxel is represented as constant, but in reality can vary. This further contributes to the partial volume effect.

The effect can in emission tomography systems be viewed as a diffusion phenomenon (Skretting, 2009). Activity concentrated in small volume «diffuses» into nearby regions, similar to physical diffusion systems. This perspective makes concepts like spill inn and spill out more intuitive.

Partial volume effects can be corrected for, although the problem is far from trivial, as

mentioned earlier. An empirical, practical and frequently used approach is to image small spheres filled with activity. These spheres should be the size of, and have the same activity concentration as the structures that are to be quantified. The ratio between expected and measured activity is called a Recovery Coefficient (RC). RCs are calculated for relevant sphere sizes and activity concentration regimes, and multiplied with measured activity in the imaged structures to correct for loss of counts.

2.2 Dosimetry

2.2.1 General concepts

Dose, sometimes referred to in the literature as absorbed, dose is the energy absorbed per unit mass of material. It is often useful to define an average dose imparted in a medium, symbolically

$$D = \frac{\epsilon}{m} \tag{2.8}$$

where ϵ is the total energy, and m is the mass of medium.

The Medical Internal Radiation Dose Committee (MIRD) of the Society of Nuclear Medicine is an entity that since 1968 has tried to establish a common nomenclature in the process of asserting absorbed dose from internal emitters. Following the initial publication in 1968, several revisions have been done, an important part of which was the MIRD PRIMER, where the schema was published in a comprehensive and didactic form with numerous examples (Loevinger et al., 1988). The last revision, consisting of a nomenclature update of the schema was printed as a special contribution in *Journal of Nuclear Physics* in 2009 (Bolch et al., 2009). This chapter will outline the main points of the *MIRD schema*. The concepts will largely be based on the MIRD primer from 1988, with notes about discrepancy's from the 2009 article.

As the energy is carried by radiation particles, a natural starting point is the activity, A. Assume that some lump of matter, an organ or a collection of tissue, contains a certain amount of activity A_0 at time zero. The amount of activity will change with time, both because of the inherently physical decay of the radioactive nuclei, and as radioactive matter passes in and out of the mass boundaries. It is therefore best described as a function of time, called a *time activity function*

$$A = A(t). \tag{2.9}$$

This function is in general not known, and must be derived by measurements and assumptions about the flow of radioactive substance through the organ. The integral of this function will yield the total number of disintegrations having taken place inside the organ.

$$\tilde{A} = \int_0^t A(t)\mathrm{dt} \tag{2.10}$$

This important quantity is in the MIRD schema called the cumulative activity, often denoted by $\tilde{A}$. The time t in the integral is the time the radioactive material remains in the organ. A finite time is maintained by biological washout of the introduced substance, and eventually the ultimate transmutation by the physical decay. If this time is not reached during measurements, assumptions about the effective half life and further washout are made to assure an integrable function.

As the time activity function is not known, but the activity in every point in time must be known to gain the cumulative activity, it is very important to model the time activity function as accurately as possible. One way of constructing a time activity function is to fit measured data to an a-priori model. A series of measurements are made by various means of detectors, yielding time-activity points in time $\{a_i, t_i\}$. For many radiopharmaceuticals, a two phase model is assumed, one initial rapid, and a second, slower, washout phase. This can be mathematically modelled by a bi exponential function

$$A(t) = Ae^{\lambda_1 t} + Be^{\lambda_2 t}. \tag{2.11}$$

The initial phase can be neglected as it often has a small contribution compared to the second phase, and the time activity curve can be modelled as a single exponential.

$$A(t) = A_0 e^{\lambda_{\text{eff}} t} \tag{2.12}$$

Note the notation change from equation (2.11) to (2.12), A_0 being initial activity at time zero after introduction of radioactivity, and the effective half life λ_{eff}.

When the cumulative activity is found, the conversion to imparted energy is done by a suitable parameter S

$$\bar{D} = \tilde{A}S \tag{2.13}$$

The S-factor is another important part of the MIRD-scheme; it carries information about how the energy is transfered to the organ. S-factors will generally depend on a variety of parameters related to the nuclei and geometry of the system. If multiple sources of radiation are present, for example multiple organs containing ligands in the human body, it is convenient to group the organs into *source* and *target* organs. The use of the word organ is somewhat arbitrary, it could also mean different parts of the same organ.

Dose to a target organ r_t from a source r_s can be written as

$$\bar{D}(r_t \leftarrow r_s) = \tilde{A}S(r_t \leftarrow r_s) \tag{2.14}$$

and as multiple sources can contribute to dose in the same target, we write the dose as a sum over the source organs

$$\bar{D}(r_t) = \sum_s \tilde{A}_s S(r_t \leftarrow r_s) \tag{2.15}$$

over all sources.

The factor S in equation (2.15) generally consist of a sum of i particle types

$$S(r_t \leftarrow r_s) = \sum_i E_i Y_i \phi(r_t \leftarrow r_s, E_i) \tag{2.16}$$

where E_i is the mean energy of the particle, Y_i is the abundance of particle type i and ϕ is absorbed fraction of particle type i from source r_s to target r_t.

S-factors have been calculated for a variety of mathematical phantoms, simulating the human body. The calculations have been carried out by Monte Carlo simulations, where numerous medically relevant nuclei have been mapped. These pre.made calculations serve as effective lookup tables for calculations concerning the human geometry. This is an ongoing process, as new and more powerful computer power makes more and more realistic and detailed situations possible.

2.2.2 Tumor dosimetry

Quantitative imaging

Following the MIRD-schema, the first step on the path to do dosimetry in tumors is to find the cumulative activity. This is usually done by measuring the activity of the tumor in different points in time, and from these time points deduce a time activity curve. The way of measuring has followed the technological advances of medical imaging hardware and software. An early, and still extensively used technique, is to do a series of planar scintigraphies (Koral et al., 2000). By taking both anterior and posterior images, and combining them with a geometric mean, so-called conjugate view images can be formed, and errors related to attenuation can be reduced. From these scans tumors can be identified, and an image of a calibration source converts the detected image from counts to activity. Examples of time activity curves for non-Hodgkin-Lymphoma tumors in the pelvic, inguinal and abdominal area from a study by (Dewaraja et al., 2009) using a ^{131}I based antibody-radionuclide-conjugate therapy agent, are shown in figure 2.4

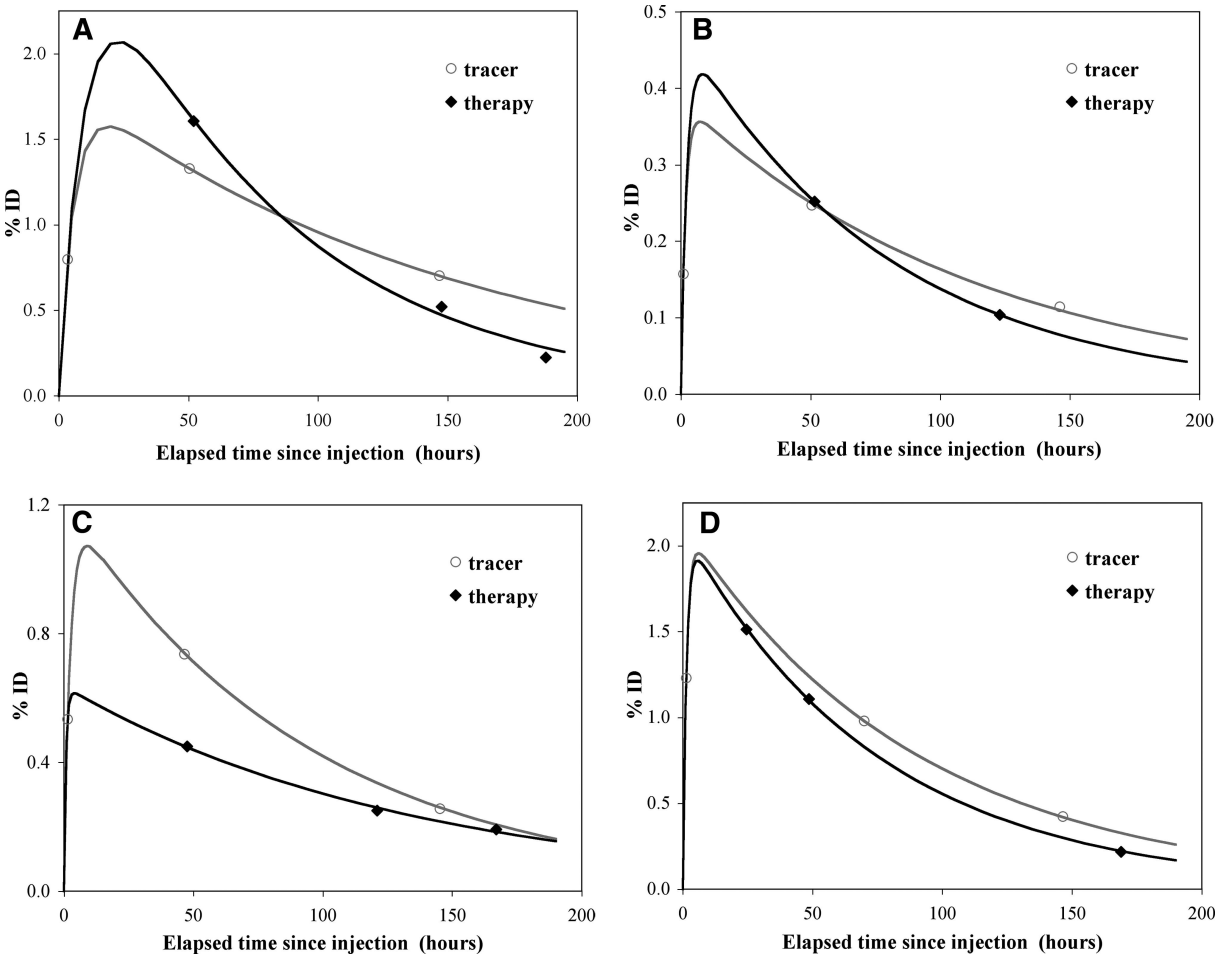

Figure 2.4: Examples of time activity curves from a study conducted on non-Hodgkin lymphoma patient undergoing treatment with a theranostic agent linked to ^{131}I. In the study, both a tracer and therapy imaging session have been conducted. The curve is a fit-curve based on a bi exponential fit model. The tumors are located in the pelvic (A and C), inguinal area (B) and abdomen (D). Figure is extracted from (Dewaraja et al., 2009)

As tomographic imaging equipment became more widespread and routinely used, three dimensional imaging of tumors has been more and more utilized. A great problem with planar images is sources that overlaps in the imaging plane, this problem is greatly reduced with tomographic imaging. Another clear benefit of a three-dimensional system is naturally that it is possible to find the distribution of the activity in all three dimensions. This is particularly interesting, as new research suggests that the dose distribution pattern, the inhomogeneity of dose in the tumor is relevant for the treatment outcome (Dewaraja et al., 2012) (Sgouros, 2005) (Dewaraja et al., 2014a), and has been investigated by the MIRD-committee.

Quantitative imaging has high demands for the SPECT-CT system. SPECT is historically considered as a qualitative imaging technique, unlike the «inherently quantitative PET» (Bailey and Willowson, 2013) This is inaccurate, as SPECT has shown great results in in vivo activity measurements. Using ^{99m}Tc, and appropriate scattering and attenuation correction techniques, errors in the order of 1.3% in ventricular fraction experiments have been found (Willowson et al., 2010). Quantitative imaging of small structures, like

tumors, have however proved to be difficult. The reasons are the coarse voxel size of the SPECT system, the broad FWHM length and the inherently noisy nature of SPECT. Extensive research has been done to assert the error in activity measurements, some of them presented in table 2.1.

Table 2.1: Phantom evaluations of radionuclides that are relevant for antibody-radionuclide-conjugate. ^{99m}Tc included. The table is partly collected from (Dewaraja et al., 2012)

Study	Radionuclide	Reconstruction/Corrections	Absolute quantification
(Zeintl et al., 2010)	^{99m}Tc	OS-EM, CDR, CT-AC, energy window based-SC, PVC	<5.8 % error in .5 to 16mL spheres
(Dewaraja et al., 2010a)	^{131}I	OS-EM, CDR, CT-AC, energy window based-SC	<17 % error in 8 to 95mL spheres
(Shcherbinin et al., 2008)	^{123}I ^{131}I ^{111}In	OS-EM, CDR, CT-AC, energy window based-SC PVC	3-5 % error in 32mL bottles
(Minarik et al., 2008)	^{90}Y	OS-EM, CDR, CT-AC,ESSE	<11 % error in 100mL spheres
He et al. (2005)	^{111}In	OS-EM, CDR, CT-AC,ESSE	<12 % error in 8-23mL spheres

Quantitative results from relevant geometries for ^{177}Lu are harder to come by, as the interest in its use is fairly new. (Beauregard et al., 2011) is often cited, finding errors in phantom measurements to be 5.6±1.9%. However, Measurements were done using a large cylindrical phantom with cylindrical inserts of 3cm diameter containing 175mL.

A good conversion from the cumulative activity to absorbed dose is not as straight-forward as for normal tissue organs. As tumors vary in shape, size and location inside the body, a good look up table for S-factors for tumors naturally does not exist. Finding good models that can be readily implemented in a clinical setting is still ongoing research. Five currently used methods are to be presented; a strictly local deposition model, the uniform sphere model, dose point kernels, voxel s-values and Monte Carlo simulations.

Local deposition and spherical model.

The first and simplest approximation is to assume local deposition of the energy emitted. This is a good approximation if the main energy contribution from the radiation is mediated through short range particles, such as electrons. Electrons have a more or less clearly defined range in tissue, and if this range is shorter than the voxel dimensions, local deposition can be assumed. A complication is the nature of the electron energies, as electrons are emitted in a continuous spectrum of energies. It is however possible to describe a mean energy of the electrons by a weighting of the spectrum. Contribution from photons is simply neglected.

When the tumor has a smaller size than the mean path of the electrons, or so large that the build up of photons becomes too dominating to neglect, the local deposition model becomes less valid. To account for these problems, the tumor can be modelled as a sphere

of uniform density, and analytical models incorporating the fraction of absorbed dose in different parts of the sphere can be made (Stabin and Konijnenberg, 2000). S-values for a wide range of medically relevant radio nuclei have been implemented into the FDA-approved dose calculating software OLINDA (Stabin et al., 2005). It is worth mentioning at this point that both the local deposition- and spherical model only takes into account dose from the radiation within the tumor, i.e. the self dose contribution.

Dose point kernel

A more refined way of calculating the absorbed energy, is through dose point kernels. A dose point kernel, used extensively in external beam radiation therapy to calculate doses, represents the energy deposition of a point source. Dose point kernels have been made for α, β and γ radiation. The electron radiation kernels were first made from analytical solutions of the electron transportation equation (Pretwich et al., 1989). At the very beginning, this was done for mono energetic electrons (Spencer, 1955). Later, as computers became more powerful, Monte Carlo methods were implemented and more refined kernels were calculated (Bolch et al., 1999). The dose point kernels are calculated as being in an infinite homogeneous medium, often water, which restricts the use of dose point kernels where the patient interior deviates from soft tissue (e.g. bones, lungs) and where boundaries between different tissue types are present.

Dose point kernels for photon radiation have also been made, resulting in extensive tables for different mediums and energy ranges. To implement dose point kernels, one is in need of an activity distribution in a matrix grid. The task of finding the energy absorption distribution then becomes to find the convolution of the activity distribution and the dose point kernel. Extra care must be taken when this problem is solved numerically; the partition and discretization of both the activity distribution and the kernel must be in correspondence (Bolch et al., 1999).

An example of a dose point kernel for photon radiation could be expressed mathematically as a radial function of a single radial spatial parameter x

$$\Phi(x) = \left[\frac{\mu_{\text{en}}}{\rho} \cdot \frac{1}{4\pi x^2} \cdot e^{-\mu x}\right] B_{\text{en}}(\mu x) \tag{2.17}$$

μ and μ_{en} are parameters related to attenuation and absorption, ρ density of the material and B is a build up factor linked to the number of scattered photons along the mean path length μx.

Voxel s-values.

A similar but different approach linked to the dose point kernel method is the voxel s-value formalism. As the dose point kernels, it is a description of an isotropic point source in a homogeneous medium, but calculated with a finite voxel size. This removes the need for the (historically) time consuming operation of convolution, and the resulting matrix can be thought of as a look up table for voxels. To illuminate the concept in two dimensions, consider a three by three matrix with voxel s-values

$$\mathbf{S} = \begin{pmatrix} 0.5 & 0.5 & 0.5 \\ 0.5 & 0.75 & 0.5 \\ 0.5 & 0.5 & 0.5 \end{pmatrix} \tag{2.18}$$

this matrix has units of mGy/MBqs.

The central value, 0.75, means a voxel has a self-irradiation of 0.75 mGy per MBqs. The voxel also contributes to a neighbouring voxel with reduced radiation energy, 0.5mGy/MBqs. This scheme can be extended far past the nearest neighbour, and in three dimensions. Through Monte Carlo simulations, such tables can be tailored to different media, nuclei and voxel sizes (Dewaraja et al., 2012).

A group of researchers in Italy have made a large database of voxel s-values for a large number of relevant nuclei and clinically interesting voxel sizes (Lanconnelli et al., 2012). This includes a total of seven different nuclei and 13 different voxel sizes, in both tissue and water. Following the MIRD-formula for s-values, the results of the Monte Carlo simulations are presented as a table ordered in a Cartesian grid with elements (0,0,0) up to (5,5,5) representing an octant in space. This octant can through symmetry be incorporated into a matrix as shown in equation (2.18). It is also possible from a set of s-values for an initial grid size to find values for a new cubical geometry through an extra- and interpolation scheme developed by (Fernández et al., 2013).

The dose calculation is carried out by inspecting each voxel in a voxelized cumulative activity distribution $\tilde{\mathbf{A}}$ by its surroundings, adding each contribution and putting the final sum in a map of absorbed dose, mathematically written

$$D\left(\text{voxel}_T\right) = \sum_{S=0}^{N-1} \tilde{A}\left(\text{voxel}_s\right) S\left(\text{voxel}_T \leftarrow \text{voxel}_s\right). \tag{2.19}$$

over every target and source voxels.

We recognize equation (2.19) as a voxelized edition of equation (2.15).

Monte Carlo

An alternative to all of the above-mentioned ways of converting cumulative activity to absorbed energy is directly through a Monte Carlo simulation. The method uses real or simulated patient geometries describing the boundaries, density and composition of the system. The activity is then distributed according to the SPECT-data, and a simulation of the energy absorption is done. This results in either dose rate maps (if activity distribution is used as input) or absorbed dose (if cumulative activity is used). The dose maps can be integrated to yield absorbed dose through a kinetic model of the activity uptake/secretion. A thorough description of the process is beyond the scope of this work, but for all intents and purposes it is considered the gold standard of which all methods are compared.

2.2.3 Cumulative dose rate histograms and dose rate maps

A spatial distribution of dose in a volume is called a dose map; if the distribution shows dose rate it is called a dose rate map. To represent a three dimensional volume in two dimensions, the volume is often visualized as a group of slices. If a spatial distribution of the dose or dose rate (dose per unit time) is available, a useful way of presenting it is through a cumulative dose(/dose rate) volume histogram. The method is well known from external beam radiation therapy, where such data are an integrated part of routine therapy (Lyman, 1985). The voxels inside a target region are collected, and sorted based on dose content. The fraction of the volume, i containing dose above a certain dose d is then calculated. A volume fractions i_n are then plotted against the doses, d_i as in figure 2.5(b) Volume is often shown as a fraction value of the whole target volume as ordinate, and dose in numerical value as abscissa. This give a useful two-dimensional representation of a three-dimensional volume.

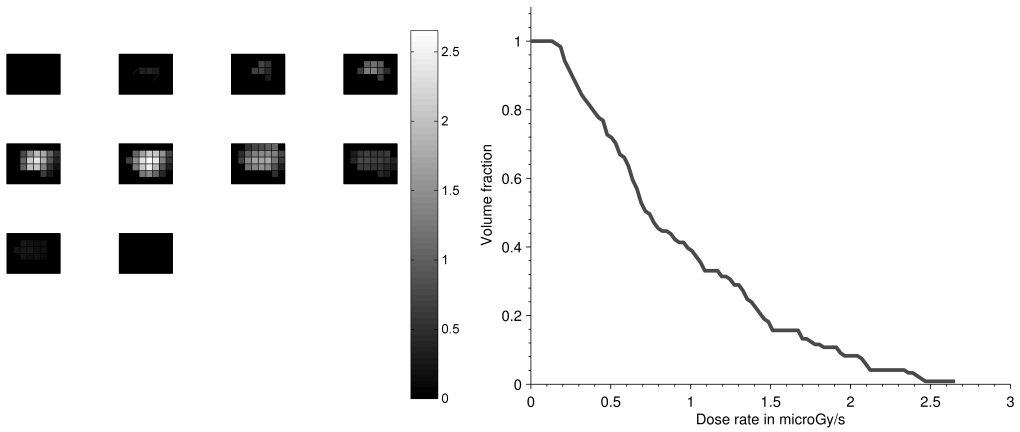

Figure 2.5: An example of a cumulative dose rate volume histogram (b) from a dose rate map (a). The map is segmented into slices, representing a three dimensional volume with two dimensional slices.

An often relevant concept in external beam radiation therapy, and also increasingly in molecular radiotherapy, is the minimum dose that covers a certain fraction of the volume. This dose is noted D_{90}, where the subscript indicates the volume fraction in percent; if the histogram shows dose rate, the parameter is given a dot, $\dot{D}$, to emphasize rate. For example, the $\dot{D}_{90}$ dose in figure 2.5 is around 0.3μGy per second, as this is the minimum dose rate in 90 % of the volume.

2.2.4 A note on voxel based dosimetry

Although not stated explicitly, the dose point kernel, voxel s-value and Monte Carlo methods deal with the distribution of absorbed dose in a structure (e.g. a tumor or an organ) on the voxel level. As imaging modalities have reached better and better resolution, quantification on the voxel level has become possible. The same concepts follows from previous chapters, initially activity is ascribed to each voxel in different points in time.

Some assumption of the kinetic nature of the activity is made, a mono-exponential, bi-exponential or other kinetic model, making a time activity curve of each voxel. These time activity curves are then integrated to form a three dimensional image of the cumulative activity in the volume investigated. Through this cumulative activity map, the energy absorbed is found through dose point kernels, voxel s-values or a Monte Carlo simulation. Another angle of approach is to find the dose rate in each voxel, assume a model of the dose rate based on the overall kinetics, and integrate this expression to yield a dose distribution (Dewaraja et al., 2012).

To trace parts of a tumor or organ across time, multiple images of the tumor have to be registered to each other. The image registration process is often done by setting one image as the «fixed» image, and subsequent images as «moving». A series of transformations are then applied to the moving image to register it to the fixed image. The last transformed moving image serve as the fixed image to the next image in a full time sequence.

Voxel based dosimetry can yield new insight into the dose response of tumors, by investigating and quantifying the dose inhomogeneity of tumors.

Chapter 3

Method

The imaging data consist of two parts. The first part is a phantom data-set, obtained by phantom SPECT/CT scans conducted over the course of this work. The second part is a set of SPECT/CT patient data, retrieved from the patients undergoing Betalutin^{TM} treatment.

3.1 Scan parameters

Both the phantom study and the patient study had the same imaging and reconstruction settings. The SPECT-component had a dual-headed detector system, using NaI-crystals with a crystal thickness of 3/8 inches. A medium energy collimator was used. Acquisition was done by 2 times 32 projections with 45 seconds rest time using a non-orbital 180 degrees orbit in step-and-shoot mode. Reconstruction was done by an iterative method, 4 iterations with 16 subsets. The size of the matrix was 128^2 with isotropic voxels, 4.79mm sized, this yields a field of view of 61.3 cm. Two energy windows are detected, centered on the main gammas of ^{177}Lu, 113 and 208keV with a 20% window width. Scatter windows are used for scatter correction, and the attenuation correction is done by the CT.

The CT system was a 16 slice CT. Voxel size 0.98 by 0.98 by 3mm and reconstruction increment resulting in 0.98 by 0.98 by 1.5mm voxel size. Two CT-reconstructions were done from the CT raw data; the difference was the kernel made by the manufacturer, resulting in a reconstruction used in attenuation correction (using the B08s-kernel) and a sharper image reconstruction used to define anatomical features (B30s-kernel).

3.2 Phantom imaging data

A mixing volume of 1.5 litre was injected with 1.042GBq of lutetium, yielding 0.693MBq/mL. Injected activity was measured with a dose calibrator. A cylindrical water filled NEMA-phantom with five micro-spheres and one spherical shell was used. The insertions were filled with the ^{177}Lu-solution, yielding the same activity concentration in all insertions.

Measurements were done with the Siemens Symbia-T16 SPECT/CT-scanner. Scan parameters were kept identical as for the patient imaging protocol in the Lymrit-37-01 study.

Reconstructions were also done using the Lymrit-37-01 reconstruction protocol. A total of four phantom measurements were performed, called week0 to week3, spanning roughly a month.

Volumes of interests (VOIs) were drawn around each individual sphere. A «physical VOI», VOI_{CT} was drawn closely around the physical extent of the sphere. A second, larger VOI, $\text{VOI}_{\text{SPECT}}$ was drawn around the imaged activity with a manually defined margin. High activity concentration on the first scan session made it difficult to resolve the «activity clouds» on the images; this is illustrated in fig 3.1a. VOIs from Week1 are shown in figure 3.1b, and a CT-image in 3.2. Enumeration of the VOIs are found in the next section. Activity was estimated using a previous acquired count-activity conversion factor.

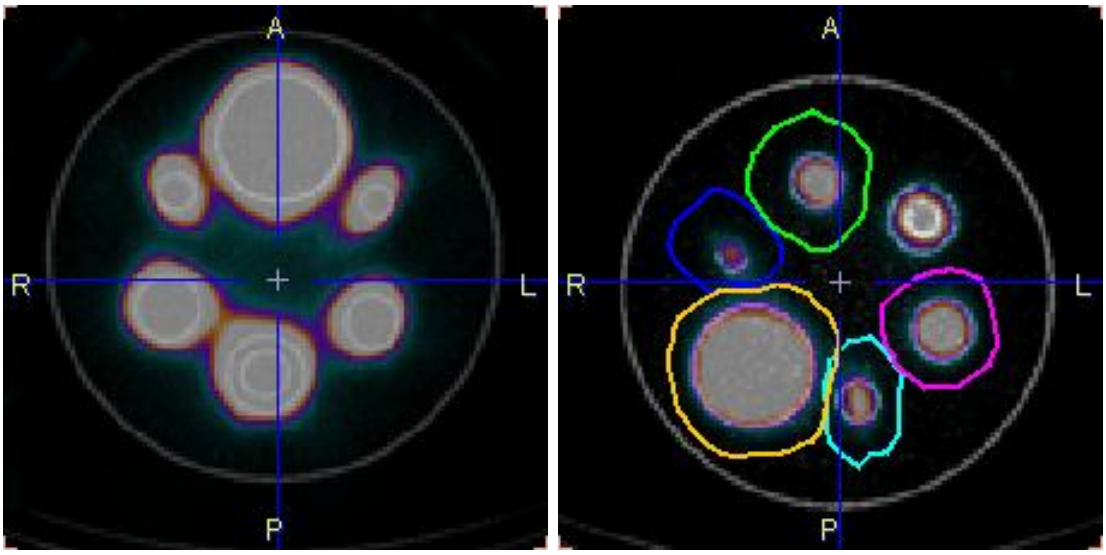

(a) **(b)**

Figure 3.1: SPECT/CT-images from Week0 (a) and Week1 b(b). Colored bands in (b) are curves in $\text{VOI}_{\text{SPECT}}$.

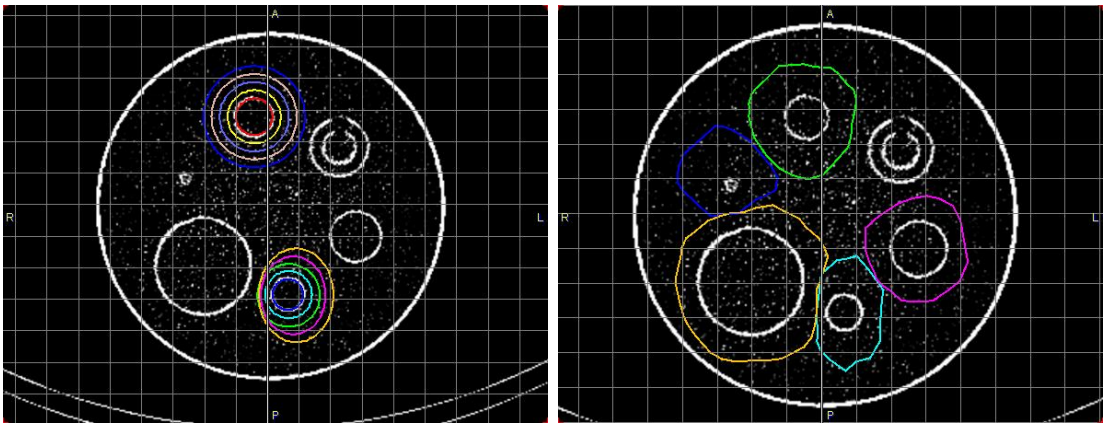

(a) **(b)**

Figure 3.2: CT-data. Grid size 20mm. (a) show different margins, (b) $\text{VOI}_{\text{SPECT}}$

3.2.1 Phantom validation

The data collected from the series of phantom measurements served three purposes

i) Validation of the novel activity VOI $\text{VOI}_{\text{SPECT}}$.

ii) Finding Recovery Coefficients by defining a CT-guided VOI around the spheres.

iii) Investigation of different margins around the spheres.

i) Validation

Using a margin around the physical object, $\text{VOI}_{\text{SPECT}}$ instead of a physical VOI VOI_{CT} is a novel approach. Therefore, measurements were validated by comparing the measured activity with the expected activity. Expected activity was found by decay-correcting the initial activity concentration found by the dose calibrator. Relative errors between measured and expected activity were found.

Relative errors between measured and expected activity are found in table 4.2. The relative error was defined by the following equation:

$$\Delta A = \frac{A - A_{\text{ref}}}{A_{\text{ref}}} \cdot 100.$$

This definition is used throughout the result chapter unless stated otherwise.

ii) Recovery Coefficients

Recovery Coefficients were found by delineating a CT-guided VOI around the physical image of the spheres, acquired by the CT. This activity was then divided by the known activity, resulting in a Recovery Coefficient, an extensively used approach in the literature. Coefficients were used to assert the loss of counts due to partial volume effects, and to compare with similar studies. By doing this over a range of different activity concentrations (as ^{177}Lu disintegrate yielding progressively less and less activity as time passes), it was possible to follow the RCs development through activity concentration regimes.

iii) Margin investigation

The two VOIs $\text{VOI}_{\text{SPECT}}$ and VOI_{CT} represent two extremities of VOI definition, the former having a large margin, the later having zero margin. It could therefore be interesting to vary the margins between these two extremities to investigate how resulting activity changes, i.e. how large margin is required to include all activity. Initial volumes of interest were generated by defining a spherical VOI co-centric with the physical sphere, identical to VOI_{CT} and the diameter of this VOI was gradually increased. If the VOI included activity that clearly came from neighbouring spheres, the VOIs were adjusted to the largest margin possible at that point. Margins starting from 0 and up to 2cm were investigated, in 0.5cm steps. This was done on patient data from Week 1 (second scan). Margins drawn on two spheres, the 2mL and the 4mL are presented in figure 3.2a.

3.3 Patient data

Patient data were gathered from patients participating in the Lymrit-37-01 study, some inclusion criteria for the patients participating in the Lymrit-37-01 were:

1. Histologically confirmed relapsed incurable non-Hodgkin B-cell lymphoma of following subtypes: follicular grade I-IIIA, marginal zone, small lymphocytic lymphoplasmacytic, mantle cell.
2. Age $>$ 18 years.
3. Life expectancy should be $>$ 3 months.
4. Measurable disease by radiological methods.

Patients included in this work had at least two SPECT/CT-imaging measurements available, predominantly four and seven days after injection. The patients were then included based on the number of visible tumors, three tumors for each patient clearly visible on the CT were desirable. The patients received activity as a fixed number of Becquerel per kilogram body mass. The amount of activity injected per mass unit, referred to as «dose level» varied between the patients, as a part of the study design. It was then desirable to have patients representing the individual dose levels. Patients included in this work along with body mass, dose level, number of included tumors and injected activity, are found in table 3.1.

Table 3.1: Overview of patients included in this work. Patient body mass and dose level is also given.

Patient num.	Body mass (kg)	Dose level (MBq/kg)	Tumors included (#)	Injected activity (MBq)
2	103.0	10	3	1046
3	73.0	10	2	736
5	97.0	20	3	1982
7	75.0	20	4	1505
9	111.0	15	3	1696
11	96.0	15	2	1435

Two volumes of interests (VOIs) were delineated on each tumor; a CT-guided VOI $\mathrm{VOI_{CT}}$ to asses the physical size of the tumor, and a SPECT-guided VOI $\mathrm{VOI_{SPECT}}$ to account for the activity belonging to the lesion. These VOIs were drawn by a skilled physician with long experience in nuclear medicine. Generally the VOIs were drawn on the SPECT/CT-data from four days post injection. VOIs were then copied and adjusted to the image data from day seven.

Imaging data-sets from the SPECT- and CT-scans were combined in the computer program PMOD (PMOD industries). The program uses the CT-dataset as a reference, and interpolates the SPECT-data to fit the CT-voxelspace using trilinear interpolation. The

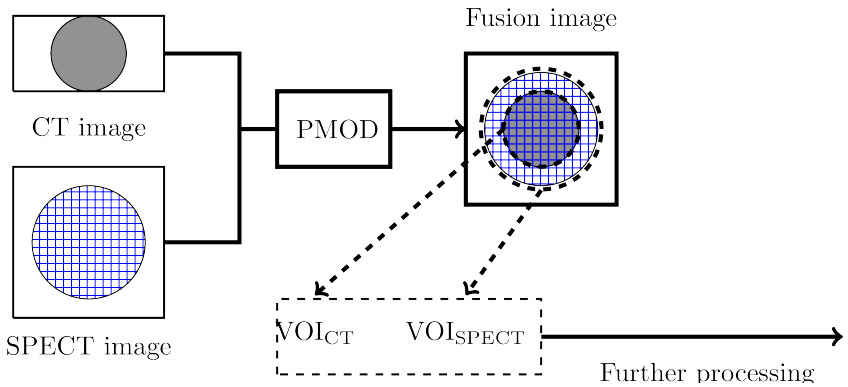

Figure 3.3: Schematic of the work flow with PMOD illustrated with a stylized image of a tumor with CT (gray) and SPECT (hatched blue). Dashed lines around the activity and physical image in the fusion image indicate the drawn volumes of interest.

sum of voxel values from these interpolated data sets was extracted from PMOD, along with coordinates for the voxel values inside the VOIs. This is illustrated in figure 3.3.

3.3.1 Auxiliary planar tumor kinetic data

Two tumors on patient 2 were distinguishable on planar scintigraphies. These tumors have been analyzed using conjugate view images, resulting in a time activity curve with six time points. These two tumors were identified and defined by the same medical professional that identified the tumors on the SPECT/CT-datasets. This curve was tested for mono exponential characteristics. Two separate tests were used, a linear regression test where the logarithm of the activity is investigated, and a pre implemented mono exponential test in MATLAB. The name of the MATLAB function is `fit` with passing of the argument `exp1` to ensure mono exponential fit parameters.

3.3.2 Mean absorbed tumor dosimetry

To asses the macroscopic (i.e. mean) tumor dose, the following method was used: From the SPECT-VOI, VOI$_{SPECT}$ mentioned previously, a total number of counts in the VOI is extracted, C_4. The subscript indicate the number of days post injection. A previously established conversion factor R_s is used to convert the number of counts to activity in MBq.

$$A_4 = R_s C_4 \tag{3.1}$$

The kinetic method to find total number of disintegration is assuming a mono-exponential form of the time activity curve

$$A(t) = A_0 e^{-\lambda_{\text{eff}} t}, \tag{3.2}$$

with analytical integral

$$\tilde{A} = \int_0^\infty A(t)\mathrm{d}t = \frac{A_0}{\lambda_{\text{eff}}}. \tag{3.3}$$

The two parameters A_0 and λ_{eff} can be expressed with A_4 and A_7 with the help of time, in hours, passed after injection.

$$\lambda_{\text{eff}} = \frac{\ln(A_7) - \ln(A_4)}{t_7 - t_4} \tag{3.4}$$

$$A_0 = \frac{A_4}{e^{\lambda_{\text{eff}} t_4}} = \frac{A_7}{e^{\lambda_{\text{eff}} t_7}} \tag{3.5}$$

to yield an expression for cumulative activity in MBqHrs. This is illustrated in figure 3.4. Now assuming the activity to be uniformly distributed, and the conversion to energy from activity to be constant, it is possible to write, following the MIRD-schema

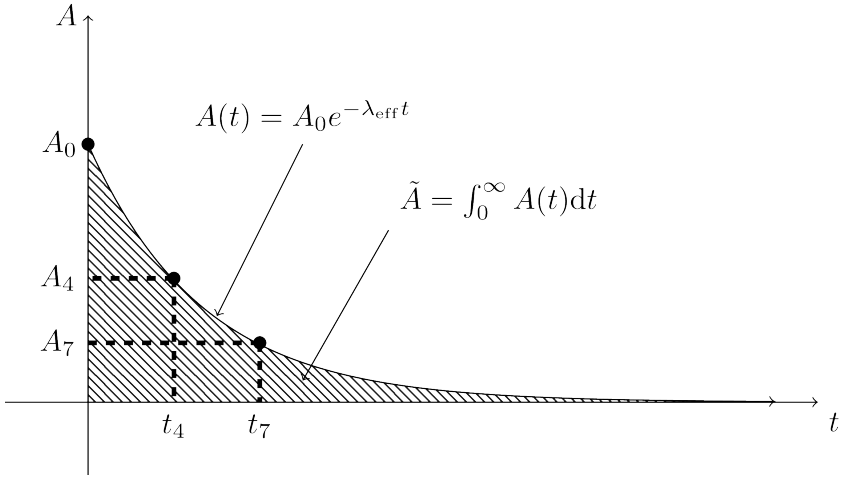

Figure 3.4: Diagram showing the most important elements of the kinetic model of the activity within the tumor, and its relation to measured quantities A_4 and A_7.

$$\bar{D} = \frac{\tilde{A}}{m_{\text{CT}}} \bar{S}. \tag{3.6}$$

The mass of the lesion, m_{CT} can be found by assuming uniform mass density, either water or soft tissue and using the CT-guided volume VOI_{CT}. Initial calculation assumes density as for water. $\bar{S}$, the conversion factor for the lesion assumes semi-locally and homogeneous deposition of energy, β- and γ-contribution and a fixed mean value of energy deposited per disintegration. 0.147MeV/disintegration is assumed. Numerical value of this parameter, with $\tilde{A}$ given in MBqHrs and mass given in Kg, becomes

$$\bar{S} = 0.147[\text{MeV/disintegration}]1.6 \cdot 10^{-13}[\text{J/MeV}]10^6[\text{Bq/MBq}]3600[\text{s/Hrs}] =$$

$$8.46 \cdot 10^{-5}[\text{J/MBqHrs}]$$

which will give $\bar{D}$ directly in units of gray.

3.3.3 Dose rate maps.

As a first approach to voxel based dosimetry, dose rate maps of the tumors were made. Using the SPECT-data, activity distributions were found by multiplying all voxels with a count $\rightarrow$ activity conversion factor R_v. Note that this is *not* the same constant as the previous R_s in equation (3.1), as R_s uses the interpolated SPECT-data, and R_v (R-voxel) is used on non-interpolated SPECT-data. Consider an activity distribution $\mathbf{A_4}$ measured 4 days after injection. A dose rate distribution $\dot{\mathbf{D}}$ can be found by convolving the activity distribution with a look up table of voxel s-values.

$$\dot{\mathbf{D}} = \mathbf{A} \otimes \mathbf{S} \tag{3.7}$$

or for each individual target voxel in $\dot{\mathbf{D}}$

$$\dot{D}\left(\text{voxel}_T\right) = \sum_{S=0}^{N-1} A\left(\text{voxel}_s\right) S\left(\text{voxel}_T \leftarrow \text{voxel}_s\right).$$

The look up table was retrieved from a database made by (Lanconnelli et al., 2012). The table in the database has been calculated with a Monte Carlo simulation for an isotropic point source of ^{177}Lu residing in tissue, with voxel size 4.8mm. Voxel s-values were available for a grid representing an octant with center Cartesian coordinate (0,0,0) up to (5,5,5). These values can through symmetry arguments be used to construct an 11 by 11 by 11 sized matrix. Equation (3.8) shows the central part of the matrix in a two dimensional plane through the origin.

$$\mathbf{S} = \begin{pmatrix} 8.65 \cdot 10^{-5} & 0.0024 & 8.65 \cdot 10^{-5} \\ 0.0025 & 0.1780 & 0.0025 \\ 8.65 \cdot 10^{-5} & 0.0025 & 8.65 \cdot 10^{-5} \end{pmatrix} \tag{3.8}$$

Matrix $\mathbf{S}$ has the units of mGy/MBqs

Equation (3.7) holds if the activity is assumed to be constant for that second, so activity and cumulative activity have the same numerical value. The units of $\dot{\mathbf{D}}$ then correctly becomes mGy/s, dose per unit time.

To extract relevant voxel values representing the tumor, binary masks were made from the CT-guided volume of interest, spanning the image of the physical tumor, VOI_{CT}. Positioning of the masks was done by placing the pre drawn VOI_{CT}s center on top of the maximum tumor activity uptake. Dose rate maps were made for all the tumors included in this work apart from 7d. From this map of dose rate, cumulative dose rate histograms were made, and $\dot{D}_{90}$-values were found. In addition to $\dot{D}_{90}$, $\dot{D}_{70}$ and $\dot{D}_{50}$ was also calculated.

The calculation was carried out by the MATLAB script `dose_rate_map`, SPECT image files, and a list of coordinates extracted from PMOD was used as input. Convolution was carried out on the whole image set, using the pre-implemented MATLAB function `convn` that performs convolution in three dimensions. The script that creates the voxel s-value convolution kernel, `kernel_maker` as well as the voxel s-values on the form (I,J,K,val) extracted from the database can be found in the appendix.

3.3.4 Comparison with OLINDA unit density spheres

To verify the factor $\bar{S}$ used in equation (3.6), a comparison with the dose calculating computer program OLINDA was made. OLINDA takes input in the form of residence time (cumulative activity divided by injected activity) and provides a look up table for dose to unit density spheres of different mass. A unity cumulative activity and injected activity were used as input, meaning 1MBqHrs and 1MBq injected. This output was converted to energy,

$$E_{\text{tot}} = D_{\text{sphere}} m_{\text{sphere}} \tag{3.9}$$

and divided by number of disintegrations, resulting in mean energy absorbed per disintegration, $\bar{E}_{\text{OLINDA}}$. This mean energy was computed for a range of relevant sphere sizes (2-20g) and compared to the 0.147MeV/disintegration used in the mean tumor dose model.

3.3.5 Patient data images.

Figure 3.5 shows sagital, coronal and axial view images of tumor 5b A fusion image is used. SPECT data have been interpolated to CT voxel space. VOI_{CT} and $\text{VOI}_{\text{SPECT}}$ for the tumor are overlaid in the image, the inner being VOI_{CT} and the outer $\text{VOI}_{\text{SPECT}}$. A grid with 20mm spacing is shown in the images, showing the size of the margin used around the tumors.

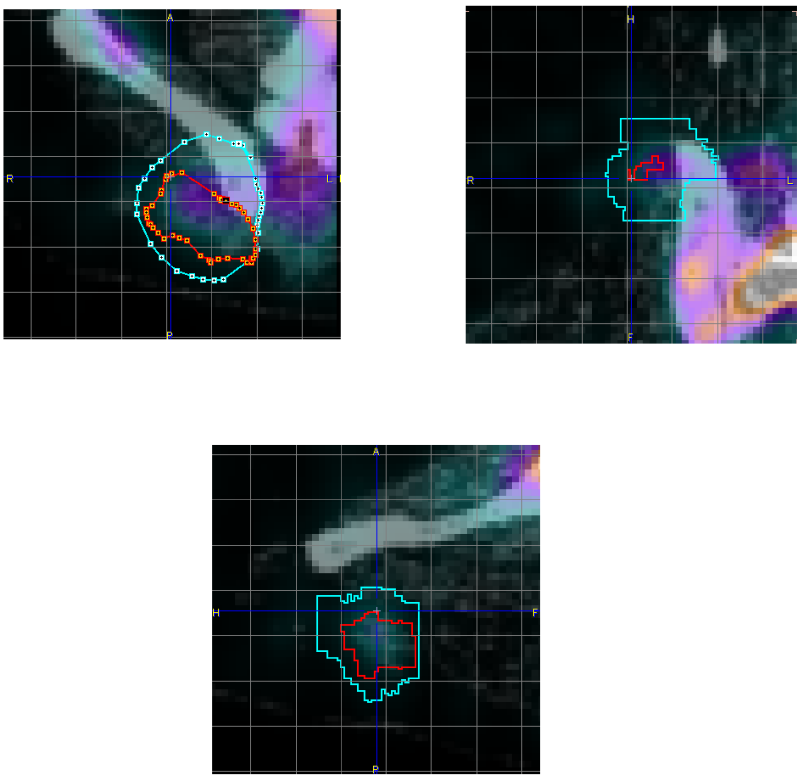

Figure 3.5: SPECT/CT images as viewed with PMOD. Images are of Patient 5, tumor 5b. Upper left is the axial view, the view that the VOIs are drawn. A grid with 20mm spacing is shown to highlight the extent of the margin used. Upper right is the coronal plane, and lower the sagital plane.

3.3.6 Partial volume correction

An attempt was made to correct for partial volume effects by deconvolving the activity distribution with a Gaussian point spread function.

From the spheres, a SPECT guided VOI $\mathrm{VOI}_{\mathrm{SPECT}}$ was drawn around the activity distribution of the sphere, giving the total activity $\mathbf{A}(I_{\mathrm{SPECT}})$ distribution in that sphere. Additionally, a physical VOI $\mathrm{VOI}_{\mathrm{CT}}$ was defined. The activity distribution and the two VOI-masks were imported to a computer program written in MATLAB. The program saves the initial activity in both VOIs, $A(\mathrm{VOI}_{\mathrm{CT}})$ and $A(\mathrm{VOI}_{\mathrm{SPECT}})$. A point spread function correction through a deconvolution was then performed on the activity distribution image using the pre-implemented MATLAB function `deconvlucy` with a symmetrical Gaussian kernel. This resulted in the new activity distribution $\mathbf{A}'$,

$$\mathbf{A}'(\mathrm{VOI}_{\mathrm{SPECT}}) = \mathrm{psf}^{-1}(\mathbf{A}(\mathrm{VOI}_{\mathrm{SPECT}})) \tag{3.10}$$

An illustration of the scheme is found in figure 3.6.

Different sizes of the Gaussian kernel were used, defined by various FWHM-values. Gaussian functions were generated with the MATLAB script `fspecial3d`, downloaded from Mathworks. Activity was then extracted from this new image of the distribution using the same physical VOI. This activity was then compared to the total activity in the distribution, and to the activity in $\mathrm{VOI}_{\mathrm{CT}}$ from the uncorrected image to investigate potential gain in activity counts. The computer program assures that the total amount of activity was preserved. The MATLAB script written to carry out the whole calculation, `psf_corr_sphere` is found in the appendix. The results from the correction are found in figure C.1 in the appendix. Shape plots before and after the convolution are found in figure C.2, C.3 and C.4. All figures are in appendix C. This was only done for the phantom spheres, and have not yet been implemented for patient tumors.

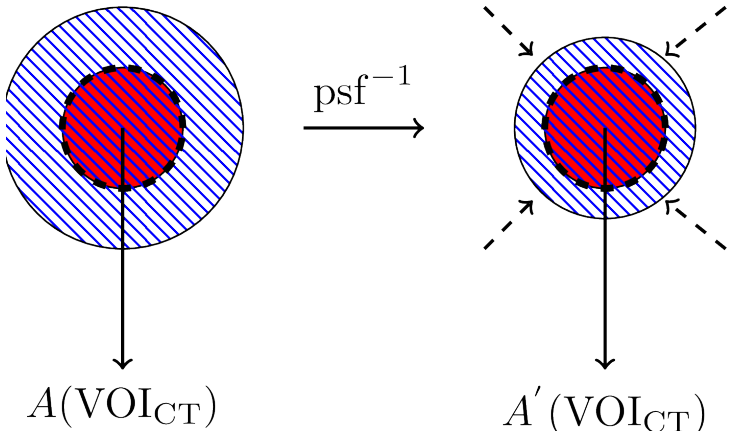

Figure 3.6: Schematic representation of the partial volume correction. Red solid volumes indicate the physical tumor, blue hatched volumes indicates the activity distribution image. A physical VOI, $\mathrm{VOI}_{\mathrm{CT}}$, around the sphere is drawn, and total activity extracted, $A(\mathrm{VOI}_{\mathrm{CT}})$. A point spread function correction is done on the activity distribution, and activity is extracted from the same physical VOI as before the correction, yielding a total activity $A'(\mathrm{VOI}_{\mathrm{CT}})$..

Chapter 4

Results

4.1 Phantom measurements

4.1.1 Activity quantification

The activity estimated by using the manually defined $\text{VOI}_{\text{SPECT}}$ with a margin around the activity image in the spherical insertions are found in table 4.1. The table contains measurements from all four weeks, along with the expected activity in each sphere. Relative errors of measured in respect to true activity are found in table 4.2.

Table 4.1: Activity measurements of the spherical phantom insertions. A denoting the measured activity compared with the «true» activity A_{ref} all in units of MBq

	Week 0		Week 1		Week 2		Week 3	
	A	A_{ref}	A	A_{ref}	A	A_{ref}	A	A_{ref}
(2mL)	1,39	1,28	0,74	0,72	0,27	0,26	0,06	0,06
(4mL)	2,77	2,66	1,48	1,43	0,54	0,51	0,13	0,13
(8mL)	5,55	5,20	2,96	2,87	1,08	1,09	0,25	0,26
(16mL)	11,09	11,01	5,91	5,75	2,16	2,08	0,50	0,50
(113mL)	78,34	75,65	41,75	43,11	15,23	14,88	3,56	3,46

Table 4.2: Relative error of the measurements compared to the expected activity, expected activity as reference. In units of percent using three significant figures in the calculation.

Sphere volume	Week 0	Week 1	Week 2	Week 3
(2mL)	-7,64	-2,42	-4,88	1,98
(4mL)	-4,22	-2,95	-5,14	0,00(2)
(8mL)	-6,23	-2,87	1,17	2,37
(16mL)	-0,78	-2,69	-3,72	-0,27
(113mL)	-3,44	3,24	-2,29	-2,86

4.1.2 Recovery Coefficients

Figure 4.1 show the ratio between expected activity and measured activity when VOI_{CT} is used. The Recovery Coefficients along the abscissa, indicating activity loss range from 10% (meaning 90% activity loss) in the 2mL sphere to 83% (loss of 17%).

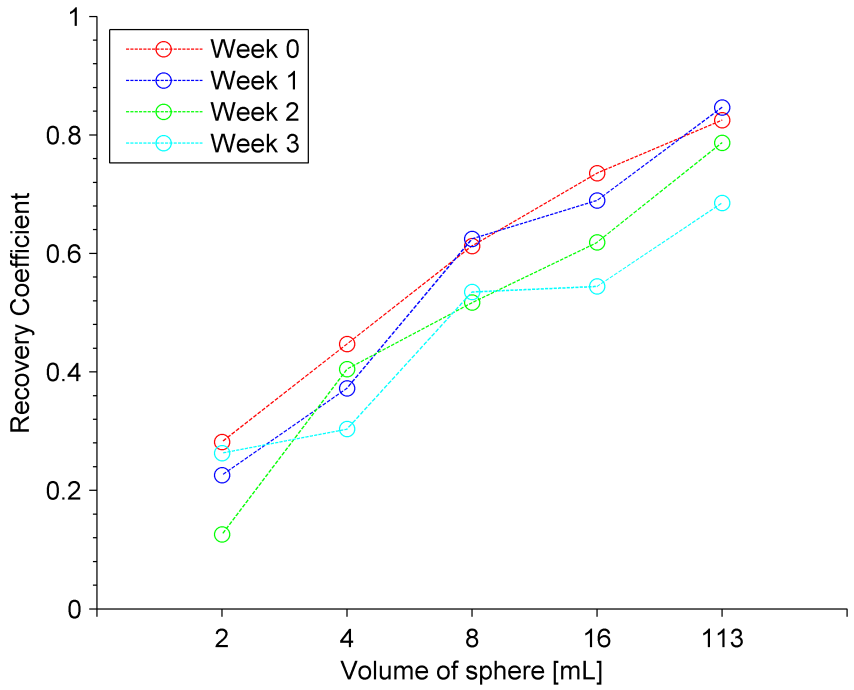

Figure 4.1: Ratio between expected and measured activity for phantom measurements when a physical VOI (VOI guided by the CT-image) is drawn. These could potentially later be used to correct for loss in counts due to partial volume effects.

4.1.3 Margins

The result of using different margins around the spheres are shown in table 4.3. Smaller spheres need a margin of 1cm or 1.5cm to recover below 10% loss. A margin of 2cm result

in errors lower than 10% for all spheres.

Table 4.3: Table showing the error between measured and expected activity for the spheres when a larger and larger margin is applied. $m = 0$ signifies no margin, and margins up to $m = 2$cm are used. Errors are given as relative percent values. The dataset for Week 1 was used. The manual $\text{VOI}_{\text{SPECT}}$ is also included.

Sphere volume	$m = 0$	$m = 0.5$	$m = 1$	$m = 1.5$	$m = 2$	$\text{VOI}_{\text{SPECT}}$
2mL	-79.6	-47.9	-21.7	-5.2	-4.6	-2.4
4mL	-62.6	-35.1	-17	-10.7	-2.5	-2.9
8mL	-40.9	-17.4	-8.9	-5.2	-2.0	-2.9
16mL	-31.3	-14.4	-7.4	-4.2	-1.2	-2.7
113mL	-17.4	-4.2	0.8	1.9	2.1	3.2

4.2 Patient results

An overview of the tumors included in this work is found in table 4.4. The index keys listed in the table are used throughout to refer to individual tumors. Tumor mass was found by using the volume of VOI_{CT} and assuming uniform density equal to water.

Table 4.4: Overview of tumors included in this work. The tumor index indicates the patient number, and letters enumerating the tumors within each patient.

Tumor index key	Tumor location (Name)	Mass of tumor (g)
2a	Lower R. neck	6,2
2b	Upper R. neck	9,8
2c	Para-esophageal	9,4
3a	Para-tracheal R.	6,2
3b	Para-vertebral R.	14,9
5a	Inguinal R.	12,5
5b	Subcut Nates R.	25,0
5c	Retroperitoneum	8,1
7a	Lower L. Inguinal	10,9
7b	Upper L. Inguinal	18,0
7c	Inguinal R.	3,2
7d	Lower b R.	22.5
9a	Mediastinum Anterior	14,4
9b	Inguinal R.	4.9
9c	Upper R. mediastinum	15.5
11a	L. Axilla	2,3
11b	R. neck	4,4

4.2.1 Mean absorbed tumor dose, $\bar{D}$

Results of the mean dose calculations are found in table 4.5. The table depicts in addition to the dose itself the most relevant parameters included in the model. A_0, calculated from equation (3.5), the cumulative activity $\tilde{A}$ as by equation (3.3) and effective half life from equation (3.4). Figure 4.2 show the tumor mean dose plotted against tumor mass.

Table 4.5: Main result of the mean tumor dosimetry. Measured activities in the various tumors 4 and 7 days post injection, cumulative activity $\tilde{A}$ and final dose $\bar{D}$. Included in the table are also the estimated activity at time zero, A_0 and an effective half life $t_{1/2}^{\text{eff}}$ found from the effective decay constant λ_{eff}.

Tumor	A_4 (MBq)	A_7 (MBq)	$t_{1/2}^{\text{eff}}$ (Hrs)	A_0 (MBq)	$\tilde{A}$ (MBqHrs)	$\bar{D}$ (cGy)
2a	0,41	0,17	2,9	1,08	110,44	151,25
2b	0,37	0,16	3,0	0,94	99,74	86,60
2c	0,27	0,16	5.35	0,45	84.10	75,55
3b	0,49	0,31	4,6	0,91	146,78	201,06
3c	1,82	0,96	3,2	4,37	496,86	281,77
5a	1,12	0,61	3,4	2,59	304,69	207,15
5b	0,97	0,55	3,6	2,11	268,32	90,99
5c	1,11	0,66	3,9	2,27	313,41	327,57
7a	3,63	2,22	4,1	7,13	1025,30	794,23
7b	4,38	2,35	3,8	10,32	1170,85	550,28
7c	0,49	0,29	3,2	1,02	135,06	358,65
7d	3.17	1.71	3.3	7.43	848.06	319,14
9a	1,94	1,19	4,1	3,87	558,45	328,48
9b	0.44	0.23	3,1	1.08	119.80	204,30
9c	0.82	0.29	2.0	3.47	240.03	130,91
11a	0,65	0,40	4,1	1,29	185,67	672,17
11b	0,54	0,28	3,1	1,34	144,46	276,72

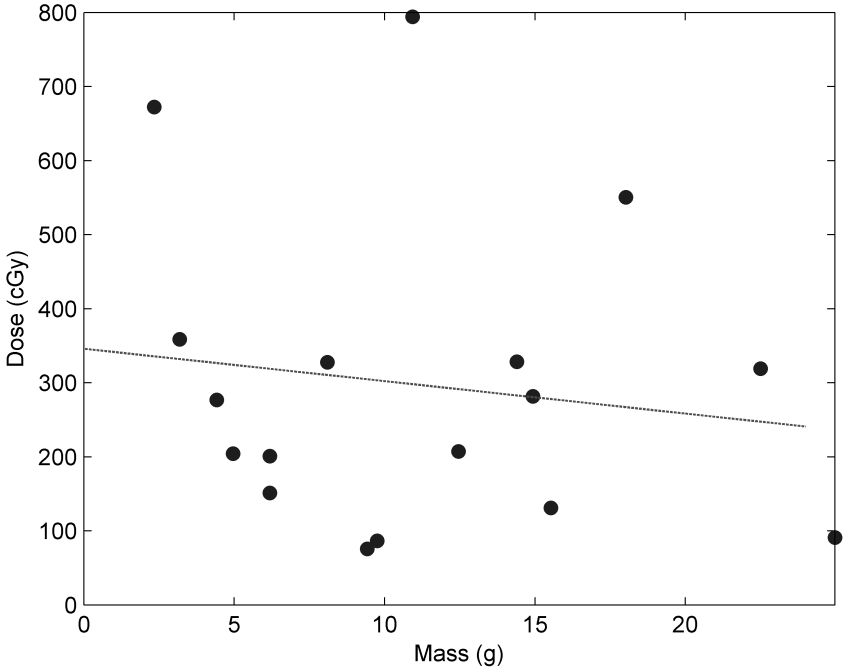

Figure 4.2: Mean tumor dose plotted against the mass of the tumor. Dashed line represents a regression curve, r-value= -0.51.

Activity concentration in all tumors, as well as calculated activity concentration from the mono exponential fit curve are shown in figure 4.3. Phantom sphere concentrations are represented as dotted lines.

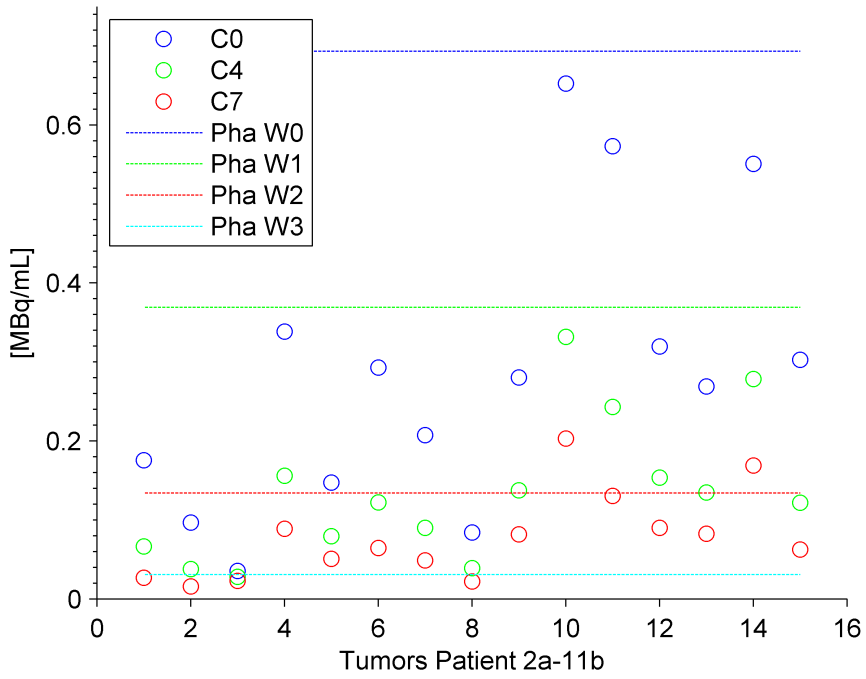

Figure 4.3: The activity concentration of the individual tumors at four and seven days past injection. Included are also the activity estimates at time zero. Dotted horizontal lines show the concentration of the spheres in the phantom measurements.

4.2.2 Auxiliary data

The regression analysis of the time activity curves established by conjugate view images of patient 2, tumors 2a and 2b is found in figure 4.4. Linear curve fit to the logarithm of the time activity resulted in r-values of -0.999 for tumor 2a and -0.994 for tumor 2b. The time point span six points in time from 2 hours past injection, to 190 hours after injection. The two last time points close to coincides with the SPECT/CT-imaging sessions used in the main tumor method, as they were done on the same days.

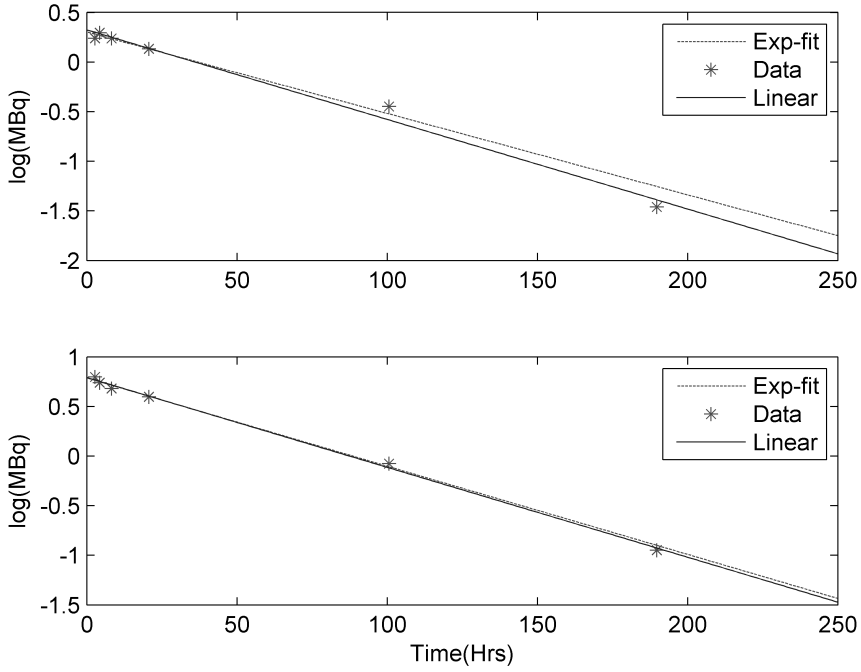

Figure 4.4: Regression analysis of the tumors located in the lower and upper neck (in lower and upper plot respectively) of patient 2 from activity acquired through scintilation scans using conjugate image view images. r-values for the logarithmic-linear regressions were found to be -0.999 and -0.994, indicating a strong mono exponential relation between time and activity.

4.2.3 Dose rate maps

The cumulative dose rate map of tumor 5b is found in figure 4.5. Two volumetric representation are included in the figure, a slice by slice image of the tumor, and a cumulative volume histogram. Cumulative dose rate volume histograms for tumors ordered by patient are found in figure 4.6. A complete set of all the dose rate volume histograms for day 4 is found in appendix A. $\dot{D}_{90}$, $\dot{D}_{70}$ and $\dot{D}_{50}$ were calculated. All are listed in table 4.6. All three parameters is plotted in figure 4.7 together with mean dose $\bar{D}$ and activity measured at day 4. The numerical values were normalized with the highest value of their respective sample, so all the parameters could be plotted together without units.

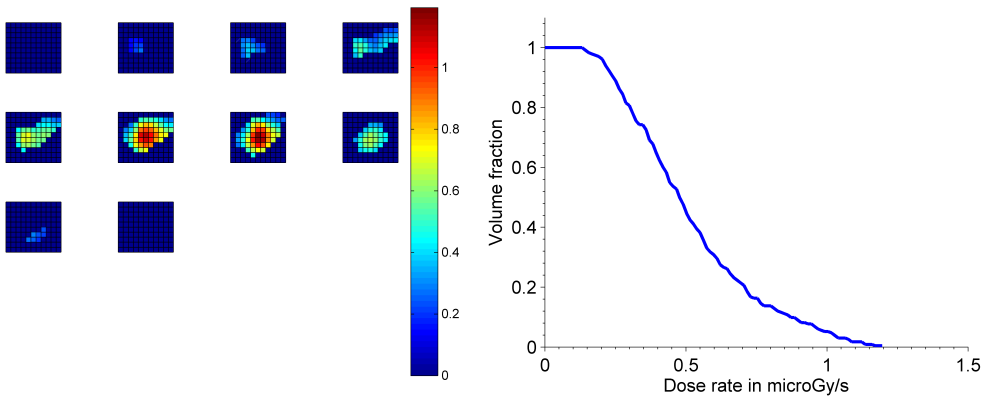

(a) (b)

Figure 4.5: Dose rate maps for tumor 5b (a) and a cumulative volume histogram (b) showing the distribution of dose rate 4 days post injection. Additional dose rate maps included in this work are found in the appendix.

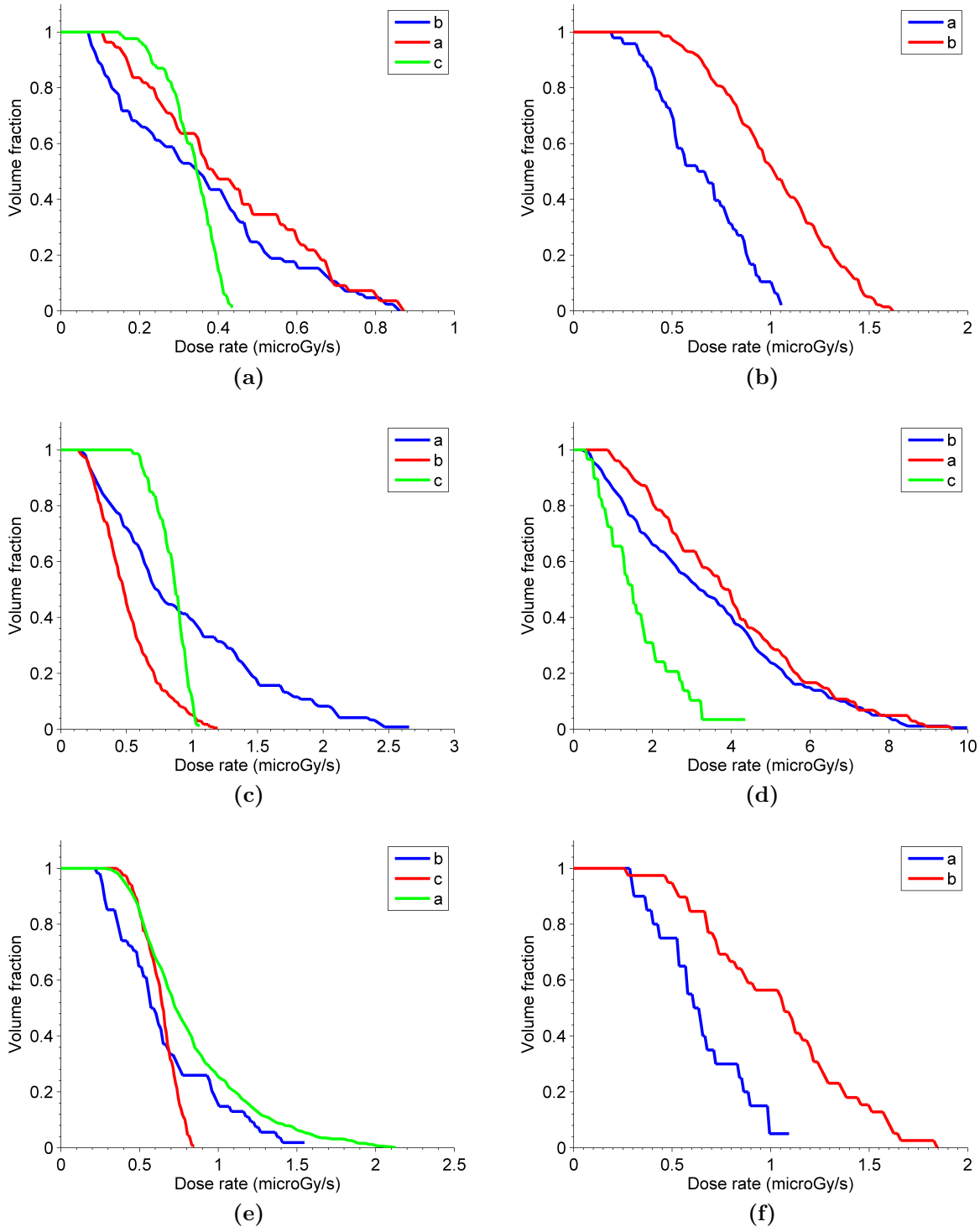

Figure 4.6: Cumulative dose rate volume histograms for patient 2(a), 3(b), 5(c), 7(d), 9(e) and 11(f)

Table 4.6: Table showing the maximum dose rate in μGy/s in a fixed volume fraction. The volume is a volume defined by the physical VOI $\mathrm{VOI_{CT}}$, and thus does not include all the activity. All doserates at four days past injection.

Tumor index (Index)	$\dot{D}_{50}$ (μGy/s)	$\dot{D}_{70}$ (μGy/s)	$\dot{D}_{90}$ (μGy/s)
2b	0.35	0.18	0.09
2a	0.39	0.28	0.17
2c	0.34	0.30	0.23
3a	0.67	0.50	0.35
3b	1.02	0.85	0.66
5a	0.74	0.55	0.26
5b	0.47	0.37	0.25
5c	0.87	0.80	0.66
7b	3.29	1.89	0.89
7a	4.04	2.59	1.54
7c	1.52	1.00	0.52
9b	0.60	0.49	0.27
9c	0.65	0.57	0.47
9a	0.74	0.59	0.46
11a	0.64	0.53	0.37
11b	1.07	0.73	0.53

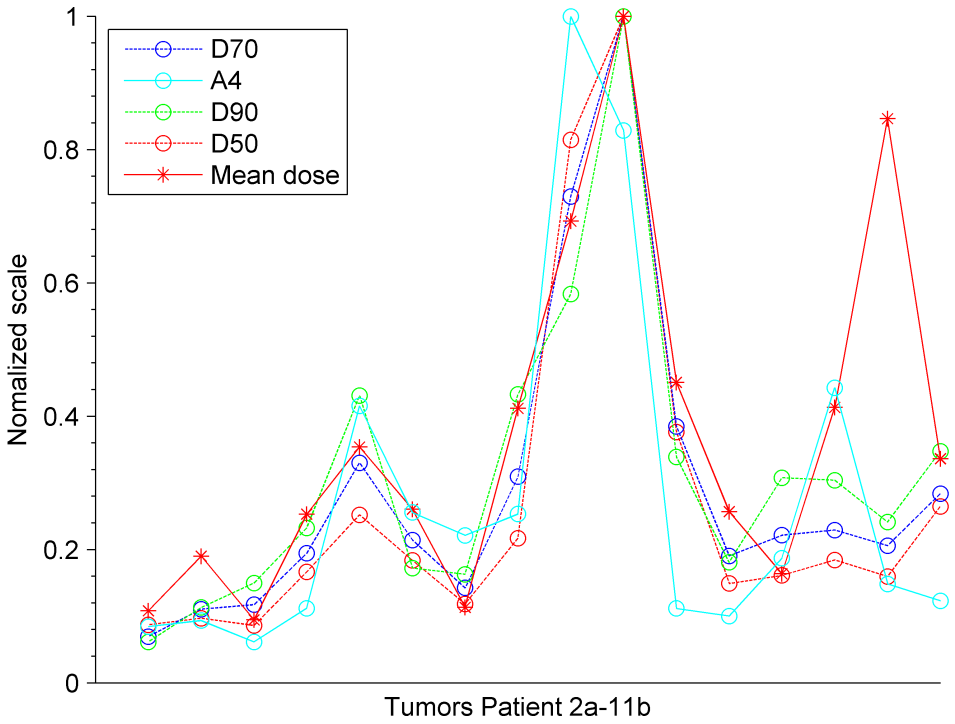

Figure 4.7: Various parameters extracted from the tumor dose rate maps. All values have been normalized. A_4 is activity measured on day 4, mean dose from the mean tumor dosimetry method, and DXX-values are the minimum dose rate in XX percent of the tumor volume.

4.3 Comparison with OLINDA unit density spheres

The calculation of mean energy per disintegration in uniform density spheres as calculated by OLINDA is found in table 4.7. Figure 4.8 show the relative error with respect to $\bar{S}$ over a wide range of sphere masses.

Table 4.7: Mean energy per disintegration as calculated by OLINDA for uniform density spheres containing 1MBqHr of cumulative activity evenly spread out. Relative difference in the far right column is compared to the 0.147MeV/disintegration used in the main model.

Sphere volume (mL)	Dose (mGy)	Energy (pJ/MBq)	Mean energy (MeV/disintegration)	Rel. diff (%)
4	21.1	23.4	0.146	0.3
6	14.1	23.5	0.146	0.0(8)
8	10.6	23.5	0.147	0.1
10	8.5	23.6	0.147	0.4
20	4.25	23.6	0.147	0.4

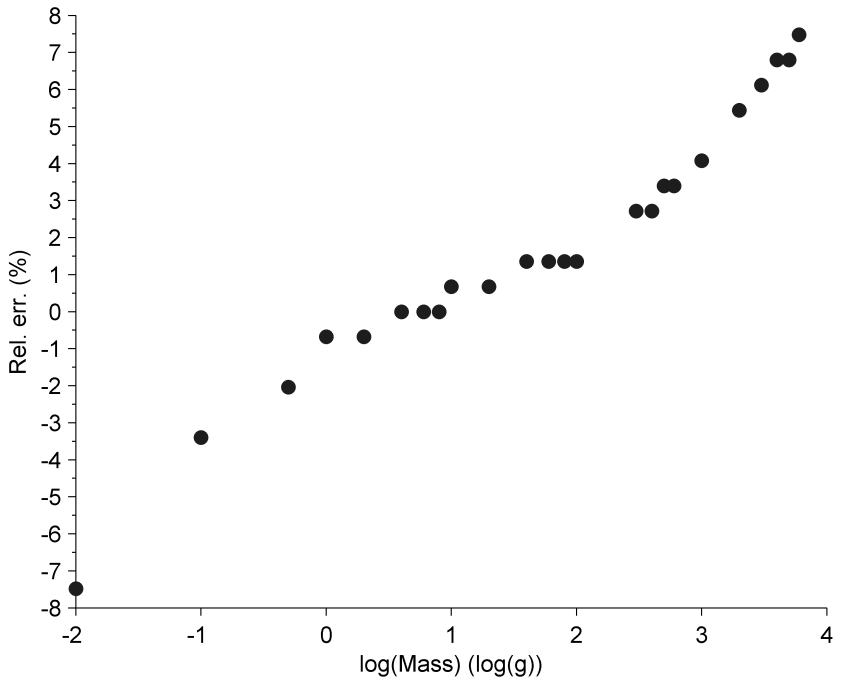

Figure 4.8: Plot of the relative difference between the mean energy absorbed per disintegration for different sphere sizes compared to 0.147MeV/disintegration. Note that the x-axis is logarithmic in base 10. Masses stretch from 0.01g to 6000g

Chapter 5

Discussion

Antibody-radionuclide-conjugate therapy with Betalutin™ is a novel treatment used to treat non-Hodgkin Lymphoma. Knowledge of how tumors respond to the treatment is valuable information to maximize treatment outcome. Tumor dosimetry is an important aspect of this knowledge. The dualistic nature of the isotope used, ^{177}Lu makes it possible to monitor the treatment without the use of another tracer. Dosimetric calculations are complicated, and often not readily available in the clinic. A method to assert mean absorbed dose to tumors has been presented, tested and implemented in the clinic using already available software tools. The method has been used to assert the mean tumor dose to 6 patients in a total of 17 tumors.

This discussion is split into two segments, the first concerns the mean tumor dose, and the second voxel dosimetry. The different steps in the mean dose calculation, activity quantification, mass estimation, activity kinetics to determine cumulative activity, and model used to convert cumulative activity to dose will be discussed separately. For the mean tumor dose, quantification of activity and the energy absorption model are first discussed. These two elements in the mean tumor method are specific for ^{177}Lu, but independent of the conjugate molecule complex Betalutin™ and non-Hodgkin lymphoma. Later the patient results, activity kinetics and target organ volumes are discussed, these are specific for Betalutin™ and non-Hodgkin Lymphoma.

5.1 Mean tumor dose

Phantom study

A pivotal element of tumor dosimetry is correct quantification. We have investigated quantification using large VOIs around the volumes containing ^{177}Lu. The phantom study conducted in this work showed that very good quantification accuracy is reached using the activity VOI, VOI_{SPECT}, even for small structures. Table 4.1 and 4.2 show that the activity predicted by counts inside the manually defined VOI_{SPECT} around the physical sphere was reflecting the activity of the sphere. Excluding week 0 make the highest error below 5.2% and no relative error with absolute value larger than 3.8% for spheres >4mL was observed. The largest errors were found in measurements from the first week, when activity distributions seemingly intertwined and were difficult to

resolve. This is a challenge which is also in general present in real patient data. Similar situations arise when tumors are close to other, localized radiation sources, i.e. bone marrow or glands. However, the amount of errors in the measurements even in week 0 was below 10%, indicating good agreement also in challenging situations. Tumors included in this work had activity concentration smaller than the spheres in week 0, as seen in figure 4.3. The margin investigation in table 4.3 show that a large margin was needed, especially for small structures. Admittedly the loss of activity measured fell sharply with increasing margin, even 5mm showed improvement, but for spheres with diameters around and less than the presumed FWHM of the system, the errors were still large. The overall results indicate a higher level of accuracy than previous studies of small spheres and structures listed in table 2.1. Howecer, all of these studies have been with other types of nuclei, with various imaging capabilities, as well as different definitions of VOIs. A study on ^{177}Lu with «small flasks» (70mL) showed accuracy in the order of a few percent (-1.6%) (Shcherbinin et al., 2012). Direct comparison is also here difficult, as the study used experimental reconstruction methods and VOIs were defined with a sophisticated mathematical image segmentation. Quantification results using the manual VOI $\text{VOI}_{\text{SPECT}}$ is difficult to compare directly as the method is novel. In a recent study conducted to investigate scatter correction techniques, VOIs with a margin were used with ^{177}Lu and small spheres (de Nijs et al., 2014). Using scatter correction they reached errors below 10% for all spheres.

The closest alternative quantification method to the one used in this work is combining the activity in the physical VOI_{CT} with a Recovery Coefficient. This is the most commonly used method in tumor quantification found in the literature. Being an empirical method, it relies on RCs collected under similar imaging conditions as the patient scans, with geometries and activity concentrations similar to the imaged lesions. The major disadvantage of the RC-method from a practical point of view is that it needs an extensive RC collection. Another is the limitation of similar geometry; not all human anatomy structures can be approximated by a sphere. Most studies utilize one Recovery Coefficient curve. The four RC-curves presented in this work showed high variability in the RC-values with different activity concentration. An implementation where the same level of accuracy as found with the manual $\text{VOI}_{\text{SPECT}}$ is to be expected would require an unpractical number of RC-coefficients. Partial volume effects depend on the placement of the object in the field of view, this is not easily accounted for by the RC-method, but handled naturally by the $\text{VOI}_{\text{SPECT}}$-method.

The spill-out of activity in the phantom spheres had a non-spherical shape; «activity clouds». These clouds had shapes that differed greatly from the physical shape of the spheres. Difference between the SPECT and CT-system is an inherent component of the hybrid system. In addition to resolution differences, they image different physical phenomena, resulting in different images. When the *physical* (CT) and *functional* (SPECT) representation of the tumor are forced together, problems then naturally arise. These difficulties are avoided when using the two imaging modalities to solve separate tasks where their respective strengths are fully used; just as in the method presented in this work.

Phantoms, although extensively used to show accuracy and aspects of the quantification, are different from the human body. Careful considerations when applying phantom results must then be made. The phantom setup in this work, with hot spheres in attenuating material, serves as a good model for tumor in a human body. Activity concentration

of the spheres did represent the activity concentration in the tumors. When comparing the overall visual situation on the imaging data, the phantom and patient images had similarities. Edges around both spheres and tumors were blurred and had a non-spherical penumbrae, almost almond-shaped. Even as the spheres and lesions had «fuzzy edges», it was clear whether the activity belonged to the sphere/lesions or other surrounding structures. This made it possible to attribute activity to each structure with a high level of certainty.

When considering mean dose to the tumor, the quantification method using the manually defined VOI_{SPECT} investigated in this work with should be preferred. It is intuitive, verified by phantom experiments under similar imaging conditions and best utilizes the functional image of the tumor.

Energy absorption.

The energy absorption model used in this work utilizes an approximation with a constant S-factor to convert cumulative activity to absorbed dose. Total local absorption of the electrons are assumed; the electrons are absorbed where they are emitted. Supporting this assumption is the relative short path length of the electrons emitted from ^{177}Lu. The maximum path length of the electrons from ^{177}Lu (2.2mm) is significantly shorter than the size of the relevant structures. When considering the voxel size of the SPECT-system, having cubical voxels with side lengths of 4.79mm, it is safe to assume that an electron emitted in the center of the voxel deposit all its energy inside the voxel. It is of course a possibility that electrons emitted outside the voxel centre «escape» and deposits energy in a neighboring voxel, and the possibility increases with decreasing distance to the voxel edge. The possibility for an electron to travel two voxel-lengths before giving away all its energy is highly unlikely. Escaping electrons that deposit their energy outside the tumor would then be electrons primarily emitted at the surface of the tumor. Absorption fraction for electrons in spherical geometries have been calculated to be 0.993 for spheres of 2-40mL (Stabin and Konijnenberg, 2000). It should then be clear that a local deposition of electron energy is reasonable.

In the energy absorption model, 90% of the energy is attributed to electrons, and 10% to γ-photons. Initially a pure electron contribution was assumed, but comparison with the unit density spheres in OLINDA caused a reinvestigation of the factor. Pure electron contribution was then abandoned in favor of a factor including photon contribution in better accordance with the literature(Sandstrom, 2011) (Jackson et al., 2013) (Ilan et al., 2015).

Photon contribution generally increases with increasing structure size, as stated earlier in the theory section. OLINDA has pre-calculated S-values for a large range of spherical masses, as seen in figure 4.8 and table 4.7. In the relevant regime, there is little difference in the mean energy per disintegration, and it should be safe to assume a constant value. The unit sphere model in OLINDA was used because it was readily available and thoroughly tested for use with internal emitters. The model has proven to be in good agreement with more sophisticated techniques. In a study conducted by (Howard et al., 2011) investigating an ^{131}I conjugate, OLINDA was compared to a full Monte Carlo transport code over a wide range of tumors, and excellent results were shown for self absorption. Results did

deviate when cross fire was included, but good agreement was still achieved even with crossfire. Crossfire from ^{177}Lu is likely to be much smaller than for ^{131}I, as the particles emitted are less energetic. (Ilan et al., 2015) reports that crossfire from ^{177}Lu is negligible.

It could be argued that it would be better to implement a scheme to make the factor $\bar{S}$ dependent on tumor mass. The study (Howard et al., 2011) uses an S-factor dependent on mass; tumor masses included ranged from 2 to 423mL. (Ilan et al., 2015) uses the S-factor of a 10g sphere (numerically equivalent to 0.147Me/disintegration) to calculate dose for tumors 2-25g, as differences are found to be negligible 0.7%. Figure 4.8 show that using the same S-factor for tumors ranging from 1g to 300g would only cause errors less than 3%. It is clear that a scheme for a varying $\bar{S}$ is only relevant if tumor masses deviate substantially from the tumors already investigated, and for tumors in the mass range included in this work, a constant factor with numerical value $\bar{S} = 8.47 \cdot 10^{-5}$J/MBqHrs is justified.

5.1.1 Patient results

A total of 17 tumors have been ascribed a mean tumor dose. The amount of measured activity in tumors did vary, from 0.37MBq in tumor 2a to 4.38 in 7b. Interestingly enough, these two tumors had almost the same mass. Variability of tumor dose were found among the tumors, ranging from 86cGy in tumor 2b to 794cGy in tumor 7b. Variability was observed not only inter-patiently but also intra-patiently. For example, two tumors in patient 7, 7a and 7b showed a significantly higher absorbed dose than the rest. However, the two tumors 7c and 7d showed moderate absorbed dose. 7c and 7d represents two extremes in the whole sample of tumors. 7c is one of the smallest tumors in regard to mass, and 7d one of the largest. In patient 5, two tumors had very high dose (5a and 5b), and one a lower dose. The tumor with the lower dose, 5c, was the largest tumor in patient 5, and also the largest in the whole sample. Figure 4.2 indicates no dependency of tumor mass and mean dose. Tumor dose that correlates negatively with tumor mass is an indication of poor perfusion of the ligand. The fact that this is not observed here indicates that the tumors are well vascularized. The intra-patient variation observed, could indicate that the tumor cells express CD37 (or bind to Betalutin$^{\text{TM}}$)differently, even for tumors in the same patient. The mean dose to all tumors were in the same order of magnitude as doses reported for lymphoma patients, however with different nuclei and antibodies (Koral et al., 2003), (Dewaraja et al., 2010c), (Dewaraja et al., 2014b), (Dewaraja et al., 2010b). Effective half lives were around half of the physical half life for all tumors.

The patient with the highest average dose was patient 7, having the third highest amount of activity administered. Doses to tumors in patient 5 and 9 that received a larger amount of activity have doses merely half of the doses in tumors in patient 7 (see figure 5.1).When the dose levels are arranged together (figure 5.2), mean dose in each dose level escalates with the dose level (10MBq/kg:195cGy, 15MBq/kg:322cGy, 20MBq/kg:406cGy) It is suggested that trend of maximum dose follows the dose level as well (368cGy $\rightarrow$ 672cGy $\rightarrow$ 794cGy). However, minimum dose in each dose level were roughly equal across the dose levels, highest and lowest dose level had nearly the same minimum dose (75cGy and 90cGy) with a significant higher minimum dose in the 15MBq-level (130cGy). The data are too sparse to draw conclusions, but the observation that mean and maximum

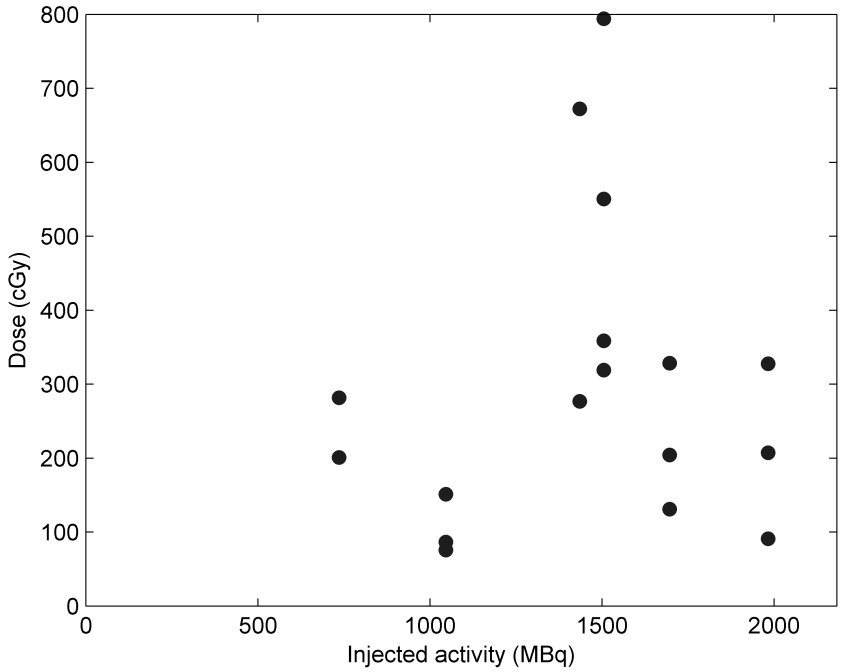

Figure 5.1: Mean tumor dose against activity injected.

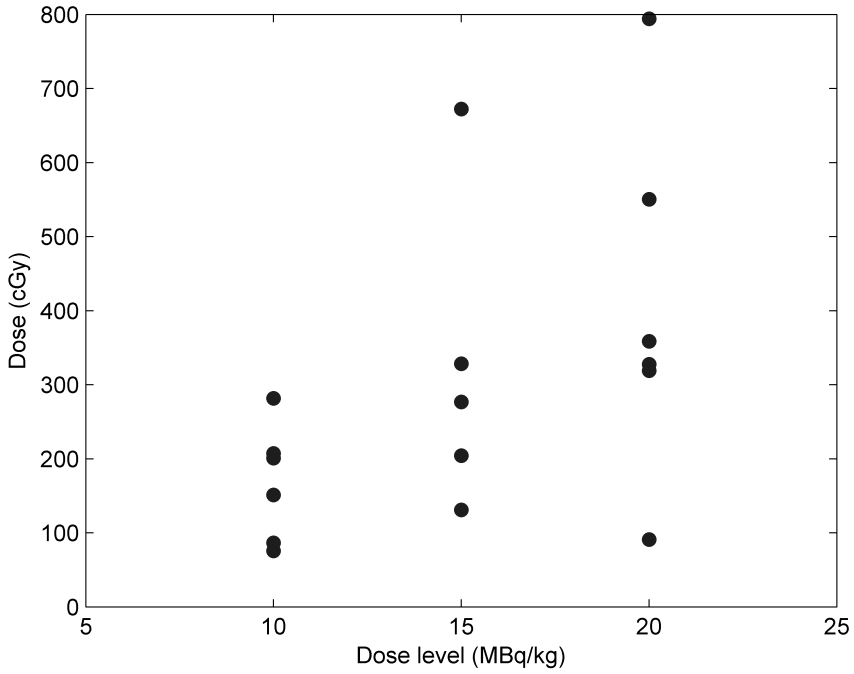

Figure 5.2: Mean tumor dose plotted against the individual dose levels.

dose seem more dependent on dose level and not total administered activity is worth noticing.

Activity kinetics.

It is necessary to know the activity in the tumor throughout the period the activity resides in the tumor to calculate the cumulative activity. Continuous measuring is virtually impossible, thus the time activity curve must be inferred from a discrete number of time activity points. An assumption of the time activity curve shape is then made, and the data fitted to the model to produce a full curve. The main challenge is to meet the often scarce number of points, and make optimal use of the points available. A central assumption in the mean dose model is the mono-exponential form of the time activity curve.

Mono exponential models for tumors have widespread use both historically and contemporarily (DeNardo et al., 1996), (Buckley et al., 2007), (Cook et al., 2006),(Sandstrom et al., 2010), (Ilan et al., 2015). However, the model has some critics, who insist that a bi-exponential model must be utilized for tumors (Schipper et al., 2012) and the validity of mono-exponentials is limited to whole body uptake curves. The rationale is that the whole body curve is the only uptake with «real» instantaneous uptake, only limited by the time it takes to inject the radiopharmaceutical. It is recommended for exponentially modelled time activity curves to include three measurements per exponential term in the model (Siegel et al., 1999) or three per washout-phase. This would result in, if we assume a two phase clearance, a total of six time points for antibody-nuclide-conjugates. However, six patient scans are seldom used in the literature, due to practical reasons.

It is important to notice that the number of fitting parameters in the mono-exponential model is the same as the number of measured time points in this work. Future imaging protocol for the Phase II patients will include an initial SPECT/CT, soon in the course of the scanning sequence. This will make it possible to adjust the modelling of the time activity curve in this point in time. It would also be possible to better test and potentially verify the mono-exponential fit, and lead to a protocol with more measurements than model parameters, which help quantifying errors. Three imaging time points and a mono-exponentially modelled time activity curve are used in the most recent tumor dosimetry work with ^{177}Lu, however with a different conjugate molecule (Ilan et al., 2015).

Scintigraphies of patient 2 showed two distinguishable tumors, found and delineated by the medical professional. This gave the possibility to follow two tumors over the course of six scans, making the regression analysis presented in figure 4.4 possible The two time activity curves stem from background and attenuation corrected conjugate view images. Regression analysis of the two time activity curves showed very good mono-exponential properties. Naturally, at time zero, the amount of radioactivity in the lesion is zero, as it takes the injected Betalutin^{TM} some time to go through the blood stream and tissue barriers to reach the tumor. It is reasonable to assume however, that this will only take a short time. The first scintigraphy is taken two hours after injection, a time where the maximum activity concentration already has been reached, indicated by the planar curve in figure 4.4. As contribution to the cumulative activity is fairly small in this phase, spanning a short range in time, there are few reasons to not neglect the rapid initial uptake phase and assume a pure mono-exponential washout. The shape of the curves match previously found time activity curves with similar techniques in antigen expressing tumors (Behr et al., 1996). Planar quantification is difficult with lymphoid tumors, as they are small, and potentially could lie on top of other sources of radiation (e.g. the

blood stream or other lymph nodes). Combining planar conjugate view images with a number of SPECT/CT-measurements used to scale the time activity curve has proven very useful (Koral et al., 2003), (Koral et al., 2000). The rationale is that the *shape* of the time activity curve is found accurately with planar methods, and one or more SPECT/CT-measurements set the activity at certain time points, and the whole curve can be scaled accordingly. However, this is not the main method in this work, as only these two tumors were distinguishable.

It is also important to consider patient discomfort. The imaging sessions are time consuming, and the patient must make numerous visits to the hospital. The SPECT/CT-sessions include multiple scan, with approximately 25 min in each scan. This trade off-between resources and accuracy is an element to consider, although giving a definite recommendation is beyond the scope of this work.

Target organ definition; $\mathrm{VOI_{CT}}$ and $\mathrm{VOI_{SPECT}}$

The following discussion will include comments on the quantification of activity and mass of tumors in the patients. These are essential for the dose calculation. $\mathrm{VOI_{CT}}$ defined the physical tumor, as delineated on the CT. The CT-scanner give an excellent image of the physical tumor, with a high precision for volume estimation given by the sub millimeter voxel size. The low dose CT with no contrast media made the identification and tumor/normal tissue segmentation more challenging. A few tumors had to be discarded because they were impossible to distinguish accurately on the CT. The extent of the challenge depended greatly on the tumor surroundings; lesions enclosed in fat were easily isolated but lesions especially in the abdominal area were harder to distinguish. A study reports the low dose CT without contrast as one of the main errors in the dose calculation when the target lymph nodes were close to conglomerates of other lymph nodes (Dewaraja et al., 2009). Therefore, no such tumors were included. A medical professional with extensive experience with human anatomy identified the tissue structures. The physician that performed delineation of the tumors had 8 years experience with nuclear medicine in addition to 16 years experience in surgery. This experience proved very useful, and such an experienced individual should be an integral part of the delineation process. As the absorbed dose depends on mass, it is important that errors in volume estimates are kept as low as possible. The strict visual inclusion criteria and sub millimeter voxel size made this possible.

The definition of the SPECT target volume, $\mathrm{VOI_{SPECT}}$, used to extract the activity in the tumor, is not straight-forward. Partial volume effects were very evident in even the larger tumors, with clear «spill out» of activity. In the mean tumor dose method, the volume was defined with a generous margin around the physical image of the tumor. The margins led to $\mathrm{VOI_{SPECT}}$s much larger than the physical $\mathrm{VOI_{CT}}$, often tenfolds larger. Potential problems then arise when $\mathrm{VOI_{SPECT}}$ and $\mathrm{VOI_{CT}}$ are used together. However, in the method currently stated, the $\mathrm{VOI_{SPECT}}$ and $\mathrm{VOI_{CT}}$ served two separate purposes, one carried information about the physical tumor, the other about *total* activity within the tumor. The use of a loosely defined margin in $\mathrm{VOI_{SPECT}}$ can be accused of introducing a level of subjectivity. It could however also be argued that the use of a margin removes some subjectivity, as the exact position of the VOI surrounding the object has less importance. This rationale is supported in the literature (de Nijs et al., 2014). The previous mentioned

VOI_{CT}-RC-method only counts for spill out and image smear caused by partial volume effect in a static system. VOI_{SPECT} also incorporates correction for smearing caused by patient motion in an intuitive manner.

The mass of the tumor in the mean dose model is assumed to be constant throughout the residence time of Betalutin^{TM}. This could potentially lead to under/overestimation of dose, as the dose is inversely proportional to mass. Preliminary results indicate no tumor mass difference between four and seven days post injection. Early mass changes are as of now obscured, as no imaging is taking place between injection and four days after injection. Other studies have observed volume changes over the course of treatment, although with different isotopes and conjugate molecules (Dewaraja et al., 2014a). The additional SPECT/CT-session between injection and day four, which is to be implemented in the future, will lead to more insight into the mass development of the tumor. Also worth mentioning is that baseline tumor masses are often used in dosimetric calculations in the literature (Ilan et al., 2015). If tumor mass changes are observed, it is possible to split the calculation into segments, calculate dose with the current mass in the time segment, and calculate an average (Howard et al., 2011).

Overall remarks.

The dosimetry model presented is simple, having a limited number of parameters. Activity in two points in time, (t_1,A_1) and (t_2,A_2) is needed as well as tumor mass m_{ct}. The constant $\bar{S}$ can safely be used in a tumor mass range of 1 to 300g, S-values for smaller and larger spheres are found in the appendix. Few parameters could potentially be a weakness, but could also be considered a strength. It is simple to implement, the whole calculation post activity measurements can be done in a spread sheet. This make it easily implementable in the clinical setting, and can than be a part of the routine.

5.2 Voxel dosimetry

Compared to mean tumor dose, voxel dosimetry calculates dose on the voxel level. Dose rate maps represent the first step towards voxelized dosimetry. These maps show the dose at a specific point in time. The larger tumors were regarded as the most suited for dose rate map creation, as they suffered less from partial volume effects. Shapes of the cumulative dose volume histograms were somewhat different across tumors. Some had a well defined plateau that stretched to almost half of the maximum dose rate before a steep fall. This shows that for these tumors, a certain (and potentially high) dose rate that covers most of the tumor volume is present. This further substantiates the notion of well vascularized tumors. Other curves almost immediately started to fall, which indicates a more inhomogeneous dose rate distribution. Curves that behaved in this way were predominantly the smaller tumors, so it could potentially be due to misplaced VOIs and partial volume effects rather than actual inhomogeneous uptake patterns. The plot of the normalized $\dot{D}_{90}$, $\dot{D}_{70}$ and $\dot{D}_{50}$ values in figure 4.7 show that minimum dose rate for all three volume fractions followed the calculated mean dose as well as total activity in day 4. The only exception was tumor 11a, that had a higher mean dose than 11b, even though 11b have (relatively) higher D_{XX}-values.

VOI_{CT} was moved from overlaying the physical tumor image to overlap the functional volume. This was to correct where the images sometimes appeared shifted, with the activity clouds of the tumor partially or completely outside the physical tumor image. This phenomenon can be caused by a range of image degrading artefacts for example patient movement or errors in the registration of the two imaging modalities. (The mapping between voxel spaces did also affect the VOIs, as VOI_{CT} was drawn on CT-data, and voxel values were extracted from SPECT-data.) Even though the relocation of the tumor VOIs introduced additional uncertainty regarding the activity distribution, the errors introduced by *not* moving it would be far greater. Confidence is put in this relocation, as there is reason to believe it gives a better image of the activity, and ultimately of the dose rate distribution. This adjustment is analog to the situation where a technician aligns the SPECT to the CT or visa versa, the difference being only that here a local adjustment is made. Some VOI_{CT} segmented tumors were visually similar to the full SPECT image of the tumor, having a central core of high intensity with radially decreasing activity towards the edges due to partial volume effects. For the smaller tumors, segmentation based on VOI_{CT} gave activity (and dose rate images) distributions not visually similar to their VOI_{SPECT} counterpart.

A potential alternative to the CT-definition of target volume used with the dose rate maps could be a redefinition of tumor volumes on the SPECT images. A visual inspection approach where volumes are defined based on image intensity, including voxels with a certain threshold value, could be used. This process could be semi-automated by the use of a computer program to delineate iso-contour surfaces, with a human operator making the final decision. Such an option is commonly used when CT-data are not present (Dewaraja et al., 2012). Even though this method is used in the literature, it would still result in potentially larger and differently shaped functional volumes than the physical tumor volume.

Lack of partial volume correction makes the absolute value of $\dot{D}$-values misleading, as they could potentially be underestimated. The deconvolution-based partial volume correction investigated in this work could possibly be utilized. The use of different FWHM lengths was partly inspired by (Teo et al., 2007) where post reconstruction was done on PET image data. The study proposed that the deconvolution kernel did not necessarily have to be the same as the imaged point spread function. Results from partial volume correction in figure C.1 for the phantom spheres show limited recovery. Useful recovery was however achieved for spheres $\geqslant$8mL assuming an effective FWHM of 12mm. The correction algorithm preserved the number of counts, did not skew the mean value, intensified central objects and suppressed outer regions (figure C.4) These are all prerequisites for a successful correction. This promising result encourage further implementation, refinement and testing of this correction; the ultimate goal being a volume the size of VOI_{CT} that contains all the activity of VOI_{SPECT} and preserves the distribution.

Apart from the challenges encountered with the tumor volume definition, the voxel s-value implementation should be considered successful. The method was straight-forward to implement, the kernel with voxel s-values used was from a Monte Carlo simulation with similar cubical geometry as the SPECT voxel space. The major drawback with the voxel s-value method itself, is the assumption of tissue homogeneity, which is often not the case in the human body. The lesions in this work were all in soft tissue, with little to no contact with surrounding structures with densities different from soft tissue. Voxel

s-values should therefore be applicable in this situation, and have as a method shown good accordance with more refined solutions, i.e. Monte Carlo simulations (Grimes and Celler, 2014).

The dose rate maps can be extended to generate dose maps. Figure 5.3 show the elements in a proposed method to do dosimetry on the voxel level with the imaging data and tools in this work. Internal dosimetry on the voxel level is found several places in the literature. An immense amount of work over several years has been done on ^{131}I where in-House programs have been developed by several research groups (Sgouros et al., 2004), (Kolbert et al., 2007), (Sgouros et al., 2003), (Dewaraja et al., 2014a). By assuming that the dose rate distribution is constant, and applying the kinetic of the whole tumor to each voxel, the conversion is simply a constant (Sgouros et al., 2003). This may be an oversimplification, since both spatial and temporal variability in absorbed dose have been found to be important parameters (Dewaraja et al., 2012). To do true spatial and temporal dosimetry on the voxel level, it is necessary to perform a registration of the tumor volumes across time. This can potentially be very challenging when tumors change shape or volume. (Dewaraja et al., 2014a) use non-rigid registration to radially expand shrunken tumors to fit their former self. This may lead to non-biological results, as when tumors are stretched, the integrity of voxels are violated. No satisfactory solution to this problem was found in the literature, nor developed over the course of the work in this thesis. The voxel dosimetry therefore ended with dose rate maps in this work.

The method as implemented and tested in this work does not interfere with or extend the workflow to a large degree. Simply a replacement of $\mathrm{VOI_{CT}}$ and extraction of the voxel-values are needed, the latter being a process that has been automated with a combination of Excel (Microsoft) and MATLAB-routines.

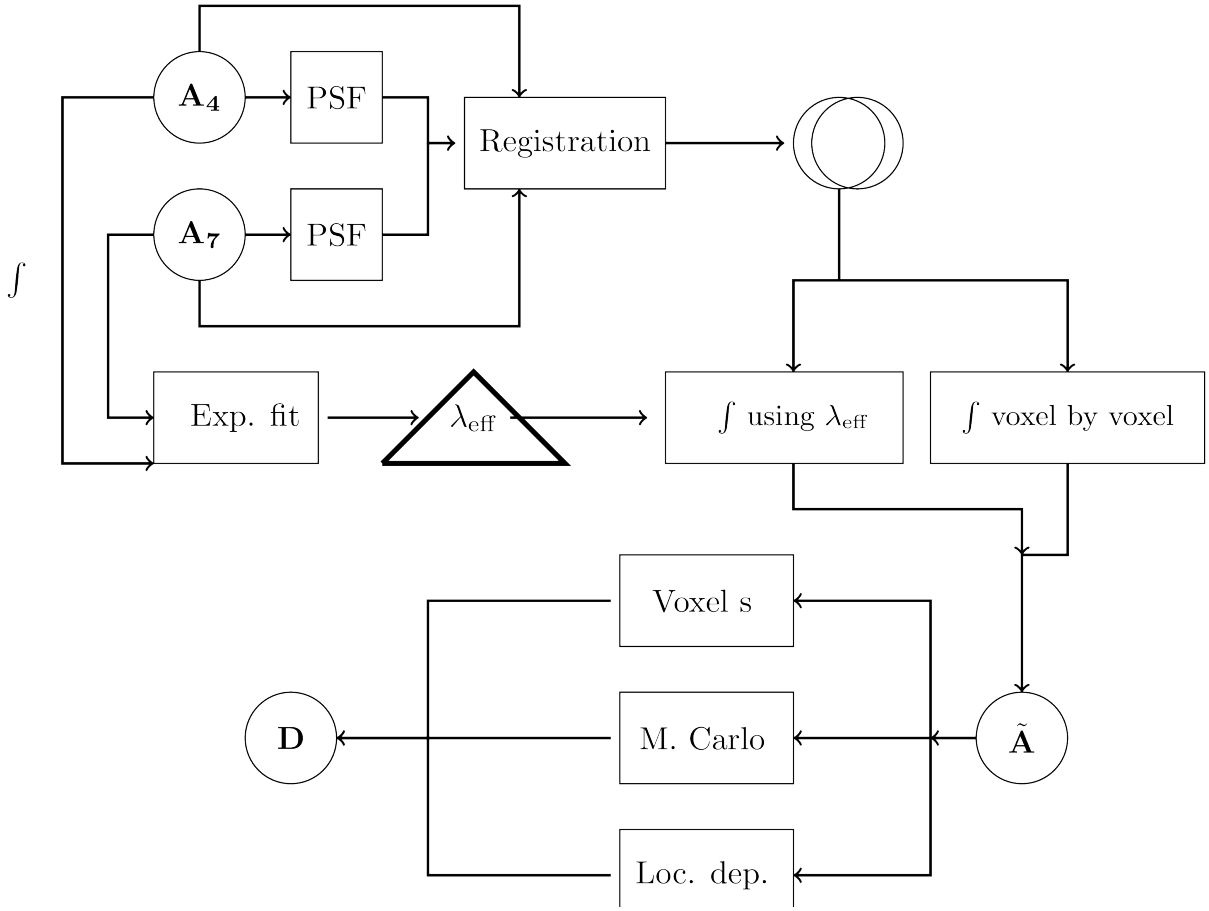

Figure 5.3: Figure showing a typical work flow for doing voxelized dosimetry, with choices along the process. Circles with bold fonts indicate voxelized distributions in space, triangles are constants and rectangles show mathematical manipulations. Starting with activity distributions for two points in time in the upper left corner. These distributions can be registered as is, or after after a PSF-correction. After the registration, the portion of the tumor images overlapping is integrated to yield a cumulative activity. This integration can either be done by direct integration, voxel by voxel, or using the effective half life found be fitting the sum of activity at the two time points to an exponential curve. The cumulative distribution is then converted to a dose distribution, by mean of three different methods.

Chapter 6

Further work

The mean tumor doses obtained for the patient tumors serve as a natural starting point for further analysis. As more tumors will be included, more thorough statistical analyses regarding dose versus administered activity and dose level can be made. Investigating the relationship between tumor response and mean tumor dose will be a valuable direction for further work.

For the dosimetry itself, working towards dosimetry on the voxel level is the next natural step. Implemented computer programs to create dose rate maps and cumulative dose rate histograms have been the first successful step on the way. The first task will be to register images of the tumor at different points in time, so a temporally tracking and integration of each voxel becomes possible. The most challenging aspect of this would most likely be the definition of the tumor volume. The nature of the transformation (i.e. rigid/non-rigid) to register volumes across time is also important to carefully consider, as conservation of the number of voxels as well as tumor volume is important for a biologically sound and meaningful dosimetric model. When a satisfactory cumulative activity map is present, it can be used directly with the voxel s-value-dose program presented in this work. The result is then a true voxel based dosimetry model. The resulting dose inhomogeneity parameters, both in spatial and temporal dimensions, can then be investigated in relation to tumor response.

Chapter 7

Conclusion

In this work a method for tumor dosimetry for patients undergoing treatment with Betalutin^{TM} has been developed, presented and tested. The method has been used to perform tumor dosimetry on patient tumors in the Lymrit-37-01-study. Quantification was performed using the novel VOI_{SPECT}-method without any partial volume correction procedures. The method was tested using phantom spheres. Kinetic modelling of the activity as a mono exponential curve has been found adequate. The energy absorption constant $\bar{S}$ has been verified in a spherical geometry through accordance with the extensively used and FDA-approved computer program OLINDA. Adjusting this value is only necessary if tumor volumes deviate substantially from the tumors included in this work. The method can easily be implemented in a clinical setting, using already available tools. Mean tumor dose has been ascribed to a total of 17 tumors in 6 patients and inter and intra-patient variability of dose have been observed.

A method to generate dose rate maps has been developed and such maps have been created for tumors included in this work. From these dose rate maps, cumulative dose rate histograms have been made, and $\dot{D}_{90}$, $\dot{D}_{70}$ an $\dot{D}_{50}$-values have been calculated.

Bibliography

Cot A, J Sempau, D Pareto, S Bullich, J Pavia, and F Calvino. Evaluation of the geometric, scatter, and septal penetration components in fan-beam collimators using monte carlo simulation. *IEE Trans Nucl Sci*, 49:12–16, 2002.

Dale L. Bailey and Kathy P. Willowson. An evidence-based review of quantitative spect imaging and potential clinical applications. *Journal of Nuclear Medicine*, 54(1):83–89, 2013. doi: 10.2967/jnumed.112.111476. URL `http://jnm.snmjournals.org/content/54/1/83.abstract`.

Christoph Barchausen and Konstantin Zhernosekov. Production of n.c.a. 177lu at frm ii for radiopharmaceutical applications. `http://www.rcm.tum.de/index.php?id=54&L=1`. Accessed: 2015-5-5.

Richard Baum. *Therapeutic Nuclear Medicine*. Springer-Verlag, 2014.

Jean-Mathieu Beauregard, Michael S Hofman, Jucilene M Pereira, Peter Eu, and Rodney J Hicks. Quantitative (177)lu spect (qspect) imaging using a commercially available spect/ct system. *Cancer Imaging*, 11(1):56–66, 2011.

TM Behr, RM Sharkey, MI Juweid, Z Dunn, RM an Ying, CH Zhang, JA Siegel, DV Gold, and DM Goldenberg. Factors influencing the pharmacokinetics, dosimetry, and diagnostic accuracy of radioimmunodetection and radioimmunotherapy of carcinoembryonic antigen-expressing tumors. *Cancer Research*, 56:1805–1816, 1996.

Wesley E. Bolch, Lionel G. Bouchet, James S. Robertson, Barry W. Wessels, Jeffry A. Siegel, Roger W. Howell, Alev K. Erdi, Bulent Aydogan, Sylvain Costes, Evelyn E. Watson, J.S. Robertson (Task Group Leader) W.E. Bolch A.B. Brill N.D. Charkes D.R. Fisher M.T. Hays R.W. Howell J.A. Siegel S.R. Thomas In collaboration with the MIRD Committee, Society of Nuclear Medicine: E.E. Watson (Chair), and B.W. Wessels. Mird pamphlet no. 17: The dosimetry of nonuniform activity distributions—radionuclide s values at the voxel level. *Journal of Nuclear Medicine*, 40(1): 11S–36S, 1999. URL `http://jnm.snmjournals.org/content/40/1/11S.short`.

Wesley E. Bolch, Keith F. Eckerman, George Sgouros, and Stephen R. Thomas. Mird pamphlet no. 21: A generalized schema for radiopharmaceutical dosimetry—standardization of nomenclature. *Journal of Nuclear Medicine*, 50(3):477–484, 2009. doi: 10.2967/jnumed.108.056036. URL `http://jnm.snmjournals.org/content/50/3/477.abstract`.

SE Buckley, FH Saran, MN Gaze, S Chittenden, M Partridge, D Lancaster, Andrew Pearson, and GD Flux. Dosimetry for fractionated 131i-mibg therapies in patients with primary resistant high-risk neuroblastoma: Preliminary results. *Cancer biotherapy and Radiopharmaceuticals*, 22(1), 2007.

JF Chatal and CO Hoefnagel. Radionuclide therapy. 354:931–935, 1999.

GJR Cook, MN Maisey, KE Britton, and V Chengazi. *Clinical Nuclear Medicine*. CTC Press, 4. edition, 2006.

Marion de Jong, Wout A.P. Breeman, Roelf Valkema, Bert F. Bernard, and Eric P. Krenning. Combination radionuclide therapy using 177lu- and 90y-labeled somatostatin

analogs. *Journal of Nuclear Medicine*, 46(1 suppl):13S–17S, 2005. URL http://jnm.snmjournals.org/content/46/1_suppl/13S.abstract.

Robin de Nijs, Vera Lagerburg, Thomas L Klausen, and Søren Holm. Improving quantitative dosimetry in (177)lu-dotatate spect by energy window-based scatter. *Nuclear Medicine Communications*, 35(5):522–533, 2014.

Diane A. DeNardo, Gerald L. DeNardo, Aina Yuan, Sui Shen, Sally J. DeNardo, Daniel J. Macey, Kathleen R. Lamborn, Marc Mahe, Mark W. Groch, and William D. Erwin. Prediction of radiation doses from therapy using tracer studies with iodine-131-labeled antibodies. *Journal of Nuclear Medicine*, 37(12):1970–1975, 1996. URL http://jnm.snmjournals.org/content/37/12/1970.short.

Y Dewaraja, SJ Wildermann, KF Koral, MS Kaminski, and AM Avram. Use of integrated spect/ct imaging for tumor dosimetry in i(131) radioimmunotherapy: A pilot patient study. *Cancer biotherapy and radiopharmaceuticals*, 24(4):417–426, 2009. URL http://deepblue.lib.umich.edu/bitstream/handle/2027.42/78152/cbr.2008.0568.pdf?sequence=1&isAllowed=y.

YK Dewaraja, KF Koral, and JA Fessler. Regularized reconstruction in quantitative spect using ct side information by hybrid imaging. *Phys med biol*, 55:2523:2539, 2010a.

Yuni Dewaraja, Matthew Schipper, Peter Roberson, Scott Wilderman, Denise Regan, Hanan Amro, Kenneth Koral, Mark Kaminski, and Anca Avram. Tumor dose-response in i-131 radioimmunotherapy using measures from 3-dimensional calculation including radiobiologic modeling. *Journal of Nuclear Medicine*, 51(supplement 2):304, 2010b. URL http://jnm.snmjournals.org/content/51/supplement_2/304.abstract.

Yuni K. Dewaraja, Matthew J. Schipper, Peter L. Roberson, Scott J. Wilderman, Hanan Amro, Denise D. Regan, Kenneth F. Koral, Mark S. Kaminski, and Anca M. Avram. 131i-tositumomab radioimmunotherapy: Initial tumor dose–response results using 3-dimensional dosimetry including radiobiologic modeling. *Journal of Nuclear Medicine*, 51(7):1155–1162, 2010c. doi: 10.2967/jnumed.110.075176. URL http://jnm.snmjournals.org/content/51/7/1155.abstract.

Yuni K. Dewaraja, Eric C. Frey, George Sgouros, A. Bertrand Brill, Peter Roberson, Pat B. Zanzonico, and Michael Ljungberg. Mird pamphlet no. 23: Quantitative spect for patient-specific 3-dimensional dosimetry in internal radionuclide therapy. *Journal of Nuclear Medicine*, 53(8):1310–1325, 2012. doi: 10.2967/jnumed.111.100123. URL http://jnm.snmjournals.org/content/53/8/1310.abstract.

Yuni K. Dewaraja, Matthew J. Schipper, Jincheng Shen, Lauren B. Smith, Jure Murgic, Hatice Savas, Ehab Youssef, Denise Regan, Scott J. Wilderman, Peter L. Roberson, Mark S. Kaminski, and Anca M. Avram. Tumor-absorbed dose predicts progression-free survival following 131i-tositumomab radioimmunotherapy. *Journal of Nuclear Medicine*, 55(7):1047–1053, 2014b. doi: 10.2967/jnumed.113.136044. URL http://jnm.snmjournals.org/content/55/7/1047.abstract.

Yuni K. Dewaraja, Matthew J. Schipper, Jincheng Shen, Lauren B. Smith, Jure Murgic, Hatice Savas, Ehab Youssef, Denise Regan, Scott J. Wilderman, Peter L. Roberson, Mark S. Kaminski, and Anca M. Avram. Tumor-absorbed dose predicts progression-free survival following 131i-tositumomab radioimmunotherapy. *Journal of Nuclear*

Medicine, 55(7):1047–1053, 2014a. doi: 10.2967/jnumed.113.136044. URL http://jnm.snmjournals.org/content/55/7/1047.abstract.

Y Du, EC Frey, WT Wang, C Tocharoenchai, WH Baird, and BMW Tsui. Combination of mcnp and simset for monte carlo simulation of spect with medium- and high-energy photons. *IEE Trans Nucl Sci*, 49:668–674, 2002.

K Erlandson, I Buvat, PH Pretorius, BA Thomas, and BF Hutton. A review of partial volume correction techniques for emission tomography and their applications in neurology, cardiology and oncology. *Physics in Medicine and Biology*, 57:119–159, 2012.

Enrico Fermi. Radiactivity induced by neutron bombardement. *Nature*, page 751, 1934.

María Fernández, Heribert Hänscheid, Thibault Mauxion, Manuel Bardiès, Peter Kletting, Gerhard Glatting, and Michael Lassmann. A fast method for rescaling voxel s values for arbitrary voxel sizes in targeted radionuclide therapy from a single monte carlo calculation. *Medical Physics*, 40(8):–, 2013. doi: http://dx.doi.org/10.1118/1.4812684. URL http://scitation.aip.org/content/aapm/journal/medphys/40/8/10.1118/1.4812684.

MA Flower. *Webbs physics of medical imaging*. Taylor & Francis group, second edition edition, 2012.

G Flux, M Bardies, Myriam Monsieurs, S Savolainen, SE Strand, and M Lassmann. The impact of pet and spect on dosimetry for targeted radionuclide therapy. 16:47–59, 2006.

Leonard M Freeman and M. Donald Blaufox. Letter from the editors: Theranostics. *Seminars in nuclear medicine*, 42(3), 2012.

Ernest V. Garcia, Tracy L. Faber, and Fabio P. Esteves. Cardiac dedicated ultrafast spect cameras: New designs and clinical implications. *Journal of Nuclear Medicine*, 52 (2):210–217, 2011. doi: 10.2967/jnumed.110.081323. URL http://jnm.snmjournals.org/content/52/2/210.abstract.

Joshua Grimes and Anna Celler. Comparison of internal dose estimates obtained using organ-level, voxel s value, and monte carlo techniques. *Medical Physics*, 41(9):092501, 2014. doi: http://dx.doi.org/10.1118/1.4892606. URL http://scitation.aip.org/content/aapm/journal/medphys/41/9/10.1118/1.4892606.

B He, Y Du, X Song, WB Segars, and EC Frey. A monte carlo and physical phantom evaluation of quantitative in(111) spect. *Phys med biol*, 50:4169:4185, 2005.

EJ Hoffmann, SC Huang, and ME Phelps. Quantification in positron emission computed tomography: 1. effect of object size. *Journal of computer assisted Tomography*, 3:299–308, 1979.

H Holte and A Fossa. Oncolex. http://www.oncolex.org/Lymphoma/Diagnoses/Non-Hodgkin-lymphoma. Accessed: 2015-21-5.

Sandra J. Horning, Anas Younes, Vinay Jain, Stewart Kroll, Jennifer Lucas, Donald Podoloff, and Michael Goris. Efficacy and safety of tositumomab and iodine-131 tositumomab (bexxar) in b-cell lymphoma, progressive after rituximab. *Journal of Clinical Oncology*, 23(4):712–719, 2005. doi: 10.1200/JCO.2005.07.040. URL http://jco.ascopubs.org/content/23/4/712.abstract.

DM Howard, KJ Kearfott, SJ Wildermann, and YK Dewaraja. Comparison of i-131 radioimmunotherapy tumor dosimetry: Unit sphere density sphere model versus patient-specific monte carlo calculations. *Cancer Biotherapy and radiopharmaceuticals*, 26(5): 615–621, 2011.

Ezgi Ilan, Mattias Sandström, Cecilia Wassberg, Anders Sundin, Ulrike Garske–Román, Barbro Eriksson, Dan Granberg, and Mark Lubberink. Dose response of pancreatic neuroendocrine tumors treated with peptide receptor radionuclide therapy using 177lu-dotatate. *Journal of Nuclear Medicine*, 56(2):177–182, 2015. doi: 10.2967/jnumed.114.148437. URL `http://jnm.snmjournals.org/content/56/2/177.abstract`.

Price A. Jackson, Jean-Mathieu Beauregard, Michael S. Hofman, Tomas Kron, Annette Hogg, and Rodney J. Hicks. An automated voxelized dosimetry tool for radionuclide therapy based on serial quantitative spect/ct imaging. *Medical Physics*, 40(11):12503, 2013. doi: http://dx.doi.org/10.1118/1.4824318. URL `http://scitation.aip.org/content/aapm/journal/medphys/40/11/10.1118/1.4824318`.

Ronald Jaszczak. The early years of single photon emission computed tomography(spect):an anthalogy of selected reminiscences. *Physics in medicine and biology*, 51:99–115, 2006.

Currie Joliot. Artificial production of a new kind of radio-element. *Nature*, page 201, 1934.

Katherine S. Kolbert, Keith S. Pentlow, Joel R. Pearson, Arif Sheikh, Ronald D. Finn, John L. Humm, and Steven M. Larson. Prediction of absorbed dose to normal organs in thyroid cancer patients treated with 131i by use of 124i pet and 3-dimensional internal dosimetry software. *Journal of Nuclear Medicine*, 48(1):143–149, 2007. URL `http://jnm.snmjournals.org/content/48/1/143.abstract`.

F. G. Kondex. Nuclear data sheets 98. 2003. URL `http://www.nndc.bnl.gov/chart/decaysearchdirect.jsp?nuc=177LU&unc=nds`.

Kenneth F. Koral, Yuni Dewaraja, Jia Li, Carla L. Barrett, Denise D. Regan, Kenneth R. Zasadny, Stephen G. Rommelfanger, Issac R. Francis, Mark S. Kaminski, and Richard L. Wahl. Initial results for hybrid spect-conjugate-view tumor dosimetry in 131i-anti-b1 antibody therapy of previously untreated patients with lymphoma. *Journal of Nuclear Medicine*, 41(9):1579–1586, 2000. URL `http://jnm.snmjournals.org/content/41/9/1579.short`.

Kenneth F. Koral, Yuni Dewaraja, Jia Li, Qiang Lin, Denise D. Regan, Kenneth R. Zasadny, Stephen G. Rommelfanger, Issac R. Francis, Mark S. Kaminski, and Richard L. Wahl. Update on hybrid conjugate-view spect tumor dosimetry and response in 131i-tositumomab therapy of previously untreated lymphoma patients. *Journal of Nuclear Medicine*, 44(3):457–464, 2003. URL `http://jnm.snmjournals.org/content/44/3/457.abstract`.

N Lanconnelli, M Pacilio, S Lo Meo, F Botta, A Di Dia, LA Torres Aroche, MA Coca Perez, and M Cremonesi. A free database of radionuclide voxel s values for the dosimetry of nonuniform activity distributions. *Physics in medicine and Biology*, 57:517–533, 2012.

R Loevinger, TF Buddinger, and EE Watson. *MIRD Primer for absorbed dose calculations*. 1988.

JT Lyman. Complication probability as assessed from dose-volume histograms. *Radiation research*, 104, 1985.

D Minarik, K Sjøgreen-Gleisner, and M Ljungberg. Evaluation of quantitative ^{90}y spect based on experimental phantom studies. *Phys med biol*, 53:5689:5703, 2008.

NIDC. National isotope development center home page.

Tove Olafsen and Anna M. Wu. Antibody vectors for imaging. *Seminars in Nuclear Medicine*, 40(3):167 – 181, 2010. ISSN 0001-2998. doi: http://dx.doi.org/10.1053/j.semnuclmed.2009.12.005. URL `http://www.sciencedirect.com/science/article/pii/S0001299809001184`. Antibodies and Peptides in Nuclear Medicine Imaging and Therapy.

O W Press, J F Eary, C C Badger, P J Martin, F R Appelbaum, R Levy, R Miller, S Brown, W B Nelp, and K A Krohn. Treatment of refractory non-hodgkin's lymphoma with radiolabeled mb-1 (anti-cd37) antibody. *Journal of Clinical Oncology*, 7(8):1027–38, 1989. URL `http://jco.ascopubs.org/content/7/8/1027.abstract`.

William Pretwich, Josane Nunes, and Cheuk Kwok. *Journal of nuclear medicine*, 30: 1036–1046, 1989.

Arman Rahmin and Habib Zaidi. Pet versus spect:strengths, limitations and challenges. *Nuclear Medicine Communications*, 29(1):193–207, 2008.

A Repetto-Llamazares, A NASIR, ØS. Bruland, J Dahle, and RH. Larsen. Advantage of lutetium-177 versus radioiodine immunoconjugate in targeted radionuclide therapy of b-cell tumors. *Anticancer Research*, 34(7):3263–3269, 2014a. URL `http://ar.iiarjournals.org/content/34/7/3263.abstract`.

AHV Repetto-Llamazares, RH Larsen, AM Giusti, E Riccardi, and ØS Bruland. 177lu-dota-hh1, a novel anti-cd37 radioimmunoconjugate:a study of toxicity in nude mice. *PLoS one*, 9(7), 2014b.

P Ritt, H Vija, J Hornegger, and T Kuwert. Absolute quantification in spect. *European Journal of Nuclear Medicine and Molecular Imaging*, 38:S69–S77, 2011.

M Sandstrom. *Dosimetry of Radionuclide Therapy with ^{177}Lu-octreotate*. PhD thesis, Uppsala, 2011. URL `http://www.diva-portal.org/smash/get/diva2:443143/FULLTEXT01.pdf`.

M Sandstrom, U Garske, and Dan Granberg. Individualized dosimetry in patients undergoing therapy with 177lu-dota-d-phe1-tyr3-octreotate. *Journal of European Med. Mol. Imaging*, 37, 2010.

MJ Schipper, KF Koral, AM Avram, MS Kaminski, and YK Dewaraja. Prediction of therapy tumor-absorbed dose estimates in i-131 radioimmunotherapy using tracer data via a mixed-model fit to time activity. *Cancer Biotherapy & Radiopharmaceuticals*, 27 (7):403–411, 2012. doi: doi:10.1089/cbr.2011.1053.

Ulrich Schötzig, Heinrich Schrader, Eckart Schönfeld, Eberhard Günther, and Reiner Klein. Standardisation and decay data of 177lu and 188re. *Applied Radiation and Isotopes*, 55(1):89 – 96, 2001. ISSN 0969-8043. doi: http://dx.doi.org/10.1016/

S0969-8043(00)00362-6. URL http://www.sciencedirect.com/science/article/pii/S0969804300003626.

George Sgouros. Dosimetry of internal emitters. *Journal of Nuclear Medicine*, 46 (1 suppl):18S–27S, 2005. URL http://jnm.snmjournals.org/content/46/1_suppl/18S.abstract.

George Sgouros, Shannon Squeri, Åse M. Ballangrud, Katherine S. Kolbert, Jerrold B. Teitcher, Katherine S. Panageas, Ronald D. Finn, Chaitanya R. Divgi, Steven M. Larson, and Andrew D. Zelenetz. Patient-specific, 3-dimensional dosimetry in non-hodgkin's lymphoma patients treated with 131i-anti-b1 antibody: Assessment of tumor dose-response. *Journal of Nuclear Medicine*, 44(2):260–268, 2003. URL http://jnm.snmjournals.org/content/44/2/260.abstract.

George Sgouros, Katherine S. Kolbert, Arif Sheikh, Keith S. Pentlow, Edward F. Mun, Axel Barth, Richard J. Robbins, and Steven M. Larson. Patient-specific dosimetry for 131i thyroid cancer therapy using 124i pet and 3-dimensional-internal dosimetry (3d-id) software. *Journal of Nuclear Medicine*, 45(8):1366–1372, 2004. URL http://jnm.snmjournals.org/content/45/8/1366.abstract.

S Shcherbinin, A Celler, T Belhocine, R Vanderwerf, and A Driedger. Accuracy of quantitative reconstructions in spect/ct imaging. *Phys med biol*, 53:4595:4604, 2008.

S Shcherbinin, H Piwowarska-Bilska, A Celler, and B Birkenfeld. Quantitative spect/ct reconstruction for 177 lu and 177 lu/ 90 y targeted radionuclide therapies. *Physics in Medicine and Biology*, 57(18):5733, 2012. URL http://stacks.iop.org/0031-9155/57/i=18/a=5733.

Jeffry A. Siegel, Stephen R. Thomas, James B. Stubbs, Michael G. Stabin, Marguerite T. Hays, Kenneth F. Koral, James S. Robertson, Roger W. Howell, Barry W. Wessels, Darrell R. Fisher, David A. Weber, and A. Bertrand Brill. Mird pamphlet no. 16: Techniques for quantitative radiopharmaceutical biodistribution data acquisition and analysis for use in human radiation dose estimates. *Journal of Nuclear Medicine*, 40(2): 37S–61S, 1999. URL http://jnm.snmjournals.org/content/40/2/37S.short.

A Skretting. Intensity diffusion is a better description than partial volume effect. *European Journal of Nuclear Medicine and Molecular Imaging*, 36:536–537, 2009.

E Smeland, E Funderud, Sand, H Kiil, and T Godal. Characterization of two murine monoclonal antibodies reactive with human b cells. their use in a high-yield, high-purity method for isolation of b cells and utilization of such cells in an assay for b-cell stimulating factor. *Scandinavian Journal of Immunology*, 21(3):205–214, 1985.

Annti Sohlberg, Hiroshi Watabe, Miho Shidahara, and Hidehiro Iida. Body-contour versus circular orbit acquisition in cardiac spect:assessment of defect detectability with channelized hotelling observer. *Nuclear Medicine Communications*, 28(12):937–942, 2007.

Hong Song, Yong Du, George Sgouros, Andrew Prideaux, Eric Frey, and Richard L. Wahl. Therapeutic potential of 90y- and 131i-labeled anti-cd20 monoclonal antibody in treating non-hodgkin's lymphoma with pulmonary involvement: A monte carlo–based dosimetric analysis. *Journal of Nuclear Medicine*, 48(1):150–157, 2007. URL http://jnm.snmjournals.org/content/48/1/150.abstract.

LV Spencer. Theory of electron penetration. *Phys rev*, 98:1597–1615, 1955.

Michael G. Stabin and Mark W. Konijnenberg. Re-evaluation of absorbed fractions for photons and electrons in spheres of various sizes. *Journal of Nuclear Medicine*, 41(1): 149–160, 2000. URL http://jnm.snmjournals.org/content/41/1/149.short.

Michael G. Stabin, Richard B. Sparks, and Eric Crowe. Olinda/exm: The second-generation personal computer software for internal dose assessment in nuclear medicine. *Journal of Nuclear Medicine*, 46(6):1023–1027, 2005. URL http://jnm.snmjournals.org/content/46/6/1023.abstract.

Boon-Keng Teo, Youngho Seo, Stephen L. Bacharach, Jorge A. Carrasquillo, Steven K. Libutti, Himanshu Shukla, Bruce H. Hasegawa, Randall A. Hawkins, and Benjamin L. Franc. Partial-volume correction in pet: Validation of an iterative postreconstruction method with phantom and patient data. *Journal of Nuclear Medicine*, 48(5):802–810, 2007. doi: 10.2967/jnumed.106.035576. URL http://jnm.snmjournals.org/content/48/5/802.abstract.

K Willowson, DL Bailey, EA Bailey, C Baldock, and PJ Roach. In vivo validation of quantitative spect in the heart. *Clinical physiology and functional imaging*, 30(3), 2010.

Gregory A. Wiseman, Christine A. White, Thomas E. Witzig, Leo I. Gordon, Christos Emmanouilides, Andrew Raubitschek, Nalini Janakiraman, John Gutheil, Russell J. Schilder, Stewart Spies, Daniel H. S. Silverman, and Antonio J. Grillo-López. Radioimmunotherapy of relapsed non-hodgkin's lymphoma with zevalin, a 90y-labeled anti-cd20 monoclonal antibody. *Clinical Cancer Research*, 5(10):3281s–3286s, 1999. URL http://clincancerres.aacrjournals.org/content/5/10/3281s.abstract.

Johannes Zeintl, Alexander Hans Vija, Amos Yahil, Joachim Hornegger, and Torsten Kuwert. Quantitative accuracy of clinical 99mtc spect/ct using ordered-subset expectation maximization with 3-dimensional resolution recovery, attenuation, and scatter correction. *Journal of Nuclear Medicine*, 51(6):921–928, 2010. doi: 10.2967/jnumed.109.071571. URL http://jnm.snmjournals.org/content/51/6/921.abstract.

List of Figures

List of Tables

Appendix A

Dose rate maps from day 4

Maps of dose rate and cumulative volume histograms. Some are in true color, some in grayscale.

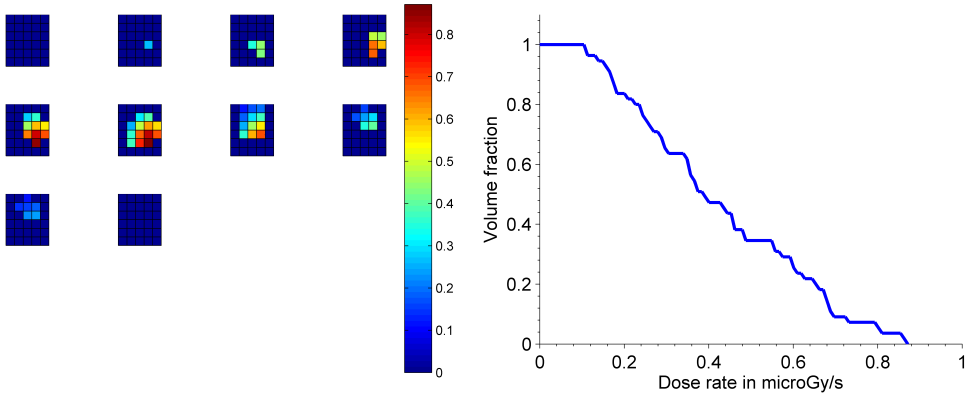

(a) **(b)**

Figure A.1: Patient 2 Lower R. neck

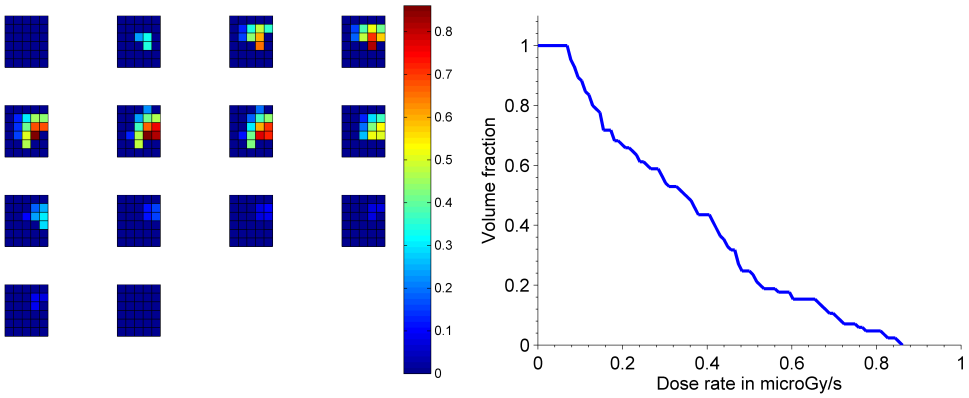

(a) **(b)**

Figure A.2: Patient 2 Upper R. neck

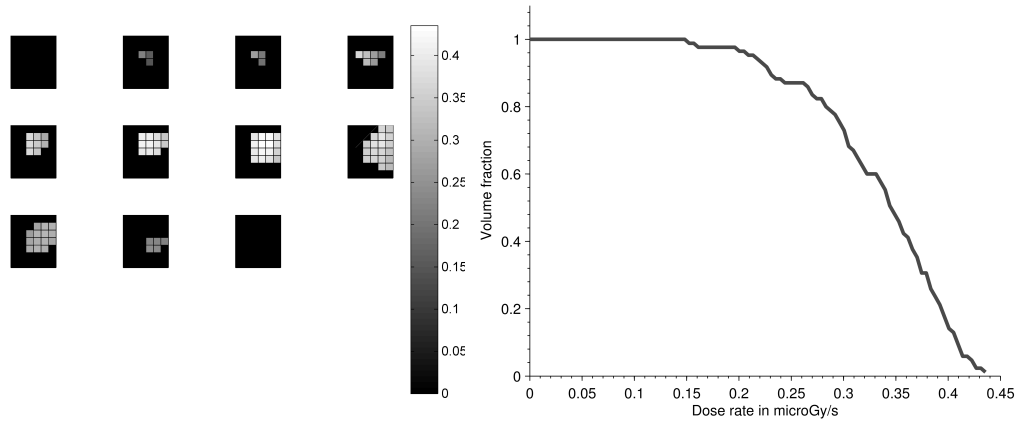

(a) **(b)**

Figure A.3: Patient 2 Para-esophageal

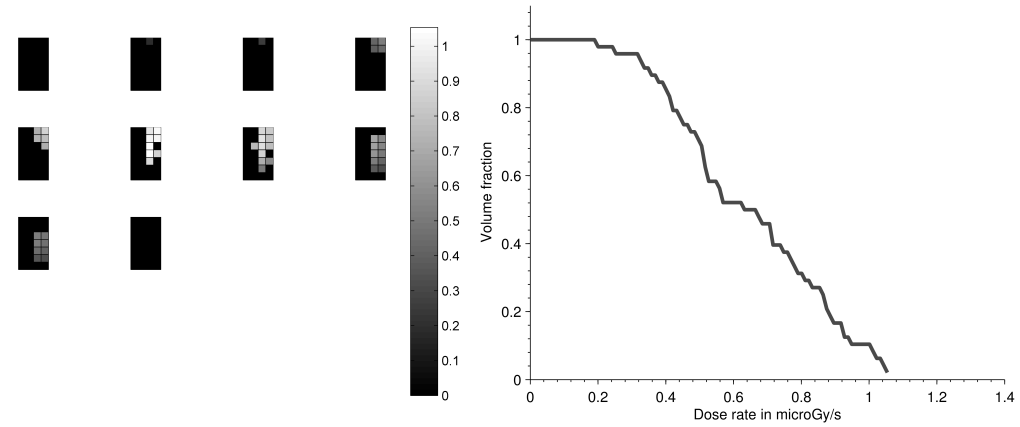

(a) **(b)**

Figure A.4: Patient 3 Para-tracheal R.

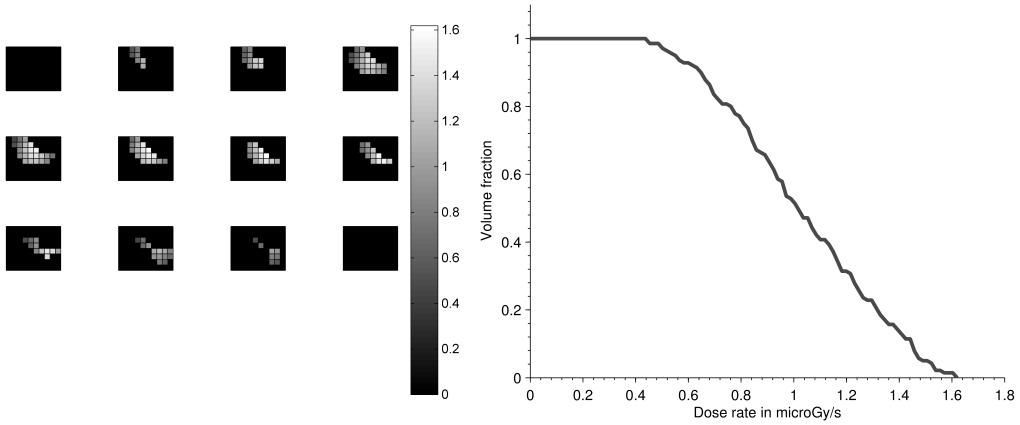

(a) **(b)**

Figure A.5: Patient 3 Para-vertebral R.

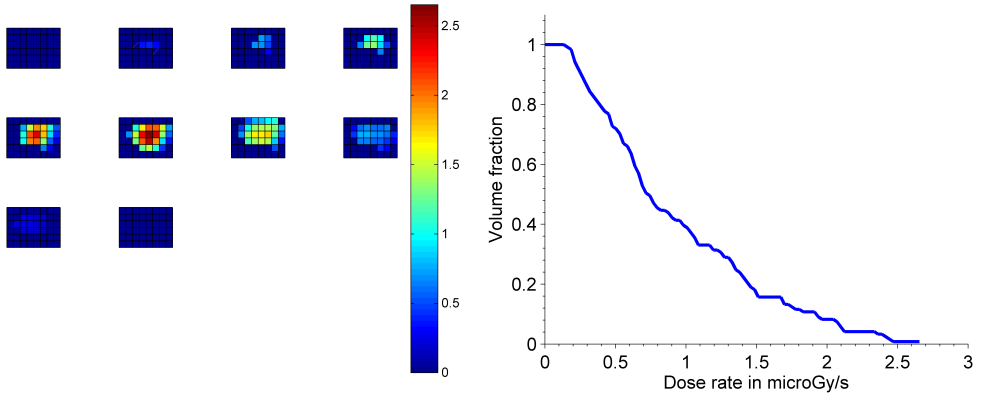

(a) (b)

Figure A.6: Patient 5 Inguinal R.

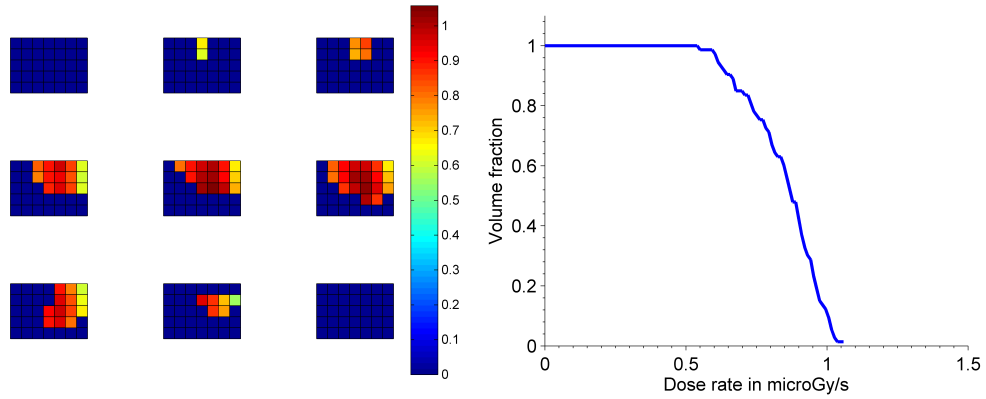

(a) (b)

Figure A.7: Patient 5 Retroperitoneum

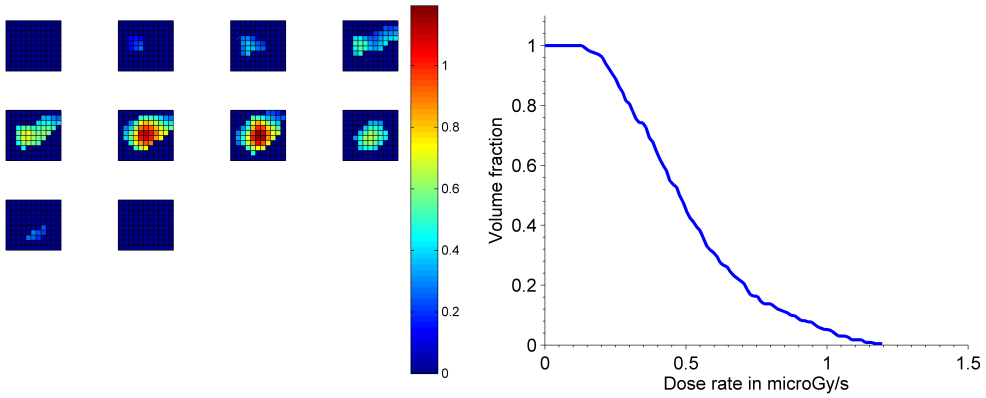

(a) (b)

Figure A.8: Patient 5 Subcut Nates R.

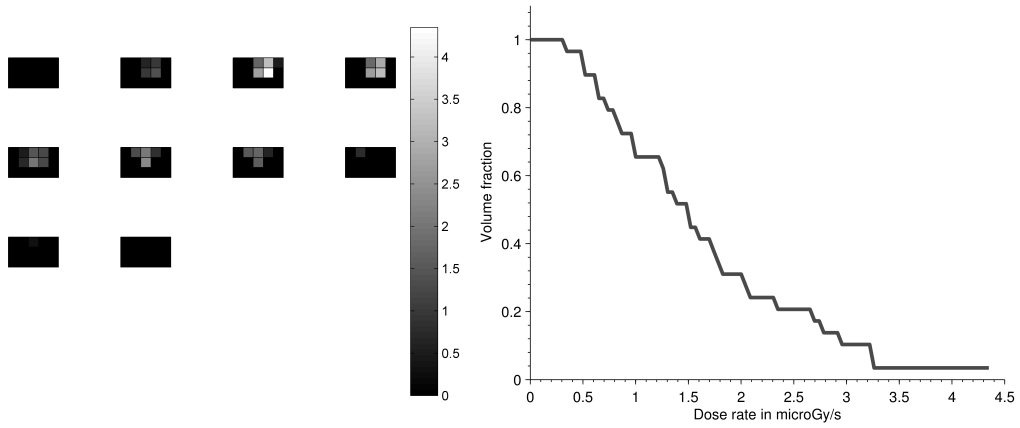

(a) **(b)**

Figure A.9: Patient 7 Inguinal R.

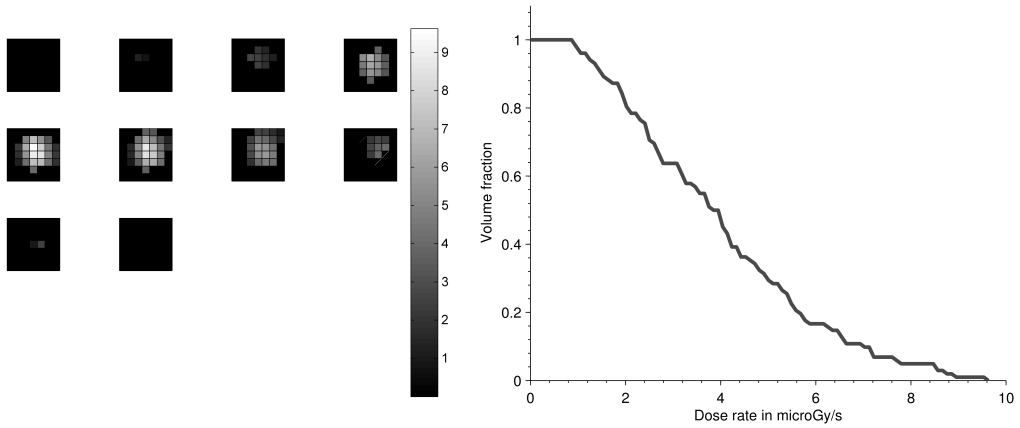

(a) **(b)**

Figure A.10: Patient 7 Lower L. Inguinal

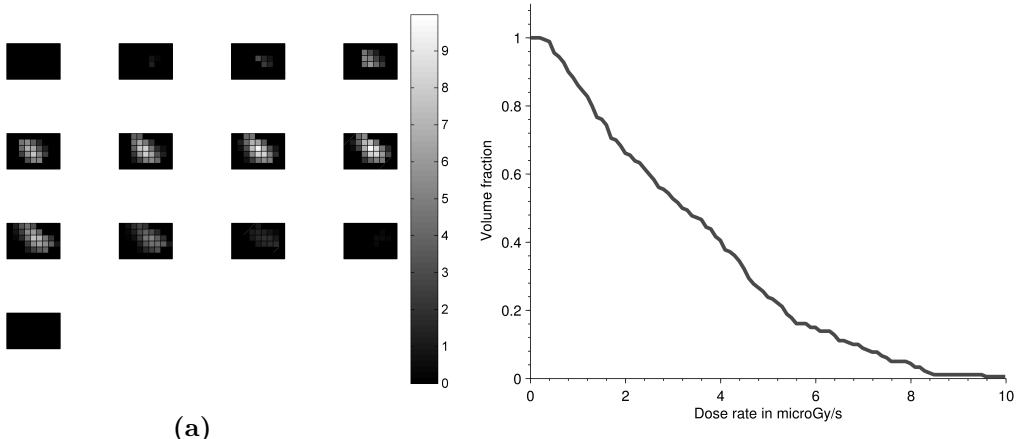

(a) **(b)**

Figure A.11: Patient 7 Upper L. Inguinal

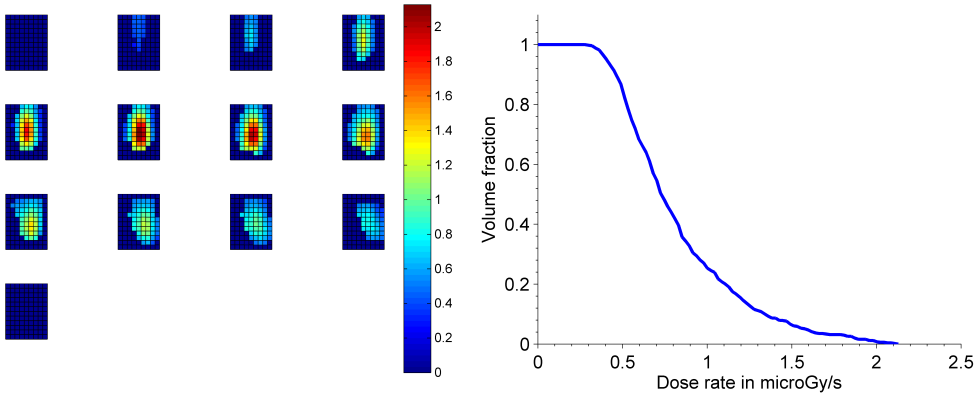

(a) (b)

Figure A.12: Patient 9 Mediastinum Anterior

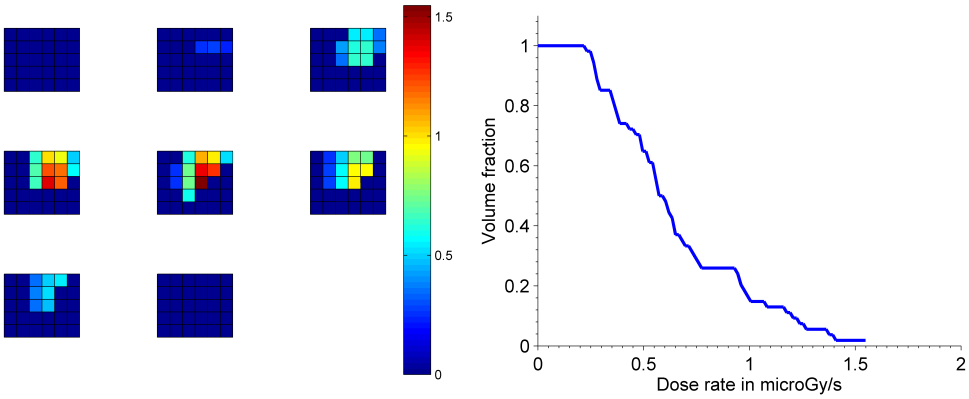

(a) (b)

Figure A.13: Patient 9 Inguinal R.

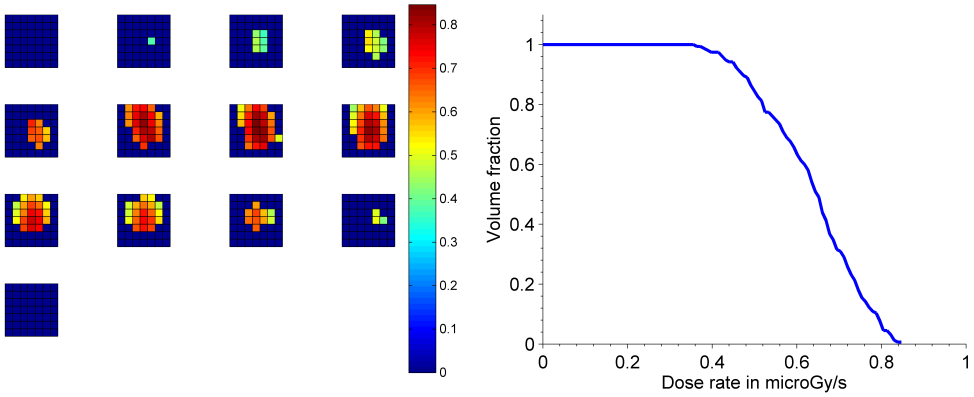

(a) (b)

Figure A.14: Patient 9 Mediastinum Upper.

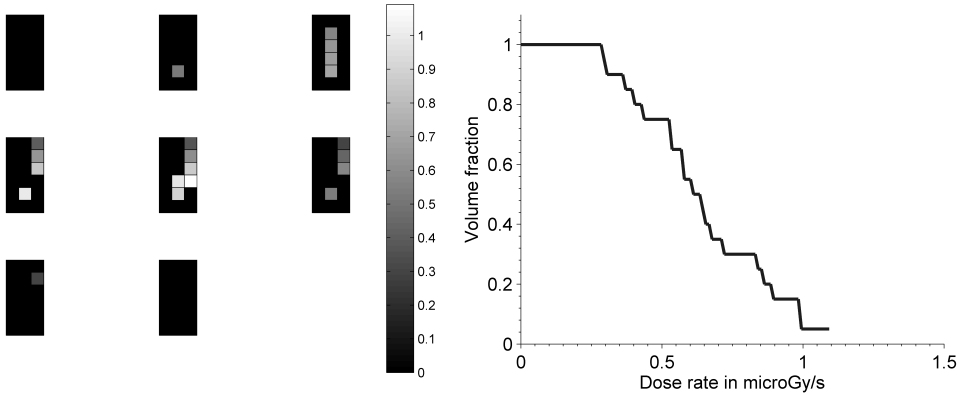

(a) **(b)**

Figure A.15: Patient 11 Axilla.

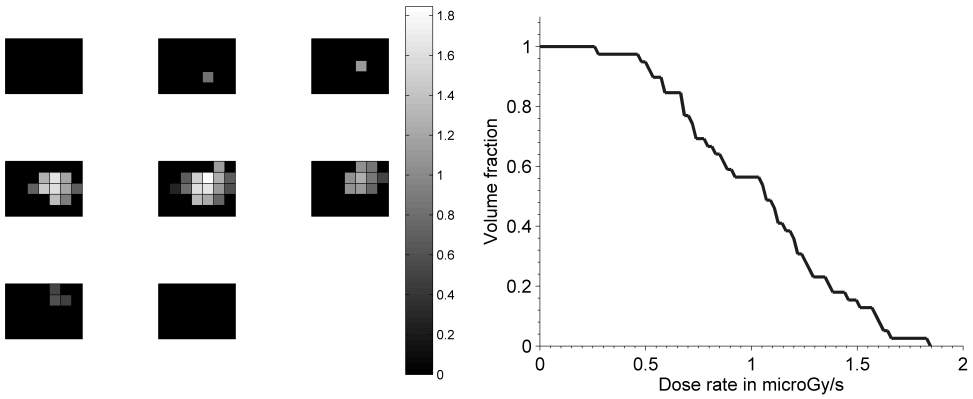

(a) **(b)**

Figure A.16: Patient 11 Upper neck.

Appendix B

Additional $\bar{S}$-factors

Table B.1: Additional $\bar{S}$-values for spheres smaller and larger than the tumors used in this work.

Tumor mass (g)	$\bar{S}$ J/MBqHrs
0.01	$7.85 \cdot 10^{-5}$
0.1	$8.17 \cdot 10^{-5}$
0.5	$8.3 \cdot 10^{-5}$
400	$8.72 \cdot 10^{-5}$
500	$8.75 \cdot 10^{-5}$
600	$8.76 \cdot 10^{-5}$
1000	$8.82 \cdot 10^{-5}$
2000	$8.92 \cdot 10^{-5}$
3000	$8.97 \cdot 10^{-5}$
4000	$9.04 \cdot 10^{-5}$
5000	$9.05 \cdot 10^{-5}$
6000	$9.12 \cdot 10^{-5}$

Appendix C

PSF correction shape plots and activity loss

Figure C.1 show the amount of count measured with VOI_{CT} after a deconvolution. Included in the figure is also the baseline, indicating no correction.

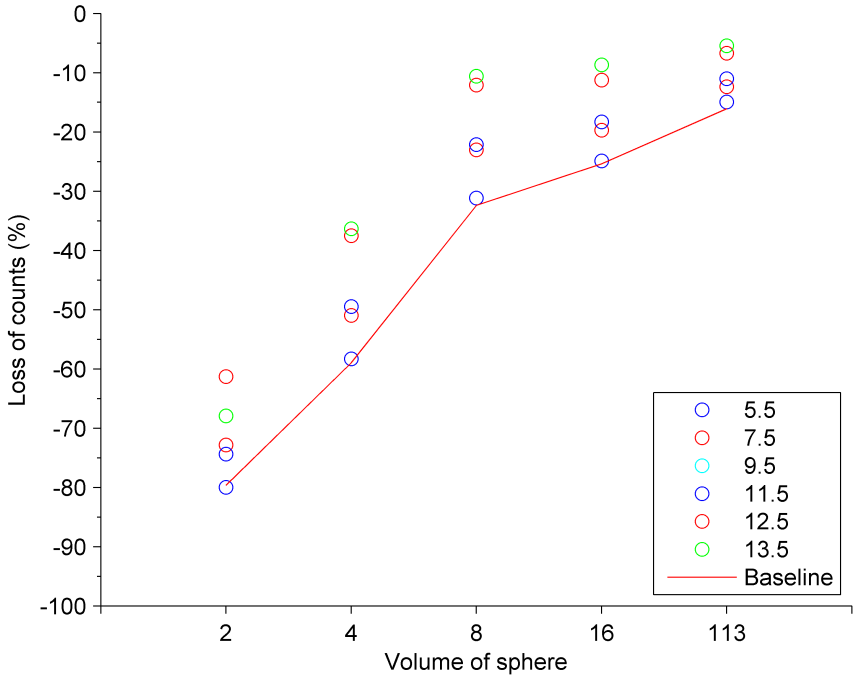

Figure C.1: The resulting loss after a deconvolution of the activity distribution and extraction from a CT-guided VOI. Baseline indicate the loss of activity with no PSF-correction. A range of FWHM-values have been used.

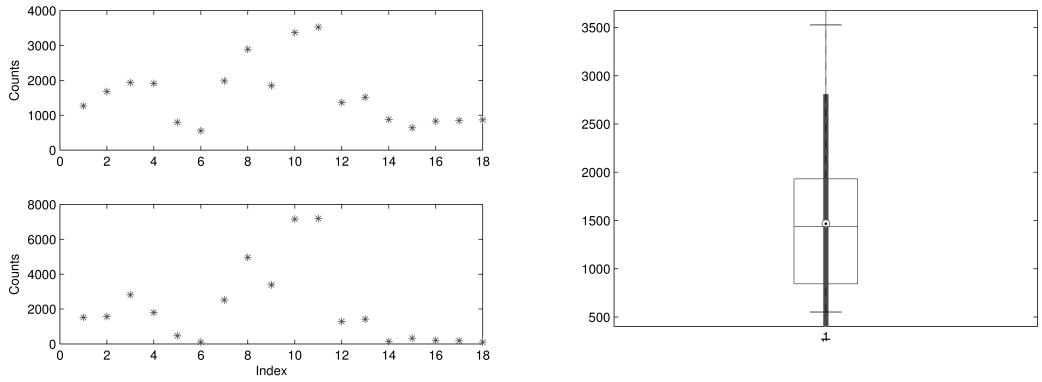

(a) **(b)**

Figure C.2: Count values for the voxels of the 2mL sphere after a point spread correction. Upper left shows counts before the correction, lower left after. In the boxplot to the right, horizontal lines indicate STD-range and mean before the correction, thick lines and circle indicates STD and mean post correction.

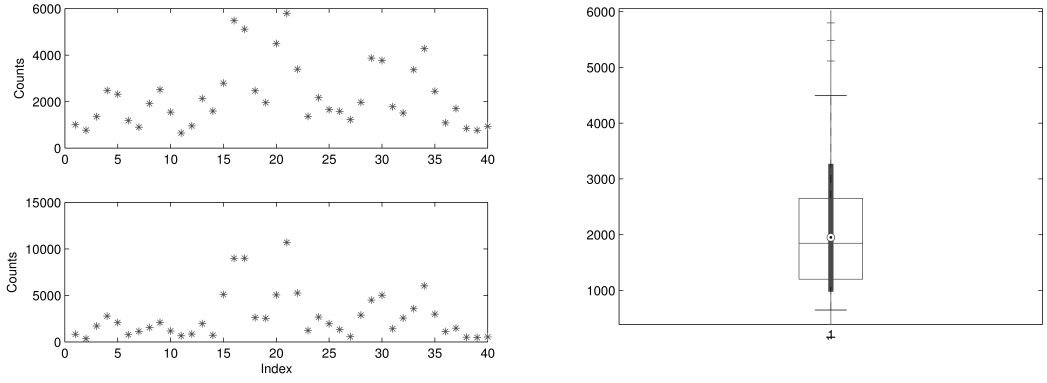

(a) **(b)**

Figure C.3: Count values for the voxels of the 4mL sphere after a point spread correction. Identical scheme as in figure C.2

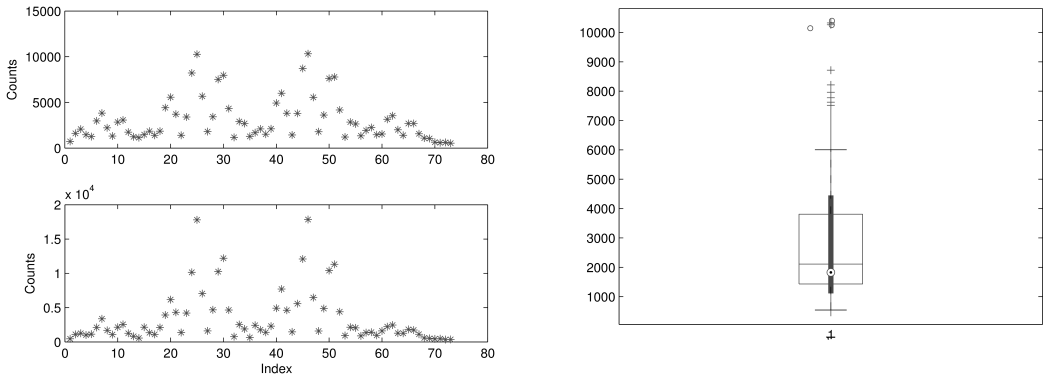

(a) **(b)**

Figure C.4: Count values for the voxels of the 8mL sphere after a point spread correction. Identical scheme as in figure C.2

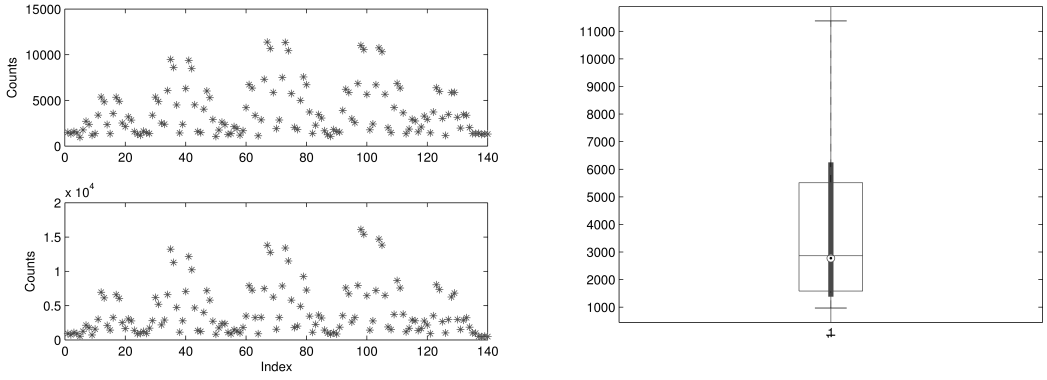

(a) **(b)**

Figure C.5: Count values for the voxels of the 16mL sphere after a point spread correction. Identical scheme as in figure C.2

Appendix D

Source code listings

This part of the appendix consists of a few of the small programs written over the course of this work.

```
% Script to do visualization of dose rate maps calculated from activity
% distributions with the help of Voxel-S-values and data taken from
% atteunuation corrected SPECT-images
%
% Name  : dose_rate_map
% Author: Johan Blakkisrud blakkisr@stud.ntnu.no
%

clear all;
close all; % Make sure work space is empty


%%=========================================================================
%%
%% String that contains the data.
%%
%%=========================================================================


ima_files = [...
    'data/ima_data/pas2dag4.ima'; ...  %1
    'data/ima_data/pas2dag7.ima'; ...  %2
    'data/ima_data/pas3dag4.ima'; ...  %3
    'data/ima_data/pas3dag7.ima'; ...  %4
    'data/ima_data/pas5dag4.ima'; ...  %5
    'data/ima_data/pas5dag7.ima'; ...  %6
    'data/ima_data/pas7dag4.ima'; ...  %7
    'data/ima_data/pas7dag7.ima' ];

voxel_coordinates_file = 'data/voxel_coordinates/main_report_data/collection_rc_volumes.xlsx';

sheat_names = [...
    'Pas2halsovreD4';...  % 1
    'Pas2halsovreD7';...  % 2
    'Pas2halsnedrD4';...  % 3
    'Pas2halsnedrD7';...  % 4
    'Pas2paraosofD4';...  % 5
    'Pas2paraosofD7';...  % 6
```

```
    'Pas3paratracD4';...  % 7
    'Pas3paratracD7';...  % 8
    'Pas3paravertD4';...  % 9
    'Pas3paravertD7';...  % 10
    'Pas5hoylyskeD4';...  % 11
    'Pas5hoylyskeD7';...  % 12
    'Pas5subcutanD4';...  % 13
    'Pas5subcutanD7';...  % 14
    'Pas5retroperD4';...  % 15
    'Pas5retroperD7';...  % 16
    'Pas7lyskeovrD4';...  % 17
    'Pas7lyskeovrD7';...  % 18
    'Pas7lyskenedD4';...  % 19
    'Pas7lyskenedD7';...  % 20
    'Pas7lyskehoyD4';...  % 21
    'Pas7lyskehoyD7';...  % 22
    ];

ima_file_nums = [1 1 1 3 3 5 5 5 7 7 7];
sheat_nums = [1 3 5 7 9 11 13 15 17 19 21];

%%=========================================================================
%%
%% Constants
%%
%%=========================================================================

ACT_CONV = 17e-6 ;% Conversion from count to MBq
LA_PHYS = -0.0043;
time_points = [4*24, 7*24];
time_point_num = 1;
S_bar = 1.6e-13*0.133*1e6 ; % From MBq to GyKg/s (or joule)

kernel_maker % Script to make voxel-s-values properly formatted

%%=========================================================================
%%
%% Input section
%%
%%=========================================================================

d_rate_XX = zeros(11,1);

for tumor_num = 1:11


    sheat_num = sheat_nums(tumor_num);
    ima_file_num = ima_file_nums(tumor_num);

    image_file_path = ima_files(ima_file_num,:);
    voi_sheat_names = sheat_names(sheat_num,:);
    voi_list_path = voxel_coordinates_file;

    %%=====================================================================
    %%
    %% End of input section
    %%
    %%=====================================================================
```

```
97
98      % Acquring maps of the activity distribution
99
100     [image_matrix map] = dicomread(image_file_path(time_point_num,:));
101
102     image_raw_stack_pre = squeeze(image_matrix(:,:,1,:));
103
104     [x_size, y_size, num_of_slices] = size(image_raw_stack_pre(:,:,:));
105
106     image_raw_stack = zeros(x_size, y_size, num_of_slices);
107     image_raw_stack(:,:,:) = image_raw_stack_pre;
108
109     clear image_raw_stack_pre;
110
111     gray_scale_stack = zeros(x_size, y_size, num_of_slices);
112
113
114     for i = 1:num_of_slices
115
116         gray_scale_stack(:,:,i) = mat2gray(image_raw_stack(:,:,i));
117
118     end
119
120     tumor_mask = zeros(x_size,y_size,num_of_slices);
121
122     %% Try to load vois directly -
123
124     num_data = xlsread(voi_list_path(1,:),voi_sheat_names(time_point_num,:));
125
126     X_index = num_data(:,2);
127     Y_index = num_data(:,1);
128     Z_index = num_data(:,3);
129     vox_vals = num_data(:,4);
130
131     for p_num = 1:length(X_index)
132
133         point = [X_index(p_num) Y_index(p_num) Z_index(p_num)];
134         point_val = vox_vals(p_num);
135         stack_val = image_raw_stack(point(1), point(2), point(3));
136
137         tumor_mask(point(1), point(2), point(3)) = 1;
138
139         if stack_val ~= point_val
140
141             disp('Error, non matching voxel-values')
142             disp('Breaking loop')
143             break
144
145         end
146
147     end
148
149     masked_stack = tumor_mask.*image_raw_stack;
150
151
152     % Convert to activity
153
154     masked_stack_act = masked_stack*ACT_CONV;
```

```
155     image_act_stack = image_raw_stack*ACT_CONV;
156
157     % Convert to dose through S-value look up-table
158
159     dose_rate_map = convn(image_act_stack, s_values, 'same')*1000; % Finished value in microGy/s
160     dose_rate_map_masked = dose_rate_map.*tumor_mask;
161
162     I_tumor = find(masked_stack_act);
163
164     %% Find a portion to illustrate distribution
165
166     [max_val I_max_val] = max(dose_rate_map_masked(:));
167
168     [I J K] = ind2sub(size(dose_rate_map_masked), I_max_val);
169
170     tumor_slice = masked_stack_act(:,:,K);
171     body_slice = image_act_stack(:,:,K);
172
173     tumor_rate_slice = dose_rate_map_masked(:,:,K);
174     body_rate_slice = dose_rate_map(:,:,K);
175
176     % Visualize the tumor in all dimensions by cutting out the relevant portion
177
178     x_min = min(X_index);
179     y_min = min(Y_index);
180     z_min = min(Z_index);
181
182     x_max = max(X_index);
183     y_max = max(Y_index);
184     z_max = max(Z_index);
185
186     tumor_selection = dose_rate_map_masked(x_min:x_max, y_min:y_max,z_min:z_max);
187     z_names = z_min-1:z_max+1;
188
189     tumor_selection_padded = padarray(tumor_selection, [1 1 1]);
190
191     [a b] = dose_vol_hist(dose_rate_map(I_tumor),100);
192
193     %% Find DXX
194
195     threshold = 0.90; % Set the threshold wanted
196     fractions_norm = b/max(b);
197     index_threshold = find(fractions_norm < threshold,1);
198     threshold_dose = a(index_threshold);
199
200     d_rate_XX(tumor_num) = threshold_dose;
201     threshold_dose
202
203
204     I_tumor_slice = find(tumor_slice);
205     body_slice(I_tumor_slice) = body_slice(I_tumor_slice)*-1;
206
207
208     figure()
209     plot_1 = plot(a,b/length(vox_vals));
210     xlabel('Dose rate in microGy/s')
211     ylabel('Volume fraction')
212     ylim([0 1.1])
```

```
213
214     set(plot_1      ,...
215         'LineStyle' , 'default',...
216         'LineWidth' , 2.5,...
217         'color'     , 'b')
218
219     set(gca, ...
220         'Box'   , 'off'     ,...
221         'TickDir'   , 'out'     ,...
222         'YMinorTick'   , 'on',...
223         'XMinorTick'   , 'on',...
224         'Ytick' ,   0:0.2:1);
225
226     set(gcf, 'PaperPositionMode', 'auto');
227     file_name = strcat('figures/',sheat_names(sheat_num,:),'final.eps')
228     %print -depsc2 file_name
229     print(file_name,'-depsc2')
230
231     disp(tumor_num)
232
233 end
```

```
1  % Script to generate a kernel for a voxel s-value calculation.
2  %
3  % Name   : kernel_maker
4  % Author : Johan Blakkisrud blakkisr@stud.ntnu.no
5  %
6  % Values for the kernel are stored in the datafile "kernel.mat"
7  % Values are stored as indices (I,J,K) = Val for indices (0,0,0)
8  % to (5,5,5) with (0,0,0) being the central voxel.
9  % As this represents an octant, the script fills up a 11 by 11 by 11
10 % matrix by utilizing symmetry.
11 %
12 % Method as of now loops over each value and place them in the up to
13 % eight possibilities they could be in the full matrix.
14 % This causes some redundancy, as not every value have eight locations
15 % Per example, (0,0,0) have only one, (6,6,6), the central voxel.
16
17 %=========================================================================
18 %
19 % TODO: Make implementation nicer by better utilizing the redundancy
20 %
21 %=========================================================================
22
23
24
25 load('kernel.mat')
26
27 voxel_s_values = zeros(11,11,11);
28
29 origo = [ceil(11/2) ceil(11/2) ceil(11/2)];
30
31 for value_num = 1:length(vals)
32
33   I_c = (I(value_num));
34   J_c = (J(value_num));
35   K_c = (K(value_num));
36
```

```
  central = [I_c J_c K_c];

  % Now iterate over the eight possibilities, values that are
  % symmetrical are handled automatically

  c_1 = [I_c J_c K_c];
  c_2 = [I_c*-1 J_c*-1 K_c*-1];
  c_3 = [I_c*-1 J_c*+1 K_c*+1];
  c_4 = [I_c*+1 J_c*-1 K_c*+1];
  c_5 = [I_c*+1 J_c*+1 K_c*-1];
  c_6 = [I_c*-1 J_c*+1 K_c*-1];
  c_7 = [I_c*+1 J_c*-1 K_c*-1];
  c_8 = [I_c*-1 J_c*-1 K_c*+1];

  voxel_s_values(c_1(1)+origo(1),c_1(2)+origo(2),c_1(3)+origo(3)) = vals(value_num);
  voxel_s_values(c_2(1)+origo(1),c_2(2)+origo(2),c_2(3)+origo(3)) = vals(value_num);
  voxel_s_values(c_3(1)+origo(1),c_3(2)+origo(2),c_3(3)+origo(3)) = vals(value_num);
  voxel_s_values(c_4(1)+origo(1),c_4(2)+origo(2),c_4(3)+origo(3)) = vals(value_num);
  voxel_s_values(c_5(1)+origo(1),c_5(2)+origo(2),c_5(3)+origo(3)) = vals(value_num);
  voxel_s_values(c_6(1)+origo(1),c_6(2)+origo(2),c_6(3)+origo(3)) = vals(value_num);
  voxel_s_values(c_7(1)+origo(1),c_7(2)+origo(2),c_7(3)+origo(3)) = vals(value_num);
  voxel_s_values(c_8(1)+origo(1),c_8(2)+origo(2),c_8(3)+origo(3)) = vals(value_num);

end
```

```

% Small auxiliary function to find the factor lambda
% and I_0 on a mono exponential curve of the form
% I(t) = I_0 exp(lambda*t) given the value of the
% function on two point in time (time_0,act_0) and
% (time_1, act_1)

% Author Johan Blakkisrud blakkisr@stud.ntnu.no

% Param:
%   @time_0
%   @time_1
%   @act_0
%   @act_1

% Retval:

%   @I_0
%   @lambda_par


function [ I_0, lambda_par ] = get_exp_param( time_0, time_1, act_0, act_1 )

  lambda_par_phys = -0.0043;

  lambda_par = (log(act_1/act_0))/(time_1-time_0);

  if lambda_par > lambda_par_phys

    lambda_par = lambda_par_phys;

  end

```

```
  I_0 = act_1/exp(lambda_par*time_1);

  return

end
```

```
% Script to compare CT-defined VOI with PSF-corrected SPECT-defined VOI
%
% Name   : psf_corr_sphere
% Author : Johan Blakkisrud blakkisr@stud.ntnu.no
%
% Input is SPECT image files in DICOM-format, ending .IMA generate by the
% Siemens scanner and reconstruction software
%
% Voxel coordinates of the VOIs are given as an .XLS-file imported and
% formatted by the computer software PMOD(PMOD-industries)

close all
clear all % Ensure empty work space

%Input section

voxel_coord_file = 'data/pixel_data/pixel_coord.xlsx';
image_file_path = 'data/phantom/phantom_week1.IMA';

number_of_spheres_to_run = 5;
number_of_psfs_to_run = 10;

deconv_diff_table = zeros(number_of_spheres_to_run, number_of_psfs_to_run);
init_diff_table = zeros(number_of_spheres_to_run, number_of_psfs_to_run);

fwhm_list = [5.5 6.5 7.5 7.52 8.5 9.5 10.5 11.5 12.5 13.5];

sheat_names_spect = [...
  's1A' ; ...
  's2A' ; ...
  's3A' ; ...
  's4A' ; ...
  's5A'];

sheat_names_ct = [ ...
  's1M' ; ...
  's2M' ; ...
  's3M' ; ...
  's4M' ; ...
  's5M' ];

% Load image files

[image_matrix map] = dicomread(image_file_path);

image_raw_stack_pre = squeeze(image_matrix(:,:,1,:));

[x_size, y_size, num_of_slices] = size(image_raw_stack_pre(:,:,:));

image_raw_stack = zeros(x_size, y_size, num_of_slices);
image_raw_stack(:,:,:) = image_raw_stack_pre;

```

```
for sphere_num = 1:number_of_spheres_to_run

  sheat_pair = [sheat_names_spect(sphere_num,:) ; sheat_names_ct(sphere_num,:)];

  % Make PSF-function

  for fwhm_num = 1:number_of_psfs_to_run

    fwhm = fwhm_list(fwhm_num);
    voxel_size = 4.79;

    fwhm_voxel = fwhm/voxel_size;

    sigma = fwhm_voxel/2.35;
    si = 4*sqrt(2*log(2))*sigma;

    h = fspecial3('gaussian',[si si si]);

    disp('PSF-function made')
    disp('FWHM')
    disp(fwhm_num)

    disp('Now doing sphere')
    disp(sphere_num)

    for j = 1:2

    num_data = xlsread(voxel_coord_file,sheat_pair(j,:));

    X_index = num_data(:,2);
    Y_index = num_data(:,1);
    Z_index = num_data(:,3);
    vox_vals = num_data(:,4);

    for p_num = 1:length(X_index)

    point = [X_index(p_num) Y_index(p_num) Z_index(p_num)];
    point_val = vox_vals(p_num);
    stack_val = image_raw_stack(point(1), point(2), point(3));

    if stack_val ~= point_val

        disp('Error, non matching voxel-values')
        disp('Breaking loop')
        %break

    end

    end

    end

    disp('Data checked, SPECT and CT mathcing ok...')

    spect_mask = zeros(size(image_raw_stack));
    ct_mask = zeros(size(image_raw_stack));

    % Do masking of SPECT
```

```
111     num_data = xlsread(voxel_coord_file,sheat_pair(1,:));
112
113     X_index = num_data(:,2);
114     Y_index = num_data(:,1);
115     Z_index = num_data(:,3);
116     vox_vals = num_data(:,4);
117
118     for p = 1:length(X_index)
119
120         spect_mask(X_index(p), Y_index(p), Z_index(p)) = 1;
121
122     end
123
124     % Do masking of CT, not elegant
125     num_data = xlsread(voxel_coord_file,sheat_pair(2,:));
126
127     X_index = num_data(:,2);
128     Y_index = num_data(:,1);
129     Z_index = num_data(:,3);
130     vox_vals = num_data(:,4);
131
132     for p = 1:length(X_index)
133
134         ct_mask(X_index(p), Y_index(p), Z_index(p)) = 1;
135
136     end
137
138     disp('Masks made')
139
140     % Retreive linear indexes
141
142     I_ct = find(ct_mask);
143     I_spect = find(spect_mask);
144
145     sum_ct = sum(image_raw_stack(I_ct));
146     sum_spect = sum(image_raw_stack(I_spect));
147
148     disp('Initial difference')
149     disp(((sum_ct-sum_spect)/sum_spect)*100)
150     init_diff = ((sum_ct-sum_spect)/sum_spect)*100;
151
152     % Mask and sparse matrix stack
153
154     CT_masked_stack = image_raw_stack.*ct_mask;
155     SPECT_masked_stack = image_raw_stack.*spect_mask;
156
157     disp('Starting deconvolution');
158
159     spect_masked_deconvoluted = deconvlucy(SPECT_masked_stack,h,10);
160
161     disp('Deconvolution finished');
162
163     disp('New difference')
164
165     sum_deconv_ct = sum(spect_masked_deconvoluted(I_ct));
166
167     disp(((sum_deconv_ct-sum_spect)/sum_spect)*100)
168
```

```
169     new_diff = ((sum_deconv_ct-sum_spect)/sum_spect)*100
170
171     deconv_diff_table(sphere_num,fwhm_num) = new_diff;
172     init_diff_table(sphere_num, fwhm_num) = init_diff;
173
174
175   end
176
177 end
```

D.0.1 Voxel s-values from (Lanconnelli et al., 2012)

Lu177 – 4.8mm – Soft tissue
(i,j,k,S) [mGy/(MBqs)]

(0,0,0,1.78E−01) (1,5,0,2.61E−06) (3,0,5,2.02E−06) (4,2,4,1.90E−06)
(0,0,1,2.46E−03) (1,5,1,2.51E−06) (3,1,0,6.49E−06) (4,2,5,1.54E−06)
(0,0,2,1.61E−05) (1,5,2,2.27E−06) (3,1,1,5.93E−06) (4,3,0,2.70E−06)
(0,0,3,7.21E−06) (1,5,3,1.96E−06) (3,1,2,4.70E−06) (4,3,1,2.60E−06)
(0,0,4,4.12E−06) (1,5,4,1.65E−06) (3,1,3,3.51E−06) (4,3,2,2.34E−06)
(0,0,5,2.68E−06) (1,5,5,1.37E−06) (3,1,4,2.60E−06) (4,3,3,2.01E−06)
(0,1,0,2.46E−03) (2,0,0,1.61E−05) (3,1,5,1.96E−06) (4,3,4,1.70E−06)
(0,1,1,8.65E−05) (2,0,1,1.29E−05) (3,2,0,5.05E−06) (4,3,5,1.40E−06)
(0,1,2,1.29E−05) (2,0,2,8.08E−06) (3,2,1,4.70E−06) (4,4,0,2.13E−06)
(0,1,3,6.49E−06) (2,0,3,5.05E−06) (3,2,2,3.90E−06) (4,4,1,2.07E−06)
(0,1,4,3.89E−06) (2,0,4,3.34E−06) (3,2,3,3.04E−06) (4,4,2,1.90E−06)
(0,1,5,2.61E−06) (2,0,5,2.35E−06) (3,2,4,2.34E−06) (4,4,3,1.70E−06)
(0,2,0,1.61E−05) (2,1,0,1.29E−05) (3,2,5,1.81E−06) (4,4,4,1.46E−06)
(0,2,1,1.29E−05) (2,1,1,1.07E−05) (3,3,0,3.69E−06) (4,4,5,1.24E−06)
(0,2,2,8.08E−06) (2,1,2,7.21E−06) (3,3,1,3.51E−06) (4,5,0,1.69E−06)
(0,2,3,5.05E−06) (2,1,3,4.70E−06) (3,3,2,3.04E−06) (4,5,1,1.65E−06)
(0,2,4,3.34E−06) (2,1,4,3.18E−06) (3,3,3,2.51E−06) (4,5,2,1.54E−06)
(0,2,5,2.35E−06) (2,1,5,2.27E−06) (3,3,4,2.01E−06) (4,5,3,1.40E−06)
(0,3,0,7.21E−06) (2,2,0,8.08E−06) (3,3,5,1.61E−06) (4,5,4,1.24E−06)
(0,3,1,6.49E−06) (2,2,1,7.21E−06) (3,4,0,2.70E−06) (4,5,5,1.08E−06)
(0,3,2,5.05E−06) (2,2,2,5.44E−06) (3,4,1,2.60E−06) (5,0,0,2.68E−06)
(0,3,3,3.69E−06) (2,2,3,3.90E−06) (3,4,2,2.34E−06) (5,0,1,2.61E−06)
(0,3,4,2.70E−06) (2,2,4,2.81E−06) (3,4,3,2.01E−06) (5,0,2,2.35E−06)
(0,3,5,2.02E−06) (2,2,5,2.08E−06) (3,4,4,1.70E−06) (5,0,3,2.02E−06)
(0,4,0,4.12E−06) (2,3,0,5.05E−06) (3,4,5,1.40E−06) (5,0,4,1.69E−06)
(0,4,1,3.89E−06) (2,3,1,4.70E−06) (3,5,0,2.02E−06) (5,0,5,1.39E−06)
(0,4,2,3.34E−06) (2,3,2,3.90E−06) (3,5,1,1.96E−06) (5,1,0,2.61E−06)
(0,4,3,2.70E−06) (2,3,3,3.04E−06) (3,5,2,1.81E−06) (5,1,1,2.51E−06)
(0,4,4,2.13E−06) (2,3,4,2.34E−06) (3,5,3,1.61E−06) (5,1,2,2.27E−06)
(0,4,5,1.69E−06) (2,3,5,1.81E−06) (3,5,4,1.40E−06) (5,1,3,1.96E−06)
(0,5,0,2.68E−06) (2,4,0,3.34E−06) (3,5,5,1.19E−06) (5,1,4,1.65E−06)
(0,5,1,2.61E−06) (2,4,1,3.18E−06) (4,0,0,4.12E−06) (5,1,5,1.37E−06)

(0,5,2,2.35E−06) (2,4,2,2.81E−06) (4,0,1,3.89E−06) (5,2,0,2.35E−06)
(0,5,3,2.02E−06) (2,4,3,2.34E−06) (4,0,2,3.34E−06) (5,2,1,2.27E−06)
(0,5,4,1.69E−06) (2,4,4,1.90E−06) (4,0,3,2.70E−06) (5,2,2,2.08E−06)
(0,5,5,1.39E−06) (2,4,5,1.54E−06) (4,0,4,2.13E−06) (5,2,3,1.81E−06)
(1,0,0,2.46E−03) (2,5,0,2.35E−06) (4,0,5,1.69E−06) (5,2,4,1.54E−06)
(1,0,1,8.65E−05) (2,5,1,2.27E−06) (4,1,0,3.89E−06) (5,2,5,1.30E−06)
(1,0,2,1.29E−05) (2,5,2,2.08E−06) (4,1,1,3.69E−06) (5,3,0,2.02E−06)
(1,0,3,6.49E−06) (2,5,3,1.81E−06) (4,1,2,3.18E−06) (5,3,1,1.96E−06)
(1,0,4,3.89E−06) (2,5,4,1.54E−06) (4,1,3,2.60E−06) (5,3,2,1.81E−06)
(1,0,5,2.61E−06) (2,5,5,1.30E−06) (4,1,4,2.07E−06) (5,3,3,1.61E−06)
(1,1,0,8.65E−05) (3,0,0,7.21E−06) (4,1,5,1.65E−06) (5,3,4,1.40E−06)
(1,1,1,2.35E−05) (3,0,1,6.49E−06) (4,2,0,3.34E−06) (5,3,5,1.19E−06)
(1,1,2,1.07E−05) (3,0,2,5.05E−06) (4,2,1,3.18E−06) (5,4,0,1.69E−06)
(1,1,3,5.93E−06) (3,0,3,3.69E−06) (4,2,2,2.81E−06) (5,4,1,1.65E−06)
(1,1,4,3.69E−06) (3,0,4,2.70E−06) (4,2,3,2.34E−06) (5,4,2,1.54E−06)
(1,1,5,2.51E−06) (1,3,1,5.93E−06) (1,4,3,2.60E−06) (5,4,3,1.40E−06)
(1,2,0,1.29E−05) (1,3,2,4.70E−06) (1,4,4,2.07E−06) (5,4,4,1.24E−06)
(1,2,1,1.07E−05) (1,3,3,3.51E−06) (1,4,5,1.65E−06) (5,4,5,1.08E−06)
(1,2,2,7.21E−06) (1,3,4,2.60E−06) (5,5,0,1.39E−06) (5,5,3,1.19E−06)
(1,2,3,4.70E−06) (1,3,5,1.96E−06) (1,2,5,2.27E−06) (1,4,1,3.69E−06)
(1,2,4,3.18E−06) (1,4,0,3.89E−06) (1,3,0,6.49E−06) (1,4,2,3.18E−06)
(5,5,1,1.37E−06) (5,5,4,1.08E−06)
(5,5,2,1.30E−06) (5,5,5,9.50E−07)